12-17-2018

# Electrical Characterization of Crystalline $UO_2$, $ThO_2$ AND $U_{0.71}Th_{0.29}O_2$

Christina L. Dugan


# ELECTRICAL CHARACTERIZATION OF CRYSTALLINE $UO_2$, $THO_2$ AND $U_{0.71}TH_{0.29}O_2$

DISSERTATION

Christina L. Dugan, Lieutenant Colonel, USA

AFIT-ENP-DS-18-D-007

**DEPARTMENT OF THE AIR FORCE**
**AIR UNIVERSITY**

***AIR FORCE INSTITUTE OF TECHNOLOGY***

**Wright-Patterson Air Force Base, Ohio**

The views expressed in this thesis are those of the author and do not reflect the official policy or position of the United States Air Force, the Department of Defense, or the United States Government.

AFIT-ENP-DS-18-D-007

# ELECTRICAL CHARACTERIZATION OF CRYSTALLINE $UO_2$, $THO_2$ AND $U_{0.71}TH_{0.29}O_2$

DISSERTATION

Presented to the Faculty

Department of Engineering Physics

Graduate School of Engineering and Management

Air Force Institute of Technology

Air University

Air Education and Training Command

In Partial Fulfillment of the Requirements for the

Degree of Doctor of Philosophy

Christina L. Dugan, BS, MS

Lieutenant Colonel, USA

October 2018

**DISTRIBUTION STATEMENT A**
Approved For Public Release; Distribution Unlimited

.

AFIT-ENP-DS-18-D-007

# ELECTRICAL CHARACTERIZATION OF CRYSTALLINE $UO_2$, $THO_2$ AND $U_{0.71}TH_{0.29}O_2$

Christina L. Dugan, BS, MS
Lieutenant Colonel, USA

Committee Membership:

James C. Petrosky, PhD
Chair

John W. McClory, PhD
Member

Sheena L. Winder, Lt Col
Member

ADEDJI B. BADIRU, PhD
Dean, Graduate School of Engineering and Management

## Abstract

Hydrothermally grown structures of uranium dioxide ($UO_2$), thorium dioxide ($ThO_2$), and $U_xTh_{1-x}O_2$ alloys were characterized for suitability in uranium-based neutron detectors and nuclear reactor fuels. $ThO_2$ was studied for its potential in an envisioned $UO_2/ThO_2$ heterojunction. A $U_{0.71}Th_{0.29}O_2$ alloy was studied because of its resistance to oxidation, and potential to stabilize the surface of $UO_2$.

The majority carrier mobility of the $UO_2$ samples, as measured by Hall effect, was consistent with established literature values on samples requiring substantial surface preparation. Direct current I(V) measurements provided evidence that the Hall currents may penetrate below any surface oxidized region caused by ambient air exposure. The depth of this surface structure was further investigated using angular resolved x-ray photoemission spectroscopy (ARPES).

The $U_{0.71}Th_{0.29}O_2$ effective Debye temperature of 217± 24 K was measured using temperature-dependent x-ray photoemission spectroscopy (XPS). The specific heat capacity for the $U_{0.71}Th_{0.29}O_2$ alloy was calculated from the Debye temperature in order to compare to the heat capacity obtained from the more traditional modulated-temperature differential scanning calorimetry (MDSC). The XPS derived Debye temperature specific heat capacity was lower than with MDSC, showing how surface oxidation and hydrolysis effect surface stability.

The U $4f_{7/2}$ peak energy was observed using ARPES, providing evidence of $U^{4+}$ and $U^{6+}$ oxidation states at the surface with an increased concentration of the $U^{4+}$ oxidation states further from the surface. The U 5*f* peaks observed in ARPES provided

evidence of $U^{4+}$ at the surface but does not preclude the presence of $U^{6+}$. Throughout the surface measurement, the electronic band-gap energy remained at 2.2 eV, confirming the dominance of $UO_2$ in establishing the electronic structure. These surface characteristics also revealed a vacuum reduced $UO_2$ surface and excess oxygen incorporated into the lattice to form a $UO_{2+x}$ selvedge region.

**Acknowledgments**

First and foremost I would like to thank God, for with God nothing shall be impossible. God truly blessed me with a great advisor and dissertation committee, wonderful lab technicians, and loving parents. Without the assistance of the following personnel, none of this would have been possible. I would like to show my sincere gratitude to my faculty advisor, Dr. James Petrosky, for his guidance and support throughout the course of this dissertation effort. I would like to thank the other two members of my committee, Dr. John McClory and Lt Col Sheena Winder for their time, advisement, and knowledge of nuclear physics and material science. Their insight and experience was certainly appreciated. I want to acknowledge Air Force Research Laboratory for providing hydrothermally-grown, single-crystal actinide samples and assistance with modulated-temperature differential scanning calorimetry. I would like to thank the lab technician, Greg Smith for his constant support, patience, and time. The numerous hours he dedicated to repairing equipment, building new chambers, and troubleshooting are much appreciated. Last but not least, I would like to thank my parents, who support me throughout my life in all my endeavors.

Christina L. Dugan

## Table of Contents

Page

Abstract ..... iv

Table of Contents ..... vii

List of Figures ..... x

List of Tables ..... xv

I. Introduction ..... 1

1.1 Motivation ..... 1
1.2. Uranium Dioxide Atomic Structure ..... 4
1.2.1 Uranium Dioxide Detector Concepts ..... 5
1.2.2 Uranium Dioxide As An Electronic Medium ..... 5
1.3 Crystal Quality and Electronic Performance ..... 7
1.4 $UO_2$ Surface Morphology ..... 8
1.5. Thorium Dioxide and $U_{0.71}Th_{0.29}O_2$ Characteristics ..... 9
1.6 Research Measurements and Methods ..... 11

II. Theoretical Basis For Experimental Techniques ..... 19

2.1 Primary Experimental Techniques ..... 20
2.1.1 X-ray Photoemission Spectroscopy ..... 20
2.1.2 Cathodoluminescence Spectroscopy ..... 22
2.2 Supplementary Experimental Techniques ..... 27
2.2.1 Hall Effect, I(V), and C(V) Characteristic Curves ..... 27
2.2.2 Ellipsometry Technique ..... 31
2.2.3 Differential Scanning Calorimetry ..... 37
2.3 Reference ..... 40

III. Electrical Characterization of $UO_2$ – Improved Mobility in Single Crystal $UO_2$ Based Electronics ..... 42

Abstract ..... 42
3.1 Research Innovation and Objective ..... 43
3.2 Impacts on Warfighter Mission ..... 43
3.3 Introduction ..... 43
3.4 Method ..... 45
3.4.1 Hydrothermal Growth ..... 45
3.4.2 Hall Measurements ..... 45
3.4.3 Current-Voltage, I(V), Measurements ..... 46
3.5 Results ..... 47
3.5.1 Hall Measurement Results ..... 47

3.5.2 Direct Current, Current Voltage Measurement Results ..... 47
3.6 Discussion ..... 48
3.7 Conclusion ..... 50
3.8 References ..... 50

IV. Electrical and Material Properties of Hydrothermally Grown Single Crystal (111) $UO_2$ 52

Abstract ..... 52
4.1 Introduction ..... 53
4.2 Experimental ..... 54
4.3 Theory ..... 56
4.4 Results & Discussion ..... 58
4.5 Conclusion ..... 68
4.6 References ..... 69

V. The Debye Temperature of a Single Crystal Thorium Uranium Dioxide Alloy ..... 74

Abstract ..... 74
5.1 Introduction ..... 75
5.2 Experiment ..... 77
5.3 Results ..... 78
5.4 Conclusions ..... 83
5.5 References ..... 84

VI. A Comparison of Modulated Differential Scanning Calorimetry and Debye Temperature Determined Specific Heat Capacities of $UO_2$, $ThO_2$, and $U_{0.71}Th_{0.29}O_2$ ..... 86

Abstract ..... 86
6.1 Introduction ..... 86
6.2. Experiment ..... 88
6.3 Theory ..... 89
6.4 Results ..... 91
6.5 Conclusion ..... 93
6.6 References ..... 94

VII. Surface-Depth Profiling of an Oxidized Single-Crystal $UO_2$ Surface by Angle-Resolved X-ray Photoemission Spectroscopy ..... 96

Abstract ..... 96
7.1 Introduction ..... 97
7.2 Experiment ..... 98
7.3 Results ..... 99
7.3.1 Binding Energies of U 4f Core Level Peaks ..... 99
7.3.2 Binding Energy of O1s. ..... 102
7.3.3 Binding Energies of O 2p - Valence-Band Region Transitions ..... 104

7.4 Discussion.....106
7.4.1 U 4f Binding Energies and Oxidation States..... 106
7.4.2 Binding Energy of O 1s. ..... 109
7.4.3 Valence Band Region ..... 110
7.5 Conclusion.....111
7.6 References .....112

VIII. Near-Infrared to Vacuum Ultraviolet Dielectric Functions and Critical Points of Single Crystal Thoria Compared to Urania .....114

8.1 Introduction .....114
8.2 Experiment .....115
8.3 Theory.....117
8.4 Results .....118
8.4.1 The complex dielectric function of $ThO_2$ and $UO_2$: ..... 118
8.4.2 Interband transitions of $ThO_2$ and $UO_2$..... 123
8.5 Conclusions .....129
8.6 References .....129

IX. Conclusions.....134

9.1 Summary of Findings .....134
9.2. Future Work.....137
9.2.1 Materials Characterization..... 137
9.2.2 Electrical Characterization..... 138

## List of Figures

Page

Figure 1. The microscopic fission cross sections for $^{235}U$ and $^{238}U$ as a function of neutron energy [7]. ..... 3

Figure 2. Unit cell of the face-centered cubic crystal of $UO_2$. The tetrahedral-coordinated anion sites (oxygen sub-lattice) are represented in black. The cubic coordinated cations (uranium sub-lattice) are represented in white. The normal interstitial sites are found in the cell edge centers (0, 0, ½), (0, ½, 0), (½, 0, 0) and the cell center (½, ½, ½) [9]. ..... 4

Figure 3. SEM images of surfaces and edges of s.c. $UO_2$. ..... 10

Figure 4. Generalized energy diagram for photoelectron emission in an XPS measurement. Derived from [1]. ..... 21

Figure 5. Schematic diagram of radiative transitions between the conduction band ($E_c$), the valence band ($E_v$) and the exciton ($E_E$), donor ($E_D$) and acceptor levels ($E_A$) in a semiconductor [4]..... 23

Figure 6. Schematic of a van der Pauw configuration used in the determination of the two characteristic resistances. A component of $R_A$ and $R_B$ is presented [9]..... 28

Figure 7. Two electromagnetic waves traveling orthogonal to the direction of propagation with arbitrary amplitude and phase [13]. ..... 32

Figure 8. Geometry of an ellipsometric experiment displaying the s- and p- directions [13]. ..... 35

Figure 9. Electric field and magnetic field for p- polarization. The magnetic field, *B*, is perpendicular to the plane of the page and is pointing toward the reader [13]. ..... 36

Figure 10. Heat flux DSC with disk-type measuring system with 1) disk, 2) furnace, 3) lid, 4) differential thermocouples, 5) programmer and controller, S) sample crucible, and $R_{ef}$) reference crucible. The arrows at $\phi_{FS}$ and $\phi_{FR}$ indicate the locations where the heat flow rate from furnace to reference sample crucible and heat flow rate from the furnace to the reference sample are measured respectively. The recorder combines the $\phi_m$, measured heat flow rate and *k* calibration factor [17]..... 38

Figure 11. Current vs. voltage measurements from d.c. I(V) compared to the van der Pauw Hall measurements. Inset shows the ohmic nature (linearity) of the contacts for both measurements. ..... 48

Figure 12. Schematic of van der Pauw Hall configuration and that of the d.c. I(V) measurement (dashed lines). Both show current must pass through the unknown surface layer twice. ..... 49

Figure 13. $UO_2$ with $CaF_2$ seed crystal. Figure 13(a) is a side-view of the $UO_2$ on the crystalline $CaF_2$ seed. Figure 13(b) provides a top view with a 4.5 mm diameter E-GaIn contact. In Figure 13(c) a diagram of the crude Ag/$UO_2$/$CaF_2$/$UO_2$/E-GaIn device. ..... 56

Figure 14. The band structure of bulk $UO_2$ (schematically shown with O: red; U: blue) using Heyd-Scuseria-Ernzerhof (HSE) hybrid functional. The band gap is 2.19 eV and the ground state is anti-ferromagnetic. ..... 58

Figure 15. The current versus voltage measurements of Ag/$UO_2$/E-GaIn metal-semiconductor Schottky device. The nearly linear data indicates a minimal barrier to charge carriers but is inconclusive as to the semiconductor majority carrier. ..... 60

Figure 16. The capacitance versus frequency and conductance versus frequency (semi-Log scale) measurements of Ag/$UO_2$/E-GaIn MS Schottky device. The frequency dependence of the data beginning at 10 kHz shows the presence of defects within the device. ..... 61

Figure 17. The capacitance versus voltage measurement for the perturbation frequencies 100 kHz, 1 MHz, and 10 MHz. The inset is a $1/C^2$ extrapolation for the determination of the effective barrier height $\varphi_B$=1.28eV. ..... 62

Figure 18. Modeled diffusion capacitance $C_D$ (·) overlaid on C(V) data measured (solid lines) at 100 kHz and 1 MHz for the Ag/$UO_2$Schottky diode. The calculated diffusion capacitance, $C_D$, indicates a drift carrier lifetime in (a) of approximately 50 $\mu$s and in (b) of approximately 250 $\mu$s. ..... 63

Figure 19. The depth resolved XPS on the $UO_2$ (111). Both U 4*f* peaks shift to higher binding energies at the surface of the crystal, with increasing take off angle, indicating a chemical shift of the U to an oxidation state greater than $U^{4+}$. ..... 64

Figure 20. Dielectric function of single-crystal $UO_2$ obtained in this analysis (red and green solid lines, respectively) compared to those by Siekhaus et al. [36](black dash and dot, respectively). Both the results of Siekhaus et al. [38] and this work come from ellipsometric techniques (see text). Arrows indicating the critical points identified by our work are labeled and correspond to Gaussian oscillator parameters. ..... 66

Figure 21. (a) XPS core level spectra for 301, 423, and 623 K in the region of the Th 4*f* shells. As the temperature is elevated the core level photoemission intensity declines sharply. (b) The thorium binding energy fits for 301 K reveal the 334.4 and 343.6 eV peaks for Th $4f_{7/2}$ and Th $4f_{5/2}$ respectively and the associated satellite peak. The fit

also reveals an unknown peak at 341.5 eV. Data are shown plotting every 8th data point for clarity. ..... 80

Figure 22. (a) XPS core level spectra for 301, 423, and 623 K in the region of the U 4*f* shells. As the temperature is elevated the core level photoemission intensity declines sharply. (b) The uranium binding energy fits for 380.3 K reveal the 391.3 eV peaks for U $4f_{7/2}$ and U $4f_{5/2}$ respectively and the associated satellite peak fits are shown at 301 K. Data are shown plotting every 8th data point for clarity. ..... 80

Figure 23. The natural logarithmic ratio of intensities as a function of temperature ranging from 301 to 623 K. The reference intensity, $I_o$, is the intensity for the room temperature measurement at 301 K. (a) The natural logarithmic slope for the Th $4f_{5/2}$ and Th $4f_{7/2}$ photoelectron is plotted along with the corresponding temperature measurements. (b) The natural logarithmic slope for the U $4f_{5/2}$ and U $4f_{7/2}$ photoelectron is plotted along with the corresponding temperature measurements. . 82

Figure 24. Specific heat capacities for $ThO_2$, $UO_2$, and $U_{0.71}Th_{0.29}O_2$ for temperatures ranging from 300 to 673 K. As observed in the left figure, the dashed lines represent specific heat calculated utilizing XPS determined Debye temperatures. The shaded regions represent experimental uncertainties with previously calculated Debye temperatures. The solid lines reference previously published Debye temperatures. As shown in the right figure, the MDSC calculated heat capacity of an amorphous fuel pellet is compared to the specific heat capacity s.c. $UO_2$ and $ThO_2$. Note a later hydrothermal growth, solid line, increases the heat capacity of the s.c. $UO_2$. The solid lines are the first MDSC measurement results. Dashed lines represent measurements 2 and 3 for each sample. The star denotes calculated specific heat capacity values at 300 K derived the from $UO_2$ temperature dependent heat content equation at 63.6 [J/K mol] utilizing a drop calorimetry measurements [18]. ..... 92

Figure 25. AR-XPS spectra of the U 4*f* shell spectra collected from angles of 34, 44, 49, 54, and 64° between the surface and the x-ray source with 34° representing the most-surface sensitive measurement. ..... 99

Figure 26. The U 4*f* shell binding energies are peak deconvolved for 34 and 49° respectively. The dotted red lines represent the individual deconvoluted peaks, while the red dashed line is the summation of the peak deconvolution. Also provided are the various shakeup satellite peaks and their energy representation. ..... 100

Figure 27. Angle-resolved XPS core level spectra in the regions of the O 1*s* shell. The angle dependent spectra collected from angles of 34, 44, 49, 54, and 64°between the surface and the x-ray source with 34° representing the most-surface sensitive measurement. ..... 102

Figure 28. The O 1*s* binding energies are peak deconvolved for 34 and 49° respectively. The dotted red lines represent the individual deconvoluted peaks, while the red dashed line is the summation of the peak deconvolution. The three O 1*s* peaks are

observed at 531.0, 531.9, and 533.5 eV for the 34° spectrum and are observed at 531.0, 533.5, and 534.0 eV for the 49° spectrum..... 103

Figure 29. The AR-XPS spectra for the $UO_2$ valence band edge collected for angles of 34, 44, 49, 54, and 64° between the surface and the x-ray source. An electronic band gap of ~2.2 eV is denoted by red lines..... 104

Figure 30. The O 2*p* and U 5*f* binding energies are peak deconvolved for 34 and 49° respectively. The dotted red lines represent the individual deconvoluted peaks, while the red dashed line is the summation of the peak deconvolution. The 34° spectrum provides evidence of the spin orbit coupled U $5f_{7/2}$ and U $5f_{5/2}$ orbitals while in the 49° spectrum the U *5f* orbitals are indistinguishable. ..... 105

Figure 31. The real and imaginary parts of the $ThO_2$ dielectric function, extracted from the variable angle spectroscopic ellipsometry by wavelength-by-wavelength analysis (green and blue circles, respectively), shown in comparison with the critical point model dielectric function (red solid). Individual contributions to the imaginary part of the dielectric function obtained with Gaussian oscillators are shown with vertical lines corresponding to their center energies ($CP_1$-magenta, $CP_2$-dark cyan, $CP_3$-violet, $CP_4$-dark yellow, $CP_5$-orange, as well as another contribution outside the investigated spectral range to account for higher energy transitions shown as navy). ..... 119

Figure 32. The real and imaginary parts of the $UO_2$ dielectric function extracted from the variable angle spectroscopic ellipsometry by wavelength-by-wavelength analysis (green and blue circles, respectively) shown in comparison with the critical point model dielectric function (red solid). Individual contributions to the imaginary part of the dielectric function obtained with Gaussian oscillators are shown with vertical lines corresponding to their center energies ($CP_1$-magenta, $CP_2$-dark cyan, $CP_3$-violet, $CP_4$-dark yellow, $CP_5$-orange, as well as another contribution outside the investigated spectral range to account for higher energy transitions shown as navy). ..... 121

Figure 33. The optical transitions for single crystal $UO_2$, measured from CL. The incident electron energy is 10 keV to avoid surface effects. The weaker transitions are indicated by arrows, and the transition corresponding the lowest unoccupied state to highest occupied state transition is shown in the inset..... 122

Figure 34. The band structure of bulk $ThO_2$ using Heyd-Scuseria-Ernzerhof (HSE) hybrid functional. The band gap is 6.12 eV and the ground state is anti-ferromagnetic.... 124

Figure 35. Band structure and density of states of $ThO_2$ by the (a) PBE+U functional in the density mixing scheme and by (b) PBE+U function in the EDFT scheme..... 126

Figure 36. The calculated real (blue) and imaginary (red) parts of the $ThO_2$ dielectric function. ..... 127

Figure 37. The calculated real (blue) and imaginary (red) parts of the $UO_2$ dielectric function. ..... 127

## List of Tables

Page

Table 1. Summary of actinide oxides measured, experimental methods employed, and desired experimental outcomes. ..... 12

Table 2. Hall Effect data from literature values compared. ..... 47

Table 3. Critical point transition parameters of single-crystal $UO_2$, obtained from spectroscopic ellipsometry data analysis of single-crystal $UO_2$. Parentheses denote 90% confidence of the last digit. ..... 67

Table 4. The angle-dependent U $4f_{7/2}$ and U $4f_{5/2}$ peak deconvoluted binding energies (eV) for the U $4f_{7/2}$ and U $4f_{5/2}$ sum of hydrothermally-grown s.c. $UO_2$. ..... 101

Table 5. The valence band region angle-dependent O $2p$ and U $5f$ peak deconvoluted binding energies [eV] for hydrothermally-grown s.c. $UO_2$ ..... 106

Table 6. Theoretically computed atomic percent ratios for the surface depth profiling of hydrothermally-grown s.c. $UO_2$ by a comparison of the U $4f_{7/2}$ and U $4f_{5/2}$ binding energies. ..... 107

Table 7. Critical point parameters determined from the VASE model dielectric function analysis, amplitude (A), energy (E) and broadening (Br) for $ThO_2$ in comparison with band-to-band transition energies determined from DFT calculation. Digits in parenthesis indicate 90% confidence from model analysis. A higher energy transition outside the investigated range is also used to account for higher energy transitions. ..... 120

Table 8. Critical point analysis parameters of amplitude (A), energy (E) and broadening (Br) for $UO_2$, obtained from VASE. Digits in parenthesis indicate 90% confidence from model analysis. A higher energy transition outside the investigated range is also used to account for higher energy transitions. ..... 123

ELECTRICAL CHARACTERIZATION OF CRYSTALLINE $UO_2$, $THO_2$ AND $U_{0.71}TH_{0.29}O_2$

# I. Introduction

## 1.1 Motivation

Tracking and identifying radiation sources in the age of nuclear proliferation and well-resourced non-state actors is a national priority. Current neutron detection methods favor large detector volumes and long data collection times. Additionally, portable neutron detection methods have persistent problems with low signal-to-noise (small pulse height) and require large applied voltages.

Conventional neutron detection usually employs scintillators, gas proportional tubes, or semiconductors with separate conversion layers that convert neutrons to charged reaction products. The challenge in conversion-layer devices is to construct a layer of adequate thickness for neutron capture that is also thin enough to allow the resulting reaction products to interact with the charge-sensitive areas. Standard conversion-layer devices typically employ 30 to 40 μm of enriched $^{10}B$ due to the high thermal capture cross section of the isotope $^{10}B$ and the ability for the energetic Li (0.84 MeV) and α (1.47 MeV) daughter particles to escape. The conversion layer thickness is thus a compromise between the neutron interaction rate and the ability to capture the charge in an electrically active medium. Some novel solid-state technologies provide a thin-film neutron detector consisting of a (or a stack of) semiconductor diode(s), each surrounded by a thin neutron-absorbing material.

As an alternative to a conversion layer, the conversion atoms can also be incorporated into the detection medium (gas, scintillator, or semiconductor). This method has the advantage of

a more efficient structure to capture the reaction products, but often results in a reduced electronic signature (or in the case of scintillators, reduced light output). As an example, icosahedral semiconducting boron carbides [1] [2] [3] [4] [5] have recently garnered interest because a high quality electronic material can be made that incorporates $^{10}B$ as a component of the semiconductor material.

Another consideration in $^{10}B$ based neutron detectors is the energy dependence of the capture cross section. For thermal neutrons (≈0.025 eV), the capture cross section for $^{10}B$ is about 3840 barns. However, for neutrons of 1.6 MeV (the mean energy of prompt fission neutrons from $^{235}U$ [6]) the $^{10}B$ absorption cross section is 0.2 barns. Therefore, to achieve the highest detection efficiency for neutrons from fission, $^{10}B$ based neutron detectors require neutron moderation, resulting in a loss of efficiency either due to scattering out or capture outside of the detection medium. Similar arguments can be made for other conventional neutron conversion materials.

For $^{235}U$, the thermal fission cross section is 585 barns and the fast neutron (1.6 MeV) fission cross section is 2 barns as shown in Figure 1. Also from Figure 1, the $^{238}U$ thermal fission cross section is 16.8 microbarns and its fast neutron (1.6 MeV) fission cross section is 1.1 barns. Therefore, $^{235}U$ is approximately 2x more likely to fission with fast neutrons than $^{238}U$ in materials of the same density. In comparison, $^{10}B$ has a thermal neutron absorption cross section 6.5x's greater than the thermal fission cross section for $^{235}U$. However, for neutrons at 1.6 MeV, $^{235}U$ has a 4x larger fission cross section and $^{238}U$ has a 2x larger fission cross section than the $^{10}B$ neutron absorption cross section of approximately 0.5 barns. Therefore, for fast neutron detection, the uranium cross section is preferred.

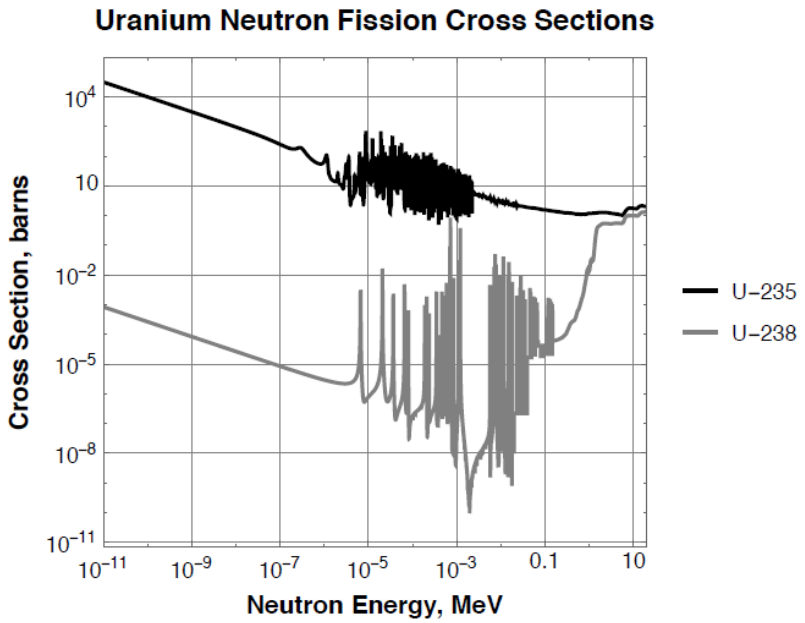


**Figure 1. The microscopic fission cross sections for $^{235}$U and$^{238}$U as a function of neutron energy [7].**

A uranium-based neutron detector has a substantial energy output advantage as compared to conventional neutron detection devices that incorporate non-fissile or fissionable neutron conversion materials, as shown in Equations (1.1) and (1.2). The fission of uranium results in two or more charged fission fragments with 168 MeV, having the potential of producing more than 25 million electronic transitions across the $UO_2$ 2.1 eV band gap. The resulting high-energy fission products may, however, degrade the electronic properties of the $UO_2$ either due to formation of point defects or because of subsequent decays and transmutations providing a larger internal background noise signal. A further consideration is that uranium requires special handling procedures, especially if enriched, to take advantage of the higher fission cross section of $^{235}$U, as opposed to the more naturally abundant $^{238}$U. Therefore, this study will help to understand the tradeoffs with uranium-based detectors made from $UO_2$, $UO_2/ThO_2$, and $U_{0.71}Th_{0.29}O_2$ using $^{238}$U, before the complications of using and managing $^{235}$U are considered. As an additional advantage, if $UO_2$ solid-state detectors are placed in an array with a mixture of

detectors made predominantly from $^{235}$U or $^{238}$U, some neutron energy spectral information may be ascertained from the count rates due to the difference in fission cross sections [8].

$$^{10}_{5}B + ^{1}_{0}n \xrightarrow{3840\ b} ^{7}_{3}Li + ^{4}_{2}He + 0.48\ MeV\ \gamma + 2.31\ MeV\ (94\%)\ or\ 2.79\ MeV\ (6\%) \quad (1.1)$$

$$^{235}_{92}U + ^{1}_{0}n \xrightarrow{580\ b} 2\ fission\ fragments + (2\ or\ 3)^{1}_{0}n + \gamma + 180\ MeV \quad (1.2)$$

### 1.2. Uranium Dioxide Atomic Structure

Uranium dioxide has a fluorite structure consisting of simple cubic packing of oxygen ions with eight-fold coordination of large $U^{4+}$ cations in half of the interstitial sites as shown in Figure 2. The lattice parameter, $a$, of $UO_2$ at room temperature is 547.081 pm with an O/U ratio of 2.001 [9]. The large number of vacancies in this open structure creates a high ionic conductivity due to vacancy diffusion. Hence, stoichiometric $UO_2$ is a stable but very active substance [10]. Fission products and substitutional impurities are readily accommodated in the vacant lattice positions. Impurities in the lattice produced by fission or neutron absorption may influence the crystal's electronic properties, specifically mobility and carrier lifetime.

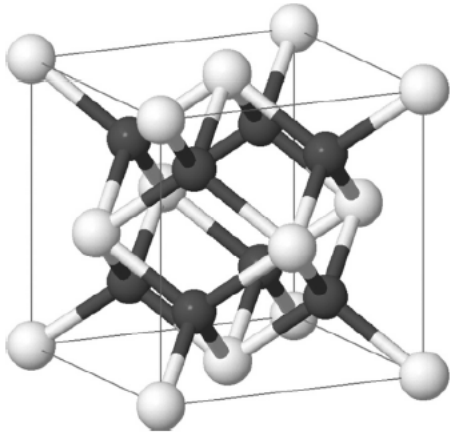

**Figure 2. Unit cell of the face-centered cubic crystal of $UO_2$. The tetrahedral-coordinated anion sites (oxygen sub-lattice) are represented in black. The cubic coordinated cations (uranium sub-lattice) are represented in white. The normal interstitial sites are found in the cell edge centers (0, 0, ½), (0, ½, 0), (½, 0, 0) and the cell center (½, ½, ½) [9].**

### *1.2.1 Uranium Dioxide Detector Concepts*

Two potential neutron detector designs are under consideration that employ $UO_2$. One device concept is an all $UO_2$ p-n junction. This device offers the best potential for a high efficiency device structure, but the growth method and control of doping has not yet been realized. Another design would be a heterojunction diode with $ThO_2$ on one side. Such a design would consist of a p-type $UO_2$ and n-type $ThO_2$ layer. This structure has been realized and is under study.

### *1.2.2 Uranium Dioxide As An Electronic Medium*

Uranium has been studied as a neutron absorber since the 1930s [11]. In recent years, limited research has explored the geometric and electronic properties of $UO_2$ for the purpose of semiconductor device fabrication [12], [13], [14]. Primarily focused on the prospects of neutron detection and photovoltaics, $UO_2$ semiconductors have been largely undeveloped due to the difficulty of material growth [12], [14]. Single-crystal growth of actinides for application in electronics is complex due to the very large electron-phonon coupling, lattice deformations, and significant changes in Debye temperature mediated through Jahn-Teller distortions [15]. These latter effects are unusual, as $UO_2$ is neither a semiconductor nor a metal; it is a Mott insulator with a U 5*f* band 2.1 eV above the optical valence band [16]. Therefore, phonons cannot couple to the Fermi sea of electrons or holes. Given the orthorhombic allotrope of α-phase uranium metal, the fluorite structure of $UO_2$, and the rapid oxidation and large range of O/U ratios, it is difficult to control sample stoichiometry without strictly controlling the temperature and pressure of the growth environment [17].

A further complication exists. While defect creation is expected to occur at temperatures above 1000 K, the simplified phase diagram of the $UO_x$ system suggests a $UO_{2+x}$ to a combination of $UO_{2+x}$ and $U_4O_{9-y}$ with a transition between 473 and 670 K [18], [19]. Such a structural phase transition alters the density of lattice imperfections and changes in defect density enhance Jahn-Teller distortions significantly [15], [19].

The challenges of growing high-quality single-crystal (s.c.) $UO_2$ have been recently addressed with the fabrication of high-quality s.c. actinide oxide samples using a hydrothermal synthesis growth technique [20]. This growth process has produced bulk crystals of near-stoichiometric $UO_2$. This method opens the door to broader understanding and higher fidelity assessments of the optical and semiconductor properties than previously possible.

The hydrothermal growth technique stems from mineral formation in nature under elevated pressure and temperature conditions in the presence of water. In the supercritical regime of water, normally insoluble materials are dissolved. The supercritical regime is above the critical point of water (647 K and 218 atm.), where water exists in both liquid and gas phases.

A feedstock is placed in the bottom of an autoclave and heated at high temperatures and pressures. A temperature gradient is maintained across the growth chamber and a mineralizer is added to the working fluid to promote solubility. The temperature differential between the zones creates a convective flow raising the dissolved feedstock to the “cooler” growth zone. The dissolved minerals may deposit on the walls of the autoclave creating spontaneous nucleation or deposition onto the seed crystal. A seed crystal is hung from a wire to provide maximum surface area for exposure to the dissolved nutrients. Transient solubility conditions may occur during the initial heating stage or when the autoclave is cooled for sample extraction. The seed crystal or initial crystal growth may dissolve prior to the desired operating temperature and pressure being

reached. During cool-down, undesirable chemical species may be deposited [21]. The Air Force Research Laboratory has developed a method for hydrothermally growing s.c. $UO_2$ at the supercritical regime of water. Work function measurements, C(V), I(V), and ellipsometry measurements were made on these crystals in the present research.

### 1.3 Crystal Quality and Electronic Performance

Electronic performance can be degraded by crystal defects, either intrinsic displacement defects from growth, substitutional defects from impurities present during growth, or displacement defects due to energetic interactions such as fission. Although hydrothermal growth provides s.c. $UO_2$, substitutional or displacement defects are likely present.

All crystals contain bulk and surface defects that interrupt crystal periodicity. This ultimately reduces carrier lifetime and mobility through the production of scattering and recombination sites. Interstitial impurities and lattice vacancies are intrinsic defects that occur between regular lattice sites. Since interstitial impurities are point defects in most crystalline solids, the interstitials are high-energy defects and uncommon [22]. Lattice vacancies are the most prominent point defect in most crystals. Since a site must be vacant for an atom to occupy it, the diffusion rate in the crystal lattice is strongly dependent on the concentration and type of lattice vacancies.

Ordered compounds are capable of having more complex intrinsic defects. Intrinsic defects disrupt the local charge balance, resulting in relaxation to restore equilibrium. For example, an isolated ion vacancy such as oxygen in $UO_2$ creates a region of excess positive charge. This excess positive charge can be compensated by a nearby uranium vacancy. A neutral defect, such as a Frenkel defect, occurs when a lattice vacancy is created, and the displaced atom

is locally resident as an interstitial. In lesser ionized compounds an anti-site defect, where the cation and anion exchange sites, is also energetically possible [22].

Extrinsic defects originate from impurities or solutes intentional or unintentionally added to the material. The foreign atom may occupy a lattice site as a substitutional solute, substitutional impurity, or it may likewise fill an interstitial site as an interstitial solute. Due to the space limitation of interstitial sites, impurity atoms are limited by their size. Smaller atoms are usually found on interstitial sites, while larger atoms are usually substitutional.

Since $UO_2$ is an ionic compound, when the valence of a substitutional defect differs from that of the lattice ion the excess charge is often compensated by a paired vacancy or interstitial. This occurs within $UO_2$ for oxygen ions with a formal -2 charge when they are replaced by anions with a formal charge of -3. The new anion would tend to be paired with vacancies on the oxygen sublattice to maintain charge neutrality [22].

Dislocations are linear defects occurring in a crystal when an excess atom is added or an atom is deleted from the crystal and crystallographic registry is lost. The defect affects the yield strength and creates plastic deformation at ordinary temperatures [22].

Extrinsic doping is a type of defect (usually intentional), in which a substitutional atom is inserted into a semiconductor to control the type and concentration of the majority charge carriers. Device conductivity increases when extrinsic solutes add excess electrons, since the excess electron can only reside in an excited state and orbit the ion core. Therefore, less energy is required to free the orbiting electron and it is easily transported through the lattice.

### 1.4 $UO_2$ Surface Morphology

To gain a preliminary understanding of the oxidation of the surface of the hydrothermally grown s.c. $UO_2$, a sample was measured in the scanning electron microscope. Surface and edge

stoichiometries were compared using Electron Dispersion Spectroscopy (EDS) while imaging the $UO_2$ surface. Figure 3(a) provides a view of the surface edge. The atomic composition of the $UO_2$ crystal was measured from the upper edge to the surface. The measurements shown in Figure 3(b) and 3(c) are representative of the edge, edge–to-surface transition, and surface of the s.c. $UO_2$. Figure 3(b) presents a surface with 20.2% uranium and 79.8% oxygen. Figure 3(c) presents a surface with 26.3% uranium and 73.7% oxygen. Figure 3(d) presents a surface with 29.3% uranium and 70.3% oxygen. The surface measurements provided an average of 27.1 ± 1.6% uranium and 72.9 ± 1.5% oxygen, indicating little surface variation. These results demonstrate the oxidation variations with respect to crystal orientation and surface boundaries.

### 1.5. Thorium Dioxide and $U_{0.71}Th_{0.29}O_2$ Characteristics

One option to form a $UO_2$ heterojunction p-n diode is with $ThO_2$ because $UO_2$ and $ThO_2$ have similar crystal properties. Both have a fluorite crystal structure with 12 atoms, similar ionic radii, and are of the $Fm\bar{3}m$ space group [23]. Likewise, the lattice interatomic spacing of $ThO_2$ is 5.59 Å, which is a 2.2% lattice mismatch from the $UO_2$ lattice spacing of 5.47 Å. The $ThO_2$ melting point is 3650 K, 257 K higher than $UO_2$. The ionic radius of $Th^{4+}$ is 0.119 nm, only 0.005 nm larger than the ionic radius of $U^{4+}$ [23]. However, the 5*f* shell electrons are absent from the optical band gap of $ThO_2$, which makes it an insulator.

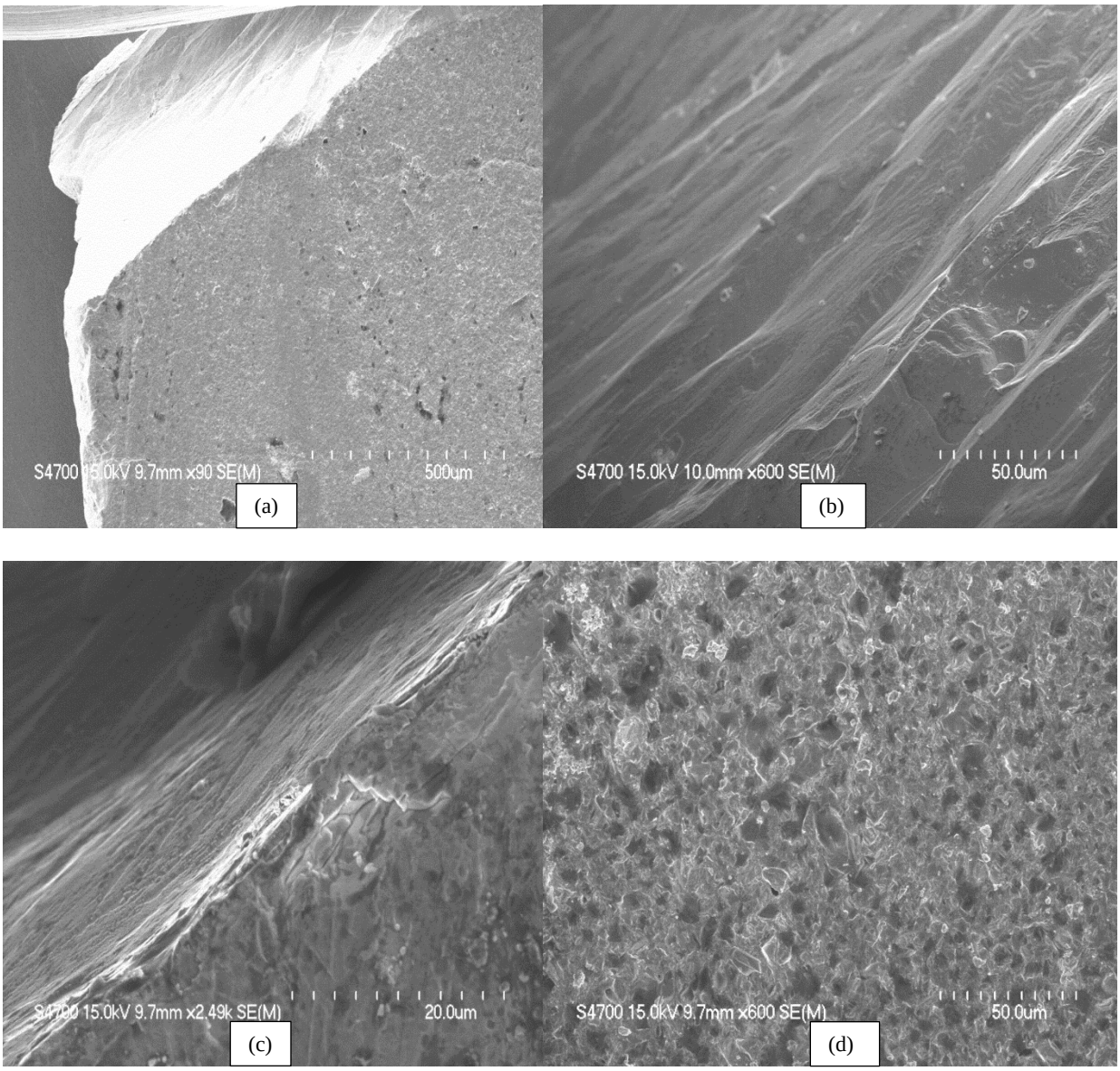


**Figure 3. SEM images of surfaces and edges of s.c. $UO_2$.**

A $U_{0.71}Th_{0.29}O_2$ alloy was studied as a potential alternative to $UO_2$ because of its potential resistance to oxidation. Because of its size and the uniqueness of the growth method, we further considered its potential value to the nuclear fuel industry, especially regarding stability and heat capacity. A literature review of alloyed $U_xTh_{1-x}O_2$ provides few research results in this area apart from a uranium/thorium phase diagram published in 1958, most likely of an amorphous uranium

compound detailing the insolubility of thorium in uranium and no evidence of intermetallic compounds [24].

### 1.6 Research Measurements and Methods

This research investigated the characteristics of hydrothermally-grown s.c. actinide-oxide crystals that can be used as the detection medium for a solid-state neutron detection system. These crystals have the potential to act as the detection medium in a neutron detector that has no need for a conversion layer or neutron moderator. Such a detector, if fabricated with favorable electronic performance, would have great potential for high efficiency neutron detection, yielding small, efficient, low-power devices. The materials studied included $UO_2$ as a detection medium, $ThO_2$ to form a heterojunction electronic interface, and $U_{0.71}Th_{0.29}O_2$ alloy as a potential alternative to $UO_2$ because of its potential resistance to oxidation.

Although actinide oxides have been studied for nearly a century, there still exists an incomplete understanding of the physical and electrical properties of s.c. $UO_2$, $ThO_2$, and their alloys, particularly regarding $UO_2$ surface reactivity and its effect on contact placement and device fabrication. To address this concern, this research investigated the surface electrical structure and interface properties of $UO_2$ using Hall effect, current/voltage measurements I(V), capacitance/voltage measurements C(V), capacitance/frequency measurements C(ω), conductance/frequency measurements G(ω), ellipsometry, x-ray photoemission spectroscopy (XPS), modulated differential scanning calorimetry (MDSC), angle resolved photoemission spectroscopy (AR-XPS), and cathodoluminescence spectroscopy (CL). The Debye temperature and specific heat capacity of a $U_{0.71}Th_{0.29}O_2$ alloy was studied to better understand $UO_2$ surface oxidation and determine if bulk properties were being accessed using the present research techniques. Table 1 provides a summary of experimental techniques, and methods performed on

each actinide oxide during this research. Since the materials used in this study represent large s.c. actinide-oxide samples, we further considered their potential value to the nuclear fuel industry, especially regarding stability and heat capacity.

**Table 1. Summary of actinide oxides measured, experimental methods employed, and desired experimental outcomes.**

| SUMMARY OF MEASUREMENTS AND METHODS | | | | | |
|---|---|---|---|---|---|
| **MEASUREMENT OR METHOD** | s.c. $UO_2$ | $UO_2$ grown on $CaF_2$ | s.c. $ThO_2$ | $UO_2$[i] | $U_{0.71}Th_{0.29}O_2$ |
| I(V) and Hall Effect | mobility, contact type, conductivity | | | | |
| C(V), C(ω), G(ω) | | diffusion carrier lifetime | | | |
| Ellipsometry | crystal quality, complex dielectric constant, electronic transitions | | | | |
| XPS | specific heat capacity | | specific heat capacity | | Debye temperature & specific heat capacity |
| MDSC | specific heat capacity | | specific heat capacity | | |
| AR-XPS | depth-resolved oxidation states | | | | |
| CL | band gap transitions | | | | |

1.7 References


[1] R. Stone, "Researchers Rise to Challenge of Replacing Helium-3," *Science,* vol. 353, no. 6294, pp. 15-16, 2016.

[2] A. Caruso, R. B. Billa, S. Balaz, J. I. Brand and P. A. Dowben, "The Heteroisomeric Diode," *Journal of Physics Condensed Matter,* vol. 16, pp. L139-L146, 2004.

[3] A. Caruso, P. A. Dowben, S. Balkir, N. Schemm, K. Osberg, R. W. Fairchild, O. B. Flores, S. Balaz, A. D. Harken, B. W. Robertson and J. I. Brand, "The All Boron Carbide Nuetron Detector: Comparison with Theory," *Material Science Engineering B,* vol. 135, pp. 129-133, 2006.


[i] This sample was an amorphous $UO_2$ nuclear fuel pellet used for comparison to hydrothermally grown $UO_2$.

[4] N. Hong, J. Mullins, K. Foreman and S. Adenwalla, "Boron Carbide Based Solid State Neutron Detectors: the Effects of Bias and Time Constanton Detection Efficiency," *Journal of Physics D: Applied Physics,* vol. 43, no. 27, 2010.

[5] G. Peterson, Q. Su, Y. Wang, P. A. Dowben and M. Nastasi, "Improved P-N Heterojunction Device Performance Induced by Irradiation in Amorphous Boron Carbide Films," *Material Science Engineering B,* vol. 202, pp. 25-30, 2015.

[6] K. Krane, Introductory Nuclear Physics, Hoboken: John Wiley & Sons, 1988.

[7] C. A. Kruschwitz, S. Mukhopadhyay, D. Schwellenbach, T. Meek, B. Shaver, T. Cunningham and J. Auxier, "Semiconductor Neutron Detectoers Using Depleted Uranium Oxide," in *SPIE 9213, Hard X-Ray, Gamma-Ray, and Neutron Detector Physics XVI, 92130C,* San Diego, 2014.

[8] A. Caruso, J. Petrosky, J. McClory, P. Dowben, W. Miller, T. Oakes and A. Bickley, "Apparatus and Method for Directional and Spectral Analysis of Neutrons". United states Patent US20120148004 A1, 14 June 2012.

[9] G. Leinder, T. Cardinaels, K. Binnemans and M. Verwerft, "Accurate Lattice Parameter Measurements of Stoichiometric Uranium Dioxide," *Journal of Nuclear Materials,* vol. 459, pp. 135-142, 2015.

[10] R. A. Schueneman, A. Khaskelis, D. Eastwood, W. Ooij and L. Burggraf, "Uranium Oxide Weathering: Spectroscopic and Kinetics," *Journal of Nuclear Materials,* vol. 323, pp. 8-17, 2003.

[11] E. Echeverría, B. Dong, G. Peterson, J. P. Silva, E. R. Wilson, M. S. Driver, Y. S. Jun, G. D. Stucky, S. Knight, T. Hoffman, Z. K. Han, N. Shao, Y. Gao, W. N. Mei, M. Nastasi, P. A. Dowben and J. A. Kelber, "Semiconducting Boron Carbides with Better Charge Extraction through the Addition of Pyridine Moieties," *Manuscript Prep,* 2016.

[12] H. Anderson, E. Fermi and L. Szilard, "Neutron Production and Absorption in Uranium," *Phys. Rev.,* vol. 56, pp. 284-286, 1939.

[13] T. T. Meek and B. v. Roedern, "Semiconductor Devices Fabricated from Actinide Oxides," *Vacuum,* vol. 83, pp. 226-228, 2008.

[14] B. von Roedern, T. Meek and M. Haire, "Some Electrical Properties of Ion-Implanted Urania - Part II," in *Symposium of the Society for the Advancement of Material and Process Engineering (SAMPE)*, Long Beach, 2003.

[15] C. Kruschwitz , S. Mukhopadhyay, D. Schwellenbach, T. Meek and B. Shaver, "Semiconductor neutron detectors using depleted uranium oxide," in *Proc. SPIE 9213; Hard X-Ray, Gamma-Ray, and Neutron Detector Physics XVI*, San Diego, 2014.

[16] J. Schones, "Optical Properties and Electronic Structure of UO2," *Journal of Applied Physics*, vol. 49, no. 3, pp. 1463-1465, 1978.

[17] J. Katz and E. Rabinowitch, "Physical Properties of Uranium Metal," in *The Chemistry of Uranium*, New York, McGraw-Hill Book Company, 1951, p. 133.

[18] L. Lynds, W. Young, J. Mohl and G. Libowitz, "X-ray and Density Study of Nonstoichiometry in Uranium Oxides," in *Nonstoichiometric Compounds*, American Chemical Society, 1963, pp. 58-65.

[19] B. Dorado, G. Jomard, M. Freyss and M. Bertolus, "Stability of Oxygen Point Defects in UO2 by first-principles DFT+U Calcuations: Occupation Matrix Control and Jahn-Teller Distortion," *Physical Review B*, vol. 82, 2010.

[20] T. Kelly, J. Petrosky, D. Turner, J. McClory, J. Mann, J. Kolis, X. Zhang and P. Dowben, "The unoccupied electronic structure characterization of hydrothermally grown ThO2 single crystals," *Physica Status Solidi RRL*, vol. 8, no. 3, pp. 283-286, 2014.

[21] C. Young, *Evaluation of Hydrothermally Synthesized Uranium Dioxide For Novel Semiconductor Applications*, Wright Patterson AFB: Air Force Institute of Technology, 2016.

[22] J. W. Morris, "A Survey of Materials Science," 2007. [Online]. Available: http://www.mse.berkeley.edu/groups/morris/MSE205/Extras/defects.pdf . [Accessed 10 02 2017].

[23] L. Morss, N. Edelstein, J. Fuger and J. Katz, The Chemistry of the Actinide and Transactinide Elements, Netherlands: Springer, 2006.

[24] F. Rough and A. Bauer, "Constitution of Uranium and Thorium Alloys," US Government, Columbus, 1958.

[25] G. W. Hohne, W. F. Hemminger and H. J. Flammershiem, Differential Scanning Calorimetry, New York: Springer, 2003.

[26] C. Young, J. Petrosky, J. M. Mann, E. Hunt, D. Turner and P. A. Dowben, "The Lattice Stiffening Transition in UO2 Single Crystals," *Journal of Physics: Condensed Matter,* vol. 29, no. 3, 2016.

[27] J. Holz, F. K. Schulte and H. Wagner, Solid Surface Physics, Berlin: Springer Berlin Heidelberg, 1979.

[28] R. C. Chiechi, E. A. Weiss, M. D. Dickey and G. M. Whitesides, "Eutectic Gallium-Indium (EGaIn): A Moldable Liquid Metal for Electrical Characterization of Self-Assembled Monolayers," *Angewandte Chemie,* vol. 120, pp. 148-150, 2007.

[29] S. M. Sze and K. K. NG, Physics of Semiconductors Devices, Wiely-Interscience, 2007.

[30] E. Borchi, M. Bruzzi, S. Pirollo and S. Sciortino, "Temperature and Frequency Dependence of the Capacitance of Heavily Irradiated Silicon Diodes," *Solid-State Electronics,* vol. 42, no. 11, pp. 2093-2096, 1998.

[31] B. T. Wilis, "The Defect Structure of Hyper-Stoichiometric Uranium Dioxide," *Acta Crystallogr.,* vol. Sect.A, no. 34, pp. 88-90, 1978.

[32] I. D. Parker, "Carrier Tunneling and Device Characteristics in Polymer Light-Emitting Diode," *Journal of Applied Physics,* vol. 75, pp. 1656-1666, 1994.

[33] J. S. Morrell and M. J. Jackson, Uranium Processing and Properties, New York: Springer, 2013.

[34] K. Gofryk, S. Du, C. Stanek, J. Lashley, X. Liu, R. Schulze, J. Smith, D. Safarik, D. Byler, K. McClellan, B. Uberuaga, B. Scott and D. Andersson, "Anisotropic Thermal Conductivity in Uranium Dioxide," *Nature Communications,* vol. 5, no. 4551, 2014.

[35] A. Mock, R. Korlacki, C. Briley, D. Sekora, T. Hofmann, P. Wilson, A. Sinitskii, E. Schubert and M. Schubert, "Anisotropy, Band-to-Band Transitions, Phonon MOdels, and Oxidation Properties of Cobalt-Oxide Core-Shell Slanter Columnar Thin Films," *Applied Physics,* vol. 108, no. 5, 2016.

[36] W. Siekhaus and J. Crowhurst, "Optical Properties of a Mechanically Polished and Air-Equilibrated [111] UO2 Surface by Raman and Ellipsometric Spectroscopy," in *IOP Conference Series: Materials Science and Engineering, Volume 9, Number 1*, 2010.

[37] S. Hufner, Photoelectron Spectroscopy Principles and Applications, New York: Springer, 2003.

[38] B. G. Yacobi, Cathodoluminescence Microscopoy of Inorganic Solids, New York: Plenum Press, 1990.

[39] D. R. Vij, Luminenscence of Solids, New York: Plenum Press, 1998.

[40] M. Fox, Optical Properties of Solids, New York: Oxford University Press, 2010.

[41] J. Schoenes, "Optical Properties and Electronic Structure of UO2," *Journal of Applied Physics*, vol. 49, no. 3, pp. 1463-1465, 2008.

[42] A. Riul Jr., C. Mills and D. Taylor, "The Electrical Characteristics of a Heterojunction Diode Formed from an Aniline Oligomer LB-deposited onto Poly(3-methylthiophene)," *Journal of Materials Chemistry*, vol. 10, pp. 91-97, 1999.

[43] G. Petererson, E. Echeverria, B. Dong, J. Silva, E. Wilson, J. Kelber, M. Nastasi and P. Dowben, "Increased Drift Carrier Lifetime in Semiconducting Boron Carbides Deposited by Plasma Enhanced Chemical Vapor Depsition from Carborands and Benzenes," *Journal of Vacuum Science & Technology A: Vacuum Surfaces, and Films*, vol. 35, no. 3, 2016.

[44] H. Fujiwara, Spectroscopic Ellispsometry: Principles and Applications, Tokyo: John Wiley & Sons, 2003.

[45] R. Azzam and N. Bashara, Ellipsometry an Polaized Light, New York: North Holland, 1978.

[46] R. Riedel and I. Chen, Cermanics Science and Technology, Germany: Wiley & Sons, 2010.

[47] "Evaluated Nuclear Data File (ENDF)," IAEA, 09 11 2016. [Online]. Available: https://www-nds.iaea.org/exfor/endf.htm. [Accessed 13 02 2017].

[48] D. Skoog, F. Holler and T. Nieman, Principles of Instrumental Analysis, Orlando: Harcourt Brace & Company, 1998.

[49] J. Goldstein, D. Newbury, P. Echlin, D. Joy, A. Romig, C. Lyman, C. Fiori and E. Lifshin, Scanning Electron Microscopy and X-ray Microanalysis: A Text for Biologists, Materials Scientists, and Geologists, Springer, 1992.

[50] S. M. Sze and K. K. NG, Physics of Semiconductors Devices, Wiely-Interscience, 2007.

[51] D. Vaughan, Energy-Dispersive X-Ray Microanalysis: An Introduction, Middleton: NORAN Instruments, 1999.

[52] A. Lauber, "On the Theory of Compensation in Lithium Drifted Semiconductor Detectors," *Nuclear Instruments and Methods,* vol. 75, pp. 297-308, 1969.

[53] J. A. Woollam, "J.A. Woollam Co. Ellipsometry Solutions," 2016. [Online]. Available: https://www.jawoollam.com/resources/ellipsometry-tutorial/polarized-light. [Accessed 16 02 2017].

[54] J. A. Woollam, "A Short Course in Ellipsometry," [Online]. Available: https://www.nnf.ncsu.edu/sites/default/files/vase_manual_short_course.pdf. [Accessed 16 02 2017].

[55] E. Hecht, Optics, New York: Addison Welsey, 2002.

[56] H. Fujiwara, Spectroscopic Ellipsometry: Principles and Applications, Hoboken: John Wiley & Sons, 2007.

[57] G. Leinders, T. Cardinels, K. Binnemans and M. Verwerft, "Accurtae lattice parameter measurments of stoichioimetric uranium dioxide," *Journal of Nucelar Materials,* vol. 459, pp. 135-142, 2015.

[58] D. J. Kim, J. H. Kim, K. S. Kim, J. H. Yang, S. K. Kim and Y. H. Koo, "Thermodynamic Assessment of UO2 Pellet Oxidation in Mixture Atmospheres under Spend Fuel Pool Accident," *World Journal of Nuclear Science and Technology,* vol. 5, pp. 102-106, 2015.

[59] G. Kresse and J. Furthmuller, "Efficient Iterative Schemes for ab initio Total-Energy Calculations Using a Plane-Wave Basis Set," *Physical Review B,* vol. 54, no. 16, pp. 169-186, 1996.

[60] G. Kresse and J. Hafner, "Ab initio Molecular Dynamics for Liquid Metals," *Physical Review B,* vol. 47, no. 1, pp. 558-561, 1993.

[61] G. Kresse and D. Joubert, "From Ultrasoft Pseudopotentials to the Projector Augmented-Wave Method," *Physical Review B,* vol. 59, no. 3, pp. 1758-1775, 1999.

[62] J. P. Perdew, K. Burke and M. Ernzerhof, "Generalized Gradient Aprpoximation Made Simple," *Physical Review Letters,* vol. 77, no. 18, pp. 3865-3868, 1996.

[63] J. Paier, M. Marsman, K. Hummer, G. Kresse, I. C. Gerber and J. G. Angyan, "Screened Hybrid Density Functionals Applied to Solids," *The Journal of Chemical Physics,* vol. 124, 2006.

[64] E. Sanville, E. Kenny, R. Smith and G. Henkelman, "Improved Grid-Based Algorithm for Bader Charge Allocation," *Journal of Computational Chemistry,* vol. 28, pp. 899-908, 2007.

[65] J. Heyd and G. S. Ernzerhob, "Hybrid Functionals Based ona a Screened Coulomb Potential," *The Journal of Chemical Physics,* vol. 118, pp. 8207-8215, 2003.

[66] H. Monkhorst and J. Pack, "Special Points for Bruillouin-zone Integrations," *Physical Review B,* vol. 13, no. 12, pp. 5188-5192, 1976.

[67] S. Clark, M. Segall, C. Pickard, P. Hasnip, M. Probert, K. Refson and M. Payne, "First Principles Methods Using CASTEP," *Zeitschrift für Kristallographie - Crystalline Materials,* vol. 220, pp. 567-570, 2005.

[68] D. K. Schroder, Semiconductor Material and Device Characterization, New York: John Wiley & Sons, 1998.

[69] L. J. van der Pauw, "A Method of Measuring Specific Resistivity and Hall Effect of Discs of Arbitrary Shape," *Philips Research Reports,* vol. 13, no. 1, pp. 1-9., 1958.

[70] "NIST Physical Measurement Laboratory Engineering Physics Division," National Insitute of Standards and Technology U.S. Department of Commerce, 15 April 2010. [Online].

Available: https://www.nist.gov/pml/engineering-physics-division/popular-links/hall-effect/hall-effect-figure-2. [Accessed 01 08 2018].

[71] D. A. Neamen, Semiconductor Physics and Devices, New York: McGraw Hill, 2003.

[72] C. L. Dugan, "Cathodoluminescence and Photoemission of Doped Lithium Tetraborate," Air Force Institute of Technology Graduate School of Engineering and Management, Wright-Patterson AFB OH , 2011.

[73] R. Eisbert and R. Resnick, Quantum Physics of Atoms, Molecules, Solids, Nuclei, and Particles, New York: John Wiley & Sons, 1985.

[74] D. R. Tallant, W. L. Warren and C. Seager, "Reflectivity Changes, and Accumulation of Graphitic Carbon during Electron Bem Aging of Phosphors," *Journal of Applied Physics,* vol. 82, p. 4515, 1997.

[75] P. Barnes, "Capacitance Voltage (C-V) Characterization of Semiconductors," *Characterization of Materials,* vol. 1, pp. 456-466, 2002.

## II. Theoretical Basis For Experimental Techniques

The purpose of this chapter is to explain the theory behind the experimental techniques used to compare the electrical and material properties of s.c. $UO_2$, $ThO_2$, and $U_{0.71}Th_{0.29}O_2$. This chapter begins with a general overview of the primary measurement techniques, x-ray photoemission and cathodoluminescence spectroscopy. Subsequent sections provide an overview of supplementary experimental techniques such as Hall effect, I(V), ellipsometry, and MDSC. Initial electrical measurements validated the requirement for an in-depth investigation of the $UO_2$ surface properties. AR-XPS provided a depth-resolved study of $UO_2$'s surface stoichiometry. CL confirmed the electronic transitions proposed by ellipsometry and DFT. The material properties

of $ThO_2$ and $U_{0.71}Th_{0.29}O_2$ were also explored as potential device materials using XPS and MDSC.

## 2.1 Primary Experimental Techniques

### *2.1.1 X-ray Photoemission Spectroscopy*

In XPS, monoenergetic x-ray photons illuminate a solid where, through the photoelectric effect, electrons are emitted into a vacuum where their energy is measured using an electron energy analyzer [1]. The primary quantity measured in XPS is the number of electrons emitted at a specific kinetic energy, $E_{kin}$. This tally is assembled to create the photoelectron spectrum. The photoelectron spectrum provides information about the binding energy state of the photoelectron before it was emitted. Figure 4 illustrates the association between the binding energy for various electrons in bound states and the photoelectron energy spectrum. The binding energy, $E_b$, is determined from the energy of the initial incident x-ray, $\hbar\omega$, and the work function, $\phi$, of the sample material, as shown in Equation (2.1) [1].

$$E_{kin} = \hbar\omega - (E_b - \phi) \tag{2.1}$$

In the process, valence band electrons are emitted from the sample first with the highest kinetic energy. Some of the photon's energy is liberated in probing the energy bands associated with the core level electrons, causing them to appear at lower kinetic energies.

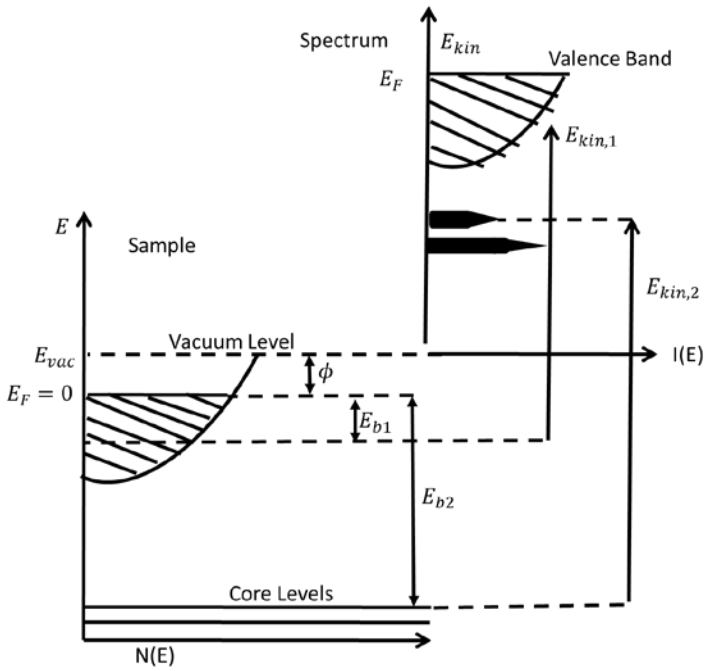


**Figure 4. Generalized energy diagram for photoelectron emission in an XPS measurement. Derived from [1].**

The Fermi level energy, which represents the highest electron energy state at 0 K, is the guideline for understanding the photoemission energy distribution. Determination of the Fermi level for the XPS measurement in the present research is based on the fact that the Fermi level of the $UO_2$ and that of the metal sample holder are at the same potential, as they are metals connected electrically.

For a semiconductor, the photoemission spectrum can provide details about the band structure. The summation of the electron affinity and the bandgap is defined as the energy required for an electron to reach vacuum level. The maximum energy needed to eject an electron to vacuum level can then be defined as $E_{pt}$, the photo-threshold energy. If the x-ray photon energy is equal to or less than $E_{pt}$, then no photoelectrons escape. For photoelectrons from the valence band, $E_{pt}$ equals the energy difference from the top of the valence band to the vacuum level less $\phi$. Furthermore, using semiconductor theory, the electron affinity, $\chi$, is the energy

difference from the conduction band to the vacuum level [1]. These relationships are shown in Equations (2.3), (2.4) and (2.5), where $E_0$ is the energy where photoemission stops, $E_V$ is the energy at the top of the valence band, $E_F$ is Fermi level energy, and $E_g$ is the band gap energy, providing an XPS determined band gap from the extinction of the valence band photoelectron emission.

$$E_{pt} = \hbar\omega - E_V + E_o \tag{2.2}$$

$$\phi = \hbar\omega - E_F + E_o \tag{2.3}$$

$$E_{pt} = \chi + E_g \tag{2.4}$$

Based upon Monte Carlo simulations, 2000 eV electrons have a mean penetration depth in $UO_2$ of ~33 nanometers. Since our PES system uses an Al kα x-ray with a fixed energy of 1486 eV, the XPS essentially measures at the x-ray depth, or the first 20-25 nanometers of the sample surface. In order to provide for depth profiling of the surface to the maximum depth of electron emission, the sample is rotated with respect to the x-ray source in AR-XPS, thus probing less into the material and providing a more surface-sensitive measurement.

### *2.1.2 Cathodoluminescence Spectroscopy*

(Parts of this section are extracted from Dugan 2011 Master's thesis [2] and modified for this dissertation.)

In CL, incident electrons produced by an electron gun are either absorbed or scattered by the atoms in the surface of the solid. This electron energy deposition results in the production of electron-hole pairs, which recombine, resulting in light emission, generally known as luminescence. The emitted photon energy is due to an electronic transition between an initial state, $E_i$, and final state, $E_f$. The energy or wavelength is given by Equation (2.8) [3].

$$E_f - E_i = \frac{hc}{\lambda} = \hbar\omega \tag{2.5}$$

In CL, the energy and intensity of the incident electrons can be varied. Typically, beam energies of 500 eV to 20 keV are used to probe the surface from several nanometers to several hundred nanometers below the surface. A monochromator/photomultiplier system measures the luminescent intensity as a function of wavelength. This allows for select stimulation and excitation transition modes to be measured through a wide range of energies. Thus, by varying the incident electron energy and observing the energy of the emitted photon, the band gap energy and interband gap transition energies can be measured as a function of depth.

Luminescence in semiconductors from conduction to the valence band is explained by the radiative recombination of electron-hole pairs [4]. Intraband transitions can occur when an electron, excited far above the conduction band, decays in energy to the bottom of the conduction band, finally reaching thermal equilibrium with the lattice. This process can result in phonon emissions. (Figure 5-1) Interband transitions can occur by direct recombination of conduction band electrons to holes in the valence band. The result is a broad photon emission spectrum due to transitions from states at or near the corresponding band edges (Figure 5-2) [4].

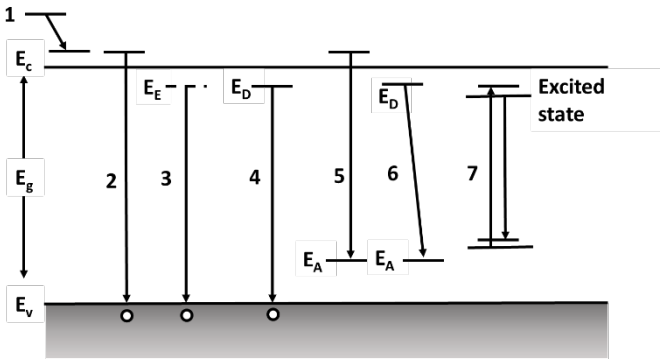


**Figure 5. Schematic diagram of radiative transitions between the conduction band ($E_c$), the valence band ($E_v$) and the exciton ($E_E$), donor ($E_D$) and acceptor levels ($E_A$) in a semiconductor [4].**

More complex transitions can also occur in a CL measurement due to exciton emission. Excitons are a two-particle system similar to a hydrogen atom. An electron in the conduction band orbits a hole in the valence band forming a bound electron-hole pair which is free to move about the lattice. This is a free exciton. With excitonic recombination, the electron and hole recombine, conserving momentum during the transition (Figure 5-3). The energy of light emitted is less than the band gap energy by the binding energy of the exciton. The excitonic energy, $E_x$, which is material dependent, is found by Equation (2.6), where $m^*_r$ is the exciton reduced mass equaling $(m_e m_h)/(m_e+m_h)$ where $m_e$ is the electron mass and $m_h$ the hole mass, $q$ is the charge of an electron, $h$ is Planck's constant, $\varepsilon$ is dielectric constant, and $n_q$ is the quantum number [3].

$$E_x = \frac{m_r^* q^4}{2h^2 \varepsilon^2 n_q^2} \tag{2.6}$$

Electron transitions from a donor site to the valence band, or from the conduction band to an acceptor site can produce extrinsic luminescence, revealing information about the donor or acceptor intraband energy. (Figure 5-4 and 5-5). Transitions from a donor to acceptor site, often called a donor-acceptor pair (DAP) recombination can occur producing extrinsic luminescence, with lower energy than the band gap energy (Figure 5-6). Carriers trapped at donor or acceptor sites produce neutral donors and acceptors. When the donor and acceptor recombine, it produces extrinsic luminescence, with energy lower than the band gap energy. The emitted photon energy from a DAP recombination is given by Equation (2.7). In Equation (2.7), $E_{g,A,D}$ are the energies of the gap, acceptors and donors respectively, $r$ is the distance between the donor and acceptor, $b$ is an adjustable Van der Waals parameter, and $\varepsilon$ is the dielectric constant. The coulomb interaction between the donor acceptor pairs separated by $r$ is $q^2/\varepsilon r$, and $q^2 b^5/\varepsilon r^6$ is the polarization term only applicable to very close pairs. When $r$ is large the discrete lines form a

continuum and a broad DAP band is observed [3]. Excitation and radiative de-excitation of an impurity within incomplete inner shells is shown in 5-7.

$$\hbar\omega = E_g - E_A - E_D + \frac{q^2}{\varepsilon\, r} - \frac{q^2 b^5}{\varepsilon\, r^6} \tag{2.7}$$

Transitions between deep donors and acceptors will have recombination emissions with lower photon energies than the band gap. Shallow donors or acceptors will have transition energies near the energy of the band gap. Therefore, to distinguish between band-to-band transitions from shallow donor and acceptors, the sample must be cooled to reduce thermal broadening and acoustic phonon interference, and hence increase the signal-to-noise ratio [3].

Since $UO_2$ is determined to be a material with an optical band gap of ~5 eV, the electron beam can excite electrons that will relax and produce photons at wavelengths as short as 2400 Å, the so-called "vacuum ultraviolet" portion of the optical spectrum. The 2.1 eV electronic band gap of $UO_2$ will provide photons at wavelengths of ~5900 Å which are within the visible spectrum.

The electron depth of penetration is a function of the electron energy and the material. Since $UO_2$ has a large atomic number, electrons scatter from the nucleus according to Rutherford scattering with a few constraints. The nuclear radius is no larger than the distance of approach and the nuclear force is considered a Coulomb force between two point charges. Analytically, the total number of electrons scattered into a solid angle $d\Omega$ at a scattering angle $\theta$ is the differential cross-section $d\sigma/d\Omega$, given by Equation (2.8).

$$\frac{d\sigma}{d\Omega} = \left(\frac{1}{4\pi\epsilon_0}\right)^2 \left(\frac{Zq^2}{2m_e v^2}\right)^2 \frac{1}{sin^4(\theta/2)} \tag{2.8}$$

In Equation (2.8) $Z$ is the atomic number of the target atom, $m_e$ is the electrons mass, $v$ is the electron velocity, $q$ is the elementary charge, and $\epsilon_0$ is the permittivity of free space. The solid angle $d\Omega$ is given by Equation (2.9), where θ is the scattering angle [5].

$$d\Omega = 2\pi \sin(\theta)\, d\theta \tag{2.9}$$

Bethe provides a method to determine the mean rate of energy loss due to scattering (stopping power) owing to electromagnetic interactions between two charged particles. Bethe includes energy losses due to ionization, leaving one (or both) particles involved in the collision in an excited state. For electrons traveling through a material, the mean energy loss per distance traveled (S) is determined using Equation (2.10) [6].

$$\frac{dE}{dS} = -2\pi q^4 N_A \frac{\rho Z}{EA} \ln\left(\frac{1.166E}{J}\right) \tag{2.10}$$

In Equation (2.10), the charge of the electron is $q$, Avogadro's number is $N_A$, density is $\rho$, the atomic weight is $A$, the mean incident kinetic electron energy is $E$, and $J$ is the mean ionization potential given by Equation (2.11).

$$J = (9.76Z + 58.5Z^{-19})10^{-3} \tag{2.11}$$

Conventional Monte Carlo calculations combine both the Rutherford and Bethe equations, to determine the distance travelled through a material. Electron trajectory simulations are used to sample electrons as they elastically and inelastically scatter and backscatter within the sample. The electron path is then calculated in a stepwise manner. The electron trajectory in the material is modeled as a series of random collisions, where the electron scatters by a random scattering angle, $W$. Between these collisions the electron is assumed to travel in a straight line. The energy loss from elastic collisions is continuous and given by Equation (2.12), where $\lambda$ is the mean free path from the total scatter cross section, as in Equation (2.13) [6].

$$S = -\lambda ln(|W|) \tag{2.12}$$

$$\lambda = \frac{A}{N_a \rho \sigma} \tag{2.13}$$

Energy loss is then calculated from *dE/dS*, and the process is repeated for the lower energy electron and a random angle *W* until the electron energy is lower than the material ionization energy. The Monte Carlo method must be calculated for a large number of trajectories to provide low numerical error. The Monte Carlo method confirms that a substantial fraction of energy dissipated occurs in a small volume where the electron beam impacts the surface [3].

Since the Bethe equation is derived from the Born approximation, it loses accuracy when low energy electrons scatter and gain a large transverse momentum [7]. A similar case can be made for electron interactions with high Z materials. To account for this, Win-X-ray, (a Monte Carlo electron transport code, uses Mott total cross sections for electrons <30 keV and Rutherford total cross elastic cross-sections for electrons >30 keV [8]. Using Win X-ray, a 20 keV electron would penetrate $UO_2$ a maximum penetration depth of 1020 nanometers, with an average penetration depth of 790 nanometers.

## 2.2 Supplementary Experimental Techniques

### *2.2.1 Hall Effect, I(V), and C(V) Characteristic Curves*

The van der Pauw technique was used to provide sample resistivity, carrier density, carrier type, and mobility. Four metal contacts were mechanically placed on the surface of the sample. A constant current was chosen to maximize the voltage applied while the current was measured.

To account for the arbitrary shape of a sample, van der Pauw has shown it necessary to measure voltage across two adjacent contacts when a current is passing through the other two contacts. Van der Pauw demonstrated there are two characteristic resistances, $R_A$ and $R_B$ associated with the terminals as shown in Figure 6. $R_A$ is equivalent to $(R_{21,34}+R_{12,43}+R_{43,12}+R_{34,21})/4$. Likewise $R_B$ is equivalent to $(R_{32,41}+R_{23,14}+R_{14,23}+R_{41,32})/4$ where $R_{21,34} = V_{34}/I_{21}$. The sheet resistance, $R_S$, defined in Equation (2.14) is numerically solved via multiple measurements [9].

$$e^{(-\pi R_A/R_S)} + e^{(-\pi R_B/R_S)} = 1 \tag{2.14}$$

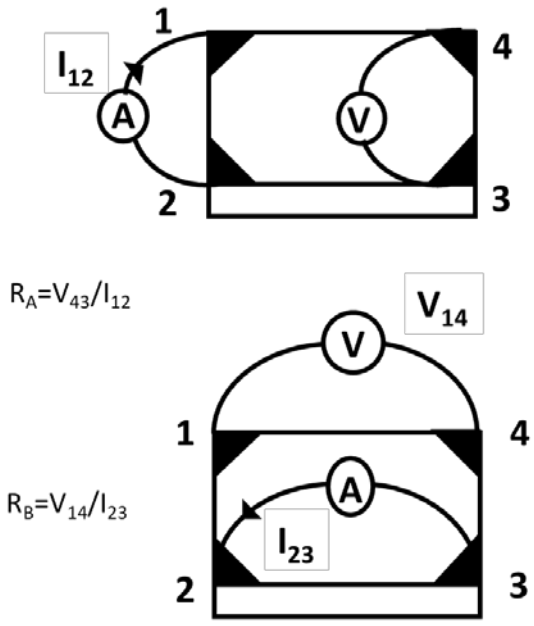


**Figure 6. Schematic of a van der Pauw configuration used in the determination of the two characteristic resistances. A component of $R_A$ and $R_B$ is presented [9].**

Sheet resistivity, $\rho_s$ is then calculated by multiplying the sheet resistance by the sample thickness as defined in Equation (2.15).

$$\boldsymbol{\rho = R_s d} \tag{2.15}$$

A magnetic field is now applied perpendicular to the direction of current flow producing an electric field perpendicular to the direct of the current [10]. The current is measured again as a function of voltage. The summation of the measured voltages provide the Hall voltage, $V_H$, and is defined in Equation (2.16).

$$V_H = \frac{IB}{qn_s} \tag{2.16}$$

In Equation (2.16), $I$ is the current, $q$ is the elementary charge, $B$ is the magnetic field, and $n_s$ is the sheet carrier concentration. If the Hall voltage is positive, the majority carrier is holes. The carrier concentration is found in Equation (2.16). The carrier concentration (2.16) and sheet resistance (2.15) are then combined to provide the carrier mobility, $\mu$ in Equation (2.17) [9].

$$\mu = \frac{1}{qR_s n_s} \tag{2.17}$$

Current-voltage, I(V), curves show the relationship between current flowing through an electronic materials and the applied voltage. Due to Ohm's law, resistors result in a linear I(V) relationship with a slope equivalent to the inverse of resistance. Unlike resistors, the I(V) curves associated with Schottky diodes and p-n junctions show rectification, or preferentially allowing current flow in one direction based upon carrier barriers and charge availability. The current-voltage relationship for a p-n junction is described in Equation (2.18).

$$I(V_a) = I_s \left[ exp\left(\frac{qV_a}{n_i kT}\right) - 1 \right] \tag{2.18}$$

The abrupt diode current-voltage relation is modeled in Equation (2.18) with Maxwell-Boltzmann statistics, where $I_s$ is the saturation current, $q$ is the elementary charge, $V_a$ is the

applied voltage, $k$ is Boltzmann's constant, $T$ is the temperature in K, and $n_i$ is an ideality factor. For a large forward bias, $n_i$ is equivalent to 1 [11]. Since the ideal diode equation assumes all electron-hole band-to-band or by trap assisted recombination occurs in the bulk, $n_i$ accounts for leaking due to avalanching, junction trap-assisted tunneling, and radiation damage.

When $V_a$ is negative, the junction is said to be in reverse bias, representing minority carrier injection across the junction. Accordingly, the term in brackets in Equation (2.18) approaches -1 so that $I(V_a)$ approaches $-I_s$, which is proportional to minority carrier concentration and inversely proportional to the square root of the minority carrier lifetime. The saturation current is generally small. This does not account for non-ideal factors, such as tunneling, which are enhanced at high voltages or can dominate carrier recombination when the defect population is high. When $V_a$ is positive, the diode is in forward bias, representing majority carrier injection across the junction. In Equation (2.18) the exponential dominates and the $I(V_a)$ relationship is generally exponential with $V_a$.

Important to neutron detection, the flow of current through the diode represents a background noise, against which the neutron signal competes. Typically detectors function in the reverse bias condition so that the small injection of carriers from radiation must only compete with minority carrier flow. This implies the need for high doping (reducing minority carrier) and long minority carrier lifetimes in radiation detection media [11].

Hillibrand and Gold found C(V) measurements provide information about a semiconductor's dopant concentration and diffusion potential [12]. In addition, a metal-semiconductor or p-n junction's effective barrier height can be extrapolated from the plot of $1/C^2$. Additionally, capacitance and conductance are frequency dependent, based upon trap lifetime. This can be exploited to determine if device transport is trap dominated.

Drift carrier lifetime can be modeled by comparing the measured C(V) curve and the modeled diffusion capacitance in the region of low forward bias. The frequency-dependent diffusion capacitance, $C_D$, is given by Equation (2.19).

$$C_D = \frac{G_0}{\omega\sqrt{2}}(\sqrt{1+\omega^2\tau^2}-1)^{1/2} \tag{2.19}$$

In Equation (2.19) $\omega$ is the angular frequency ($2\pi f$), and $\tau$ is the drift carrier or effective carrier lifetime. The low frequency conductance, $G_0$, is calculated from the d.c. I(V) values by numerical differentiation. Utilizing $G_0$ and $f$ from the measurement, $\tau$ can be iteratively adjusted to ensure the $C_D$ curve fits the C(V) data. The lifetime, $\tau$, controls the height and the slope of the modeled $C_D$ to the measured C(V) data and yields a drift carrier lifetime.

### *2.2.2 Ellipsometry Technique*

Ellipsometry is a very sensitive surface measurement utilizing the relative phase change of polarized light, or how the p- and s-wave components change upon reflection or transmission in relation to each other. The measurement response is dependent on the complex dielectric constant, the complex index of refraction, and sample thickness. Outputs from ellipsometry include optical properties, film thickness crystallinity, roughness, doping concentration, and material characterization. VASE, or variable angle spectroscopic ellipsometry, increases the spectral acquisition range and angles of incidence for a sample. This allows for a wider range of samples and structures.

Ellipsometry measures the electric field behavior of light in space and time, or polarization. The electric and magnetic field wave are orthogonal to the direction of propagation. Polarized light follows a specific path and traces out a distinct shape at any point. When two

orthogonal electric and magnetic fields are of arbitrary amplitude and phase, they are of elliptical polarization as shown in Figure 7.

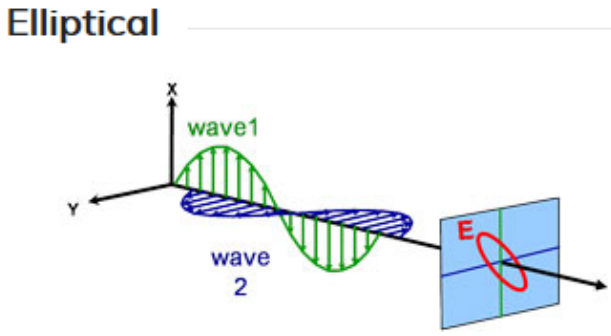


**Figure 7. Two electromagnetic waves traveling orthogonal to the direction of propagation with arbitrary amplitude and phase [13].**

Equation (2.20) is the electric field wave equation solution for the electromagnetic plane wave.

$$\vec{E}(r,t) = \vec{E}_0 e^{\left(\frac{i2\pi\tilde{n}}{\lambda}\vec{q}\cdot\vec{r}\right)} e^{(-i\omega t)} \tag{2.20}$$

In Equation (2.20) the unit vector along the direction of wave propagation is $\vec{q}$, $\tilde{n}$ is the complex index of refraction $n + ik$, $\lambda$ is the wavelength of light in a vacuum, $\omega$ is the wave angular frequency, $\vec{r}$ is the distance traveled, and $\vec{E}_0$ is a complex vector constant specifying the wave amplitude and polarization state. Multiplying the first exponential term by the complex index of refraction allows for the deconvolution of Equation (2.20). As $\vec{r}$ increases, the wave's amplitude may change as indicated by the $e^{-\frac{2\pi k}{\lambda}(\vec{q}\cdot\vec{r})}$term. How the wave changes in space is represented by the $e^{\frac{2\pi in}{\lambda}(\vec{q}\cdot\vec{r})}$ term. Finally the $e^{(-i\omega t)}$ component addresses how the wave oscillates in time. Since the electric field and magnetic field are perpendicular, only the electric field wave is needed to define a plane wave.

The complex index of refraction determines how a plane wave oscillates. If the imaginary part of $\tilde{n}$ is non-zero, the wave's amplitude will decay exponentially while it propagates. If the wave is assumed to be propagating in the z-direction, the decay will occur according to Equation (2.21).

$$\vec{E} \propto exp(-\frac{2\pi kr}{\lambda}) \tag{2.21}$$

In Equation (2.21) *k* is the extinction coefficient, as it represent the decay of the wave through the material, *r* is the propagation distance in length units, and $\lambda$ is the wavelength of light in length units [14]. The wave decays to 1/e of its original amplitude after propagating $D_p$, or the penetration depth defined by Equation (2.22).

$$D_p = \frac{\lambda}{2\pi k} \tag{2.22}$$

If *k* is large, then the light does not penetrate readily. For ellipsometry, light must penetrate the surface and propagate back out after it reflects from an interface. Experimentally, for metal films greater than 50 nm, ellipsometry is not possible due to the inability of light to traverse to the interface and return to the detector.

According to Maxwell, the divergence of the displacement field must equal the local charge density by Equation (2.23) [14]. In Equation (2.23) $\rho_c$ is the charge density.

$$\vec{\nabla} \cdot \vec{E} = \frac{\rho_c}{\varepsilon} \tag{2.23}$$

If the material is isotropic and absent of space charge, $\rho_c$ is zero, Equation (2.23) reduces to Equation (2.24) requiring the components of the polarization vector, $\vec{E}_0$ to lie in the plane perpendicular to the direction of beam propagation. Therefore, the polarization state of any beam can be explained by its components along any two orthogonal axes in the plane perpendicular to the beam's propagation direction [14].

$$\vec{\nabla} \cdot \vec{E} = 0, \tag{2.24}$$

Ellipsometry uses the p- and s- directions as the two orthogonal basis vectors to convey beam polarization states as depicted in Figure 8. The p- direction is perpendicular to the sample's flat surface and the s- direction lies parallel to the surface, where the cross product of p and s provide the direction of wave propagation via the Pointing vector [14].

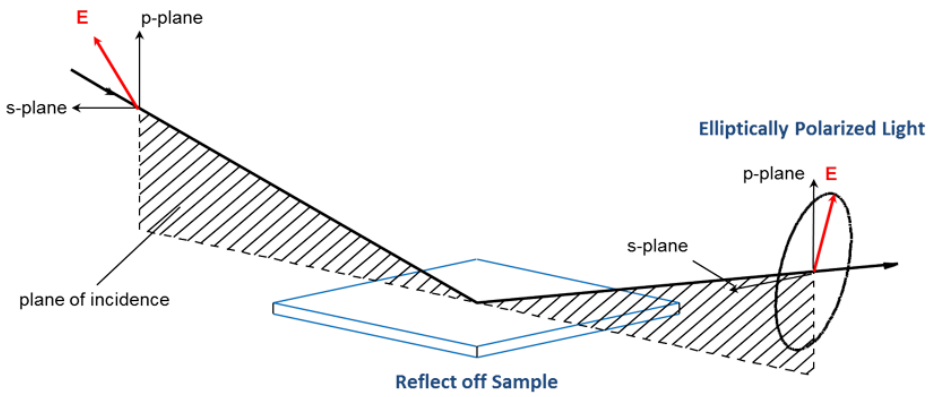


**Figure 8. Geometry of an ellipsometric experiment displaying the s- and p- directions [13].**

The total polarized beam can be expressed by the components of the beam's electric field along the p- and s- directions. In ellipsometry, a laser light source is sent through a polarizer allowing light of a preferred electric field orientation to pass. This polarized light reflects from the sample surface, changes polarization, and travels through a combined continuously rotating polarizer and analyzer. Then the detector converts the light to an electric signal to determine the reflected polarization [14].

A simplistic model of light reflecting from a surface in air is shown in Figure 8. It provides $r_p$, and $r_s$, (Equation (2.25) and Equation (2.26)) with $\tilde{n}_0$ and $\tilde{n}_1$ being the complex refractive indices of air and the sample respectively [15].

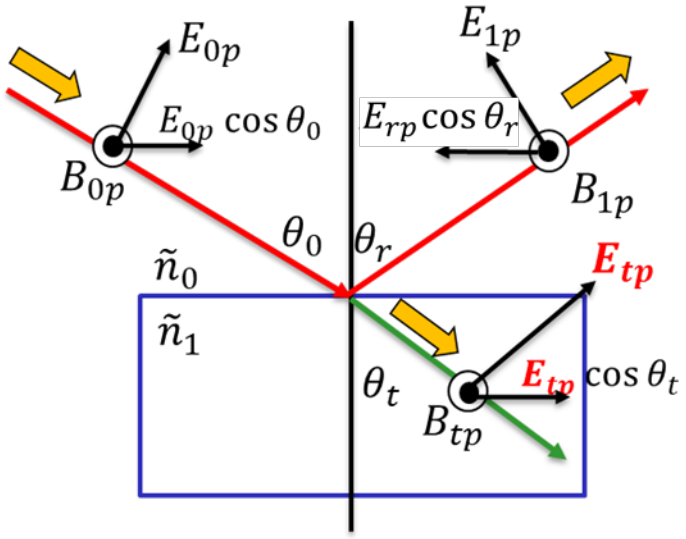


**Figure 9. Electric field and magnetic field for p- polarization. The magnetic field, *B*, is perpendicular to the plane of the page and is pointing toward the reader [13].**

$$r_p = {E_{rp}}/{E_{0p}} = \left(\frac{n_1\,cos(\theta_o) - n_0\,cos(\theta_t)}{n_1\,cos(\theta_o) + n_0\,cos(\theta_t)}\right) \tag{2.25}$$

$$r_s = {E_{rs}}/{E_{0s}} = \left(\frac{n_0\,cos(\theta_o) - n_1\,cos(\theta_t)}{n_0\,cos(\theta_o) + n_1\,cos(\theta_t)}\right) \tag{2.26}$$

The transmission angle, $\theta_t$, can be calculated from the incident angle, $\theta_o$, using Snell's law [15]. The polarization change is represented as an amplitude ratio,$\Psi$, and the phase difference, $\Delta$. The $\Psi$ and $\Delta$ are related to the ratio of Fresnel reflection coefficients, $r_p$and $r_s$ for p- and s- polarized light. The change in amplitude,$\Psi$, is found by Equation (2.27) where $\Delta$ is given in polar coordinates by Equation (2.29), assuming $\tilde{n} \equiv n + ik$ [15].

$$\rho_e \equiv \frac{r_p}{r_s} = tan(\Psi)\,e^{i\Delta} \tag{2.27}$$

$$\Delta = arg(\rho_e) = \begin{cases} tan^{-1}\left[\frac{Im(\rho_e)}{Re(\rho_e)}\right] & for\ Re(\rho_e) > 0 \\ tan^{-1}\left[\frac{Im(\rho_e)}{Re(\rho_e)}\right] + 180 & for\ Re(\rho_e) < 0, \quad Im(\rho_e) \geq 0 \\ tan^{-1}\left[\frac{Im(\rho_e)}{Re(\rho_e)}\right] - 180 & for\ Re(\rho_e) > 0, \quad Im(p\rho_e) < 0 \end{cases} \tag{2.28}$$

An appropriate physical model is necessary to accurately describe the optical properties of the material measured via ellipsometry. Values of the complex dielectric function of an unknown material can be found by a wavelength-by-wavelength regression analysis. Electronic band-to-band transitions cause critical point (CP) features in the dielectric function spectra. The imaginary part, $\varepsilon_2$, can be modeled conveniently using a Gaussian oscillator absorption model as in Equation (2.29) with best-match parameters of amplitude, $A$, center energy, $E_n$, and broadening, $B_r$. with $\sigma$ defined in Equation (2.30) [16].

$$\varepsilon_2(E) = A\left(\exp(-\left(\frac{E - E_n}{\sigma}\right)^2) - \exp(-\left(\frac{E + E_n}{\sigma}\right)^2)\right) \tag{2.29}$$

$$\sigma = \frac{B_r}{2\sqrt{\ln(2)}} \tag{2.30}$$

The real part, $\varepsilon_1$, is obtained from the Kramers-Kronig transformation shown in Equation (2.32), where $P$ is the principal value of the integral and $\omega$ is the angular frequency [16].

$$\varepsilon_1(E) = \frac{2}{\pi} P \int_0^\infty \frac{\xi \varepsilon_2(\xi)}{\xi^2 - E^2} d\xi \tag{2.31}$$

### *2.2.3 Differential Scanning Calorimetry*

Calorimetry, or the measurement of heat, allows for the study of physical transitions and chemical reactions that are linked with the generation or loss of heat. Differential scanning

calorimetry, DSC, measures the difference in the heat flow rate of a sample to a reference material while subjected to a controlled temperature program [17]. One such material property of interest in the present research is heat capacity.

A common DSC is shown in Figure 10. The reference material, $R_{ef}$, experiences the same sample heating conditions as the sample, denoted as *S* in the figure. The heat flow from the furnace passes through the disk with an integrated thermocouple. The thermocouples cover the entire base of both sample and reference pans. Heat flows from the disks to the sample and reference materials. The differential temperature signal, $\Delta T$, or the temperature differential between the heat flows is measured and then converted to the measured heat flow rate, $\phi_m$ by a factory-installed calibration [17].

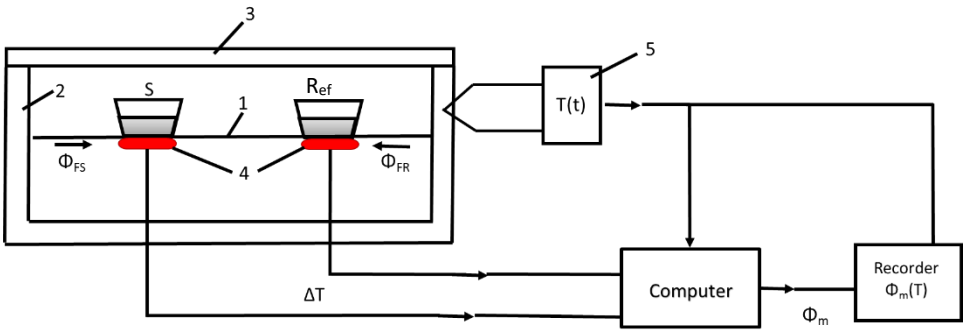


**Figure 10. Heat flux DSC with disk-type measuring system with 1) disk, 2) furnace, 3) lid, 4) differential thermocouples, 5) programmer and controller, S) sample crucible, and $R_{ef}$) reference crucible. The arrows at $\phi_{FS}$ and $\phi_{FR}$ indicate the locations where the heat flow rate from furnace to reference sample crucible and heat flow rate from the furnace to the reference sample are measured respectively. The recorder combines the $\phi_m$, measured heat flow rate and *k* calibration factor [17].**

The specific heat capacity, $c_p$, in steady state is the sample heat flow rate, $\frac{dQ_s}{dt}$, divided by the sample mass, *m*, and the heating rate, $\frac{dT}{dt}$. Therefore $c_p$ is equivalent to $\phi_s$, the sample heat flow rate divided by *m* and $\beta_0$, or the heating rate. Likewise $\phi_s$ is equivalent to $\phi_m$ minus the unavoidable asymmetry of the differential scanning calorimeter, $\phi_0$ [17].

$$c_p = \frac{C_p}{m} = \frac{\frac{dQ_s}{dt}}{m \cdot \frac{dT}{dt}} = \frac{\phi_s}{m \cdot \beta_o} = \frac{\phi_m - \phi_0}{m \cdot \beta_o} \tag{2.32}$$

A linear heat flow would produce a constant heating rate of $T(t) = T_0 + \beta_0 t$, where $\beta_0$ is the heating or cooling rate and $T_0$ is the starting temperature. A combination of linear and periodic heating provides the benefit of good temperature resolution for slow scanning speeds with the higher output signal due to faster oscillations.

A recent variation in the standard method, Modulated Differential Scanning Calorimetry, MDSC, combines the advantage of good temperature resolution at slow scan speeds with a higher output signal due to oscillations. MDSC uses a combination of linear and periodic heating and incorporates a variable heating rate. It therefore provides a time-dependent temperature $T(t)$ via Equation (2.33) [17]. In this system, every periodic temperature change is a sum of a sinusoidal function with a maximum heating rate of $(\beta_0 + T_A\omega)$ and a minimum heating rate of $(\beta_0 - T_A\omega)$. In the "heating only" mode $T_A\omega < \beta_0$.

$$T(t) = T_0 + \beta_0 t + T_A \sin(\omega t) \tag{2.33}$$

Hence $dT/dt$ is as shown in (2.34) where $\omega$ is the angular frequency of modulation and $T_A$ is the temperature fluctuation amplitude [25].

$$\frac{dT}{dt} = \beta_0 t + \omega T_A \cos(\omega t) \tag{2.34}$$

Through (2.34) only vibration heat capacity is considered, which has a very weak temperature dependence. Adding endothermic and exothermic latent heat exchange, the heat flow rate is defined by Equation (2.35), where $\Phi^{ex.}(T, t)$ represents the endothermic or exothermic latent heat exchange and $T_u$ represents the mean temperature around fluctuations, $T_u = T_0 + \beta_o t$ [17].

$$\Phi(T,t) = C_p\beta_o + \Phi^{ex.}(T,t) + C_p T_A \omega \cos(\omega t) + \frac{\delta\Phi^{ex.}(T_u,t)}{\delta T} T_A \sin(\omega t) \quad (2.35)$$

As the sample is heated during MDSC, the result represents a bulk measurement of the sample heat capacity. However, for the case of reactive materials such as $UO_2$, the measurement of the sample surface may be reduced due to heating, whereas a photoemission derived Debye temperature heat capacity measurement is made in a reduced oxygen environment, but only represents the surface.

### 2.3 Reference


[1] S. Hufner, *Photoelectron Spectroscopy Principles and Applications*, New York: Springer, 2003.

[2] C. L. Dugan, "Cathodoluminescence and Photoemission of Doped Lithium Tetraborate," M.S. Thesis, ENP, AFIT, Wright-Patterson AFB, OH, 2011.

[3] B. G. Yacobi, *Cathodoluminescence Microscopy of Inorganic Solids*, New York: Plenum Press, 1990.

[4] D. R. Vij, *Luminescence of Solids*, New York: Plenum Press, 1998.

[5] R. Eisbert and R. Resnick, *Quantum Physics of Atoms, Molecules, Solids, Nuclei, and Particles*, New York: John Wiley & Sons, 1985.

[6] D. R. Tallant, W. L. Warren and C. Seager, "Reflectivity Changes, and Accumulation of Graphitic Carbon during Electron Beam Aging of Phosphors," *Journal of Applied Physics*, vol. 82, p. 4515, 1997.

[7] Kotera, M., Murata, K., and Nagami, K., "Monte Carlo Simulation of 1 -10 keV Electron Scattering in a Gold Target," *Journal of Applied Physics*, vol. 52, p. 997 - 1003, 1982.

[8] Gauvin, R., Lifshin, E., Demers, H., Horny, P., and Campbell, H., "Win X-ray: A New Monte Carlo Program that Computes X-ray Spectra Obtained with a Scanning Electron Microscope," *Microscopy and Microanalysis*, vol. 12, p. 49-64, 2006.

[9] "NIST Physical Measurement Laboratory Engineering Physics Division," National Institute of Standards and Technology U.S. Department of Commerce, 15 April 2010. [Online]. Available: https://www.nist.gov/pml/engineering-physics-division/popular-links/hall-effect/hall-effect-figure-2. [Accessed 01 08 2018].

[10] D. K. Schroder, *Semiconductor Material and Device Characterization*, New York: John Wiley & Sons, 1998.

[11] D. A. Neamen, *Semiconductor Physics and Devices*, New York: McGraw Hill, 2003.

[12] P. Barnes, "Capacitance Voltage (C-V) Characterization of Semiconductors," *Characterization of Materials*, vol. 1, pp. 456-466, 2002.

[13] J. A. Woollam, "J.A. Woollam Co. Ellipsometry Solutions," 2016. [Online]. Available: https://www.jawoollam.com/resources/ellipsometry-tutorial/polarized-light. [Accessed 16 02 2017].

[14] J. A. Woollam, "A Short Course in Ellipsometry," [Online]. Available: https://www.nnf.ncsu.edu/sites/default/files/vase_manual_short_course.pdf. [Accessed 16 02 2017].

[15] H. Fujiwara, *Spectroscopic Ellipsometry: Principles and Applications*, Hoboken: John Wiley & Sons, 2007.

[16] A. Mock, R. Korlacki, C. Briley, D. Sekora, T. Hofmann, P. Wilson, A. Sinitskii, E. Schubert and M. Schubert, "Anisotropy, Band-to-Band Transitions, Phonon Models, and Oxidation Properties of Cobalt-Oxide Core-Shell Slanter Columnar Thin Films," *Applied Physics*, vol. 108-5, 2016.

[17] G. W. Hohne, W. F. Hemminger and H. J. Flammershiem, *Differential Scanning Calorimetry*, New York: Springer, 2003.

## III. Electrical Characterization of $UO_2$ – Improved Mobility in Single Crystal $UO_2$ Based Electronics.

This chapter is derived from a paper prepared for submission to the *Journal of Defense Research and Engineering*. Although the journal is an FOUO publication, this article was modified to meet the release statement of this dissertation. It was additionally modified to be consistent with the dissertation format. The collaborating authors are C. Dugan, R., Carmona, E. Cazalas, G. Peterson, J. M. Mann, and J. Petrosky. The journal article is titled, "Electrical Characterization of $UO_2$ – Improved Mobility in Single Crystal $UO_2$ Based Electronic Materials."

In order to determine if Hall effect measurements could be used to evaluate s.c. $UO_2$ mobility and carrier concentration without substantial surface preparation, Hall effect and I(V) measurements were conducted on two samples of s.c. $UO_2$ that had been exposed to different environments and experimental conditions. Previous research revealed large discrepancies in resistivity based upon probe type and placement. Consistent in each measurement was a current settling that occurred within 1-3 seconds of measurement that persisted for several minutes. We therefore compared Hall currents, which are primarily surface dominated, to I(V) through the bulk in order to determine if consistent measurements can be made using a dwell time of 5 seconds for each measurement.

### Abstract

This paper presents an initial study of electrical measurements of single crystals of $UO_2$ grown hydrothermally in a unique method at the Air Force Research Laboratory. Hall measurements reveal an electron mobility up to 2.5±1.3 $cm^2/V\text{-}s$. The measured conductivity of the samples was $(5.7\pm0.3)\times10^{-3}\ \Omega^{-1}\ cm^{-1}$. Direct current-voltage measurements were conducted

to assess the validity of the van der Pauw geometry Hall measurements, using the same contact probe materials. The I(V) relationship indicates that an ohmic contact is presented, and the semiconductor is not carrier limited during the measurement. The reported mobility and ability to construct a consistent contact are a promising new development demonstrating potential use of hydrothermally grown $UO_2$ as a semiconductor medium.

### 3.1 Research Innovation and Objective

Actinide oxides, and in particular $UO_2$, have been under study since before the nuclear age. A majority of the literature is oriented on developing and understanding nuclear fuels for either nuclear reactors or weapons. This study leverages a growth method for $UO_2$ with the potential to produce $UO_2$ material with consistent and quality electrical properties. We are studying this $UO_2$ to evaluate whether it may be exploited in uranium bearing electronics or have advantages in use with nuclear fuels.

### 3.2 Impacts on Warfighter Mission

The research is focused primarily on developing $UO_2$ neutron detectors, which can take advantage of the 180 MeV of energy from neutron induced fission products. Additional potential uses include a new class of radiation-hardened electronics and directly incorporating uranium electronic structures into nuclear fuels to assess aging, tampering and managing inventory; a significant part of the deterrence effort.

### 3.3 Introduction

Uranium dioxide is known to have unique semiconducting properties that have yet to be exploited [1]. From an electronic standpoint, $UO_2$ has poor characteristic properties, including low mobility and conductivity, and a very reactive surface that can allow multiple uranium-

dioxide phases to be present [2]. This inhibits production of quality and consistent direct measurements to assess electrical performance, restricting much of the potential applications research to modeling and simulations [2]. The present research, however, is a study of the electrical measurements of $UO_2$ crystals grown via a hydrothermal process, providing bulk samples of $UO_2$. These $UO_2$ samples provide an excellent opportunity to measure bulk carrier properties in order to assess engineering methods to produce a semiconductor device.

A key defense application for use of $UO_2$ is in the design and fabrication of a solid-state neutron detector. Such a detector could provide a substantial improvement in size and power over conventional solid-state neutron detectors, as well as replace $^3He$ gaseous detectors, which suffer from a shortage of $^3He$. In order to make a solid-state detector perform optimally, the majority carrier mobility ($\mu$) and the carrier lifetime ($\tau$) must be maximized. Assessing these parameters in $UO_2$ can be challenging due to the reactive nature of the surface in normal atmospheric conditions. It has been well established that $UO_2$ will undergo surface oxidation and that its electronic properties are very sensitive to the $UO_2$'s oxygen concentration [3-5]. Therefore candidate materials and analyses are often based upon ideal or theoretical parameters, skewing the evaluation of the material characteristics [4].

The $UO_2$ electronic band structure further complicates traditional methods of analysis as a semiconductor. $UO_2$ is a Mott insulator, with a 5 *f* orbital band lying between the conduction and valence bands [5]. Therefore, traditional band theory is not applicable in modeling potential device outputs before device construction and engineering is complete. This inhibits standard semiconductor development processes to optimize a structure before design begins. Therefore, it is imperative to conduct initial studies and rely on measured values to best assess the synthetic technique as well as the device design and fabrication. This paper illustrates initial Hall Effect

measurements that provide carrier conductivity (σ), and mobility (μ) measurements on a hydrothermally grown sample of $UO_2$, to be used for further engineering and material studies [6].

## 3.4 Method

### *3.4.1 Hydrothermal Growth*

Single crystals (s.c.) of $UO_2$ were grown by hydrothermal synthesis using a nutrient/feedstock of high-purity, depleted uranium dioxide powder (99.998% $UO_2$, International Bioanalytical Laboratories, Lot# B206093). A 6M cesium fluoride mineralizer solution (99.9% CsF, Alfa Aesar, Lot# S25A038) was utilized to aid dissolution of the nutrient and transport it to the colder crystallization zone of the reaction vessel. The temperature of the feedstock and crystallization zones were held at 650 and 600ºC, respectively for 45 days at a pressure of 25 kpsi. The feedstock, mineralizer and seed crystals were loaded into an inert sealed silver ampule (99.95% Ag, Refining Systems, Inc.) and then welded shut. Thorium dioxide, $ThO_2$, seeds provided templated nucleation and crystalline $UO_2$ growth > 0.10 mm thick [7].

Following growth, samples were cleaned by sonication in deionized water, polished, sawed into roughly 1.3-1.5 mm thick wafers (to separate the $UO_2$ from the $ThO_2$ seed crystal), hand polished and cleaned again. Our sample set consisted of two $UO_2$ samples from the same growth method, but with surfaces that had been exposed to multiple different ambient and test environmental conditions.

### *3.4.2 Hall Measurements*

All Hall effect measurements were accomplished using a 4 point probe in a standard van der Pauw configuration with tungsten tips [8]. Measurements were carried out at a constant

current of 200 μA and a constant magnetic field of 7 kG. The probe tips were mechanically contacted directly to the $UO_2$ and held in place using a spring, similar to that used by Hartmann [3]. Unlike Hartman, we did no surface preparation (e.g. reduction) before measurement. Based upon our previous experiences with this material, we isolated the substrate from the sample station using a thin Mylar film and used a 5-second dwell time for each Hall effect measurement to allow for current settling. The source of this settling is presently unknown, but is under separate investigation.

### *3.4.3 Current-Voltage, I(V), Measurements*

The primary purpose for the direct current (d.c.) I(*V*) measurement was to ensure Hall currents were not invalid due to incorrect or improper metal to semiconductor electrical contact material selection or application. This has been reported as problematic with $UO_2$ electrical measurements [2-3].

If the tungsten contacts impede the current, then Hall current measurements would be invalid at the voltage used for the measurement. If instead, an ohmic or tunneling junction (spatially thin Schottky junction) was present, then the contact would appear ohmic, and the Hall data would be valid.

## 3.5 Results

### *3.5.1 Hall Measurement Results*

Table 2 provides the results of the Hall Effect measurements as compared to those reported in the literature. [4, 9] In our data, mobilities are consistently higher than most literature values. Resistivity values for Sample 1 are close to the high end of published values while Sample 2 provides an average resistivity consistently higher than literature results.

**Table 2. Hall Effect data from literature values compared.**

| | | s.c. $UO_2$ | |
|---|---|---|---|
| | Published[4,9] | Sample-1 | Sample-2[2] |
| $\boldsymbol{\mu}\left[\frac{cm^2}{V\,s}\right]$ | 0.015 to 1 | 1.57±0.62 | 3.20±1.54 |
| $\boldsymbol{\sigma}\left[\frac{1}{\Omega\,cm}\right]$ | $6\times10^{-7}\ to\ 3\times10^{-3}$ | $(1.43\pm0.21)\times10^{-3}$ | $(5.66\pm0.34)\times10^{-3}$ |

**[1]Two measurements were taken on Sample-1.**

**[2]The values provided for Sample-2 are an average of six measurements.**

### *3.5.2 Direct Current, Current Voltage Measurement Results*

For each d.c. I(*V*) measurement, the voltage was swept from -5 to +5 V and back. Although multiple sweeps were made, the error was less than 1%.

Figure 11 provides the Hall Effect I(V) results and the d.c. I(V) measurements. An important delineation of these measurements is that the Hall effects measurements are performed using four contacts applied to the same sample surface, while the d.c. I(V) uses two contacts on opposing surfaces, each normal to the bulk of the sample (Figure 12). Both measurements have a linear I(V) relationship with the same slope at low current providing evidence that the contacts

appear ohmic with the same material resistance. Additionally, there is no discernable difference in the conductivity of the Hall measurement when compared to the d.c. I(V) measurements.

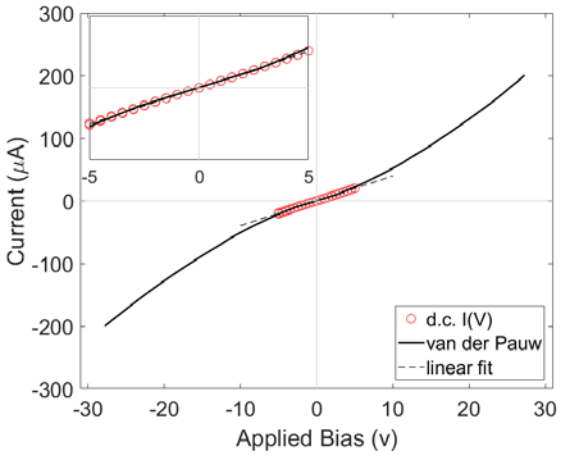


**Figure 11. Current vs. voltage measurements from d.c. I(V) compared to the van der Pauw Hall measurements. Inset shows the ohmic nature (linearity) of the contacts for both measurements.**

### 3.6 Discussion

A full interpretation of these results must include a detailed study of the surface structure, which was beyond the scope of this publication. However, the consistency of the measurements, lack of a barrier to conduction (either due to the tungsten-sample contact being truly ohmic or because it is a tunneling contact) and good comparison of conductivity in two measurement methods is encouraging in the light of lack of sample preparation to obtain such results.

Sample preparation and contact material considerably impact $UO_2$'s electrical measurements. For example a 10-fold increase over our conductivity results was reported by Hartmann under vastly different conditions [3]. The samples in the Hartmann study were with sintered $UO_2$ fuel pellets, both with or without a tragacanth binder. The contacts were made using copper disks and silver-plated Hall electrodes. Lastly, surfaces were reduced using flowing hydrogen, while gradually heated over two hours to 1900 °C, heated for 20 minutes and

quenched to room temperature in 15 minutes to provide a clean surface [3]. In the present study the $UO_2$ samples had rough polished surfaces that were cleaned using acetone before contacts

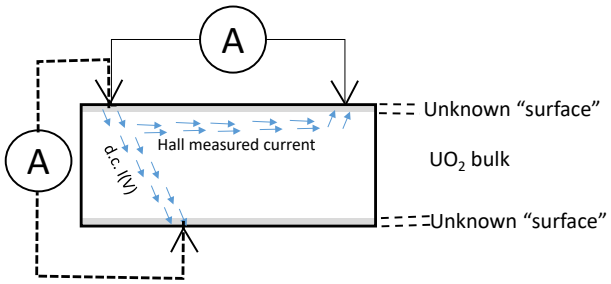


were made. Consequently, a promise of higher conductivities and mobility appears plausible with substantial sample preparation, even with lesser quality $UO_2$ samples.

**Figure 12. Schematic of van der Pauw Hall configuration and that of the d.c. I(V) measurement (dashed lines). Both show current must pass through the unknown surface layer twice.**

Also in our measurements we demonstrate a consistently between two contact methods with little sample preparation. One possible explanation for our results is the sample is entirely stoichiometric $UO_{2.0}$, and the surface nature of the Hall effect measurements and bulk nature of the I(V) measurements are sampling the same material. Thus, the Hall effect measurement would characterize $UO_2$ directly. However, based upon well-documented surface studies of $UO_2$ it is reasonable to assume that all surfaces of our sample have oxidized and that there are differences in bulk and surface character. If this is the case, then two additional potential options exist, either the current is wrapping around the crystal edge or both measurement techniques are reaching the crystal bulk. The edge and the surface of s.c. $UO_2$ represent different crystal surfaces. A (100) $UO_2$ vicinal surface has a reduced tendency for step ordering compared to (111) $UO_2$ vicinal surface creating dissimilar surface diffusion barriers [10]. Since different diffusion barriers are specific to crystal orientation, one would not expect to find consistent conductivities between both measurement techniques. Therefore, the d.c. I(V) measurements are not likely a result from

surface wrapping current. The most plausible explanation is that both experimental techniques are reaching bulk $UO_2$ with the Hall effect current penetrating a thin oxidized resistive surface layer (designated as "unknown in our diagrams) and reaching the bulk. The d.c. I(V) measurements are taken normal to the surface, conducting through the bulk of the material. Since both conductivity results are consistent, we can eliminate the possibility of surface effects dominating the Hall current, the primary interest in our study.

### 3.7 Conclusion

This report provides an initial measurement of the mobility for hydrothermally grown s.c. $UO_2$ which represents a high mobility with little surface preparation. The consistency of the bulk d.c. I(V) measurements reported here provide evidence that Hall currents are representing the material as the I(V). The high mobility is favorable for $UO_2$ being selected as a working semiconductor for a solid-state neutron detection device. As with many non-traditional materials, we also have demonstrated some of the behaviors that must be considered when working with $UO_2$, not observed with more traditional materials.

Present and future endeavors in this work include further development of contact placement, evaluation of surface structure with depth, and a better understanding of the electronic band structure, especially when a contact is present.

### 3.8 References

[1] Meek, T., Hu, M., and Haire, M. "Semiconductive Properties of Uranium Oxides," Waste Management 2001 Symposium, 2001.

[2] Roy, L. E., Durakiewicz, T., Martin, R. L., Peralta, J. E., Scuseria, G. E., Olson, C. G., Joyce, J. J., and Guziewicz, E., "Dispersion in the Mott Insulator $UO_2$: A Comparison of Photoemission Spectroscopy and Screened Hybrid Density Functional Theory," *Journal of Computational Chemistry*, vol. 29-13, pp. 2288–2294, 2008.

[3] Hartman, A., Werner, “Elektrische Untersuchungen A Oxydischen Halbleitern,” *Zeitschrift fur Physik*, pp.709-733, 1936.

[4] Schoenes, J. “Optical Properties and Electronic Structure of $UO_2$,”*Journal of Applied Physics*, vol. 49-3, pp. 1463–1465, 1978.

[5] Teterin, Y. A., Kulakov, V. M., Baev, A. S., Nevzorov, N.B., Melinkov I.V., Streltsov, V.A., Mashirov, L.G., Suglobov, D.N., and Zelenkov, A.G., “A Study of Synthetic and Natural Uranium Oxides by X-ray Photoelectron Spectroscopy.” *Physics and Chemistry of Minerals*, vol. 7-4, pp. 151-158, 1981.

[6] Ferris, K. and Jones, D., “Trade-Offs and Compromises in Carrier Properties of Semiconducting Materials,” *IEEE Transactions on Nuclear Science*, vol. 60, no. 2, pp. 1237-1242, April 2013.

[7] Dugan, C., Peterson, G., Mock, M., Young, C., Mann, J.M., Nastasi, M., Schubert, M., Wang, L., Mei, W., Tanabe, I., Dowben, P., Petrosky, J. “Electrical and Material Properties of Hydrothermally Grown Single Crystal (111) $UO_2$,” *The European Physical Journal B*, vol. 92:67, April 2018.

[8] van der Pauw, L. J. "A Method of Measuring Specific Resistivity and Hall Effect of Discs of Arbitrary Shapes," *Philips Research Reports*, vol. 13, pp. 1-9, 1958.

[9] Magill, J., Hyland, G., and Rand, M. “New Ionic Contributions to the Vapor Pressure of Urania,” *The Journal of Chemical Physics* vol. 88, pp. 4101-2, 1998.

[10] Taylor, P. and Ellis, W., “A LEED Study of $UO_2$ (100) Vicinal Surfaces,” *Surface Science*, vol. 77-2, pp.321-336, 1978.

## IV. Electrical and Material Properties of Hydrothermally Grown Single Crystal (111) $UO_2$

The contents of this chapter were published in the *European Journal of Physics B*, volume 91, pages 1-7, in April 2018. The journal citation is: C. Dugan, G. Peterson, A. Mock, J. M. Mann, M. Natasi, M. Schubert, L. Want, L. Mei, I. Tanabe, P. Dowben, and J. Petrosky, "Electrical and Material Properties of Hydrothermally Grown Single Crystal (111) $UO_2$." It was modified to be consistent with the dissertation format.

As part of the evolution of material growth studies, a $UO_2$ hydrothermal growth was accomplished using a $CaF_2$ seed crystal to identify the quality of the $UO_2$ growth. The majority carrier, carrier lifetimes and barrier type were measured, while evaluating crystal quality. Electrical properties were determined with I(V), and C(V), measurements, while band-gap confirmation and crystal quality were assessed by ellipsometry and compared with density functional theory (DFT) modeling. This paper is inconclusive of the s.c. $UO_2$ majority carrier type, while the crystal quality corroborates the need for further s.c. $UO_2$ material characterization.

### Abstract

The semiconductor and optical properties of $UO_2$ are investigated. The very long drift carrier lifetimes, obtained from current-voltage, I(V) and capacitance-voltage C(V) measurements, along with the well-defined optical properties provide little evidence of an abundance of material defects away from the surface region. Schottky barrier formation may be present, but very much dependent on the choice of contact and surface stoichiometry and we find that Ohmic contacts are in fact favored. Depth resolved photoemission provided evidence of a chemical shift at the surface. Density functional theory, with the Heyd-Scuseria-Ernzerhof (HSE) functional, indicates a band gap of 2.19 eV and an anti-ferromagnetic ground state.

Ellipsometry measurements indicate that $UO_2$ is relatively isotropic with a band gap of approximately 2.0 eV, consistent with theoretical expectations.

### 4.1 Introduction

The rapid depletion of $^3He$ resources, and the desire for vibration insensitive, radiation hard devices dominates the search for alternative neutron detector technologies [1] used for tracking fissile materials. The ultimate goal is an efficient, compact, low power detector relatively unaffected by terrestrial temperature changes. As an example, icosahedral semiconducting boron carbides [2-6] have recently garnered interest because they meet many of the operational requirements, but they still need significant neutron moderation to be efficient in detecting neutrons from fissile materials.

A novel approach explored in this research is a solid-state neutron detector composed of $UO_2$. Uranium has the unique (among semiconductors) feature of a high fission cross section, making it a valuable medium for detection because of the potential for very large signal-to-noise generation. It has been studied as a neutron absorber since the 1930s [12]. In recent years, although somewhat limited, there have been efforts to explore the geometric and electronic properties of $UO_2$ for the purpose of semiconductor device fabrication [8, 9, and10]. Primarily focused on the prospects of neutron detection and photovoltaics, the concept has been largely undeveloped due to the difficulty of material growth. [8,10] Single crystal growth of actinides for application in electronics is complex due to the very large electron-phonon coupling, lattice deformations, and significant changes in Debye temperature, mediated through Jahn-Teller distortions [26]. These latter effects are unusual, as $UO_2$ is a true semiconductor, not a metal, so phonons cannot couple to the Fermi Sea of electrons or holes.

Given the orthorhombic allotrope of α-phase uranium metal, the fluorite structure of $UO_2$, rapid oxidation, and large range of O/U ratios, it is difficult to control sample stoichiometry without strictly controlling temperature and pressure of the growth environment [17]. A further complication exists: while defect creation is expected to occur at high(er) temperatures, especially above 1000 K, the simplified phase diagram of the $UO_x$ system suggests a $UO_{2+x}$ to a combination $UO_{2+x}$ and $U_4O_{9-y}$ transition between 473 to 670 K [13, 14]. Such a structural phase transition would alter the density of lattice imperfections and a change in defect density would enhance Jahn-Teller distortions significantly [11, 15].

The challenges of growing high-quality uranium oxide single-crystal have begun to be addressed with the fabrication of high-quality, single crystal actinide oxide samples using a hydrothermal synthesis growth technique [20]. This growth process has produced bulk single crystals of near-stoichiometric $UO_2$. These improved single crystals open the door to a much better assessment of the optical and semiconductor properties, not previously possible.

**4.2 Experimental**

Single crystals of $UO_2$ were grown by hydrothermal synthesis using a nutrient/feedstock of high-purity, depleted uranium dioxide powder (99.998% $UO_2$, International Bioanalytical Laboratories, Lot# B206093). A 6M cesium fluoride mineralizer solution (99.9% CsF, Alfa Aesar, Lot# S25A038) was utilized to aid dissolution of the nutrient and transport it to the colder crystallization zone of the reaction vessel. The temperature of the feedstock and crystallization zones were held at 650 ºC and 600 ºC, respectively for 45 days at a pressure of 25 kpsi. The feedstock, mineralizer and seed crystals were loaded into an inert sealed silver ampule (99.95% Ag, Refining Systems, Inc.) and then welded shut. $CaF_2$ seeds with (111) orientation provided a template for oriented growth of 0.10 mm $UO_2$ on the substrate. Orientation and crystal structure

was confirmed by single-crystal X-ray diffraction. $UO_2$ crystals grown under these conditions have measured lattice parameters of 5.4703 ± 0.0006 Å indicating a stoichiometry near $UO_{2.003}$ [13, 17]. The resultant (111) $UO_2$ crystal's triangular surface area measured approximately 21 $mm^2$.

Contacts on a triangular 21 $mm^2$ (111) $UO_2$ sample were fabricated at 20º C using a paint/melt deposition technique as well as mechanical placement. The circular Ag paint contact with radius of approximately 2.9 mm, was fabricated by application of Ag (Delco Conductive Ag Paint, #16062). The opposing circular GaIn paint/melt contact with radius of approximately 4.5 mm was fabricated by applying a GaIn eutectic (Aldrich Gallium-Indium eutectic, > 99.99% trace metals) to the $UO_2$ (111) sample. Mechanical contacts were made by pressing sharpened tungsten pins into opposing facets of the crystal. Micron thick Cu wires were then affixed to the contacts allowing current-voltage, I(V), and capacitance-voltage, C(V), measurements using a semiconductor analyzer system. The paint/melt two-point circuit used the Ag contact as the positive voltage reference. The work function of polycrystalline Ag is 4.26 eV, slightly higher than that of GaIn, 4.1 – 4.2 eV making possible ohmic contact surfaces [27] [28].

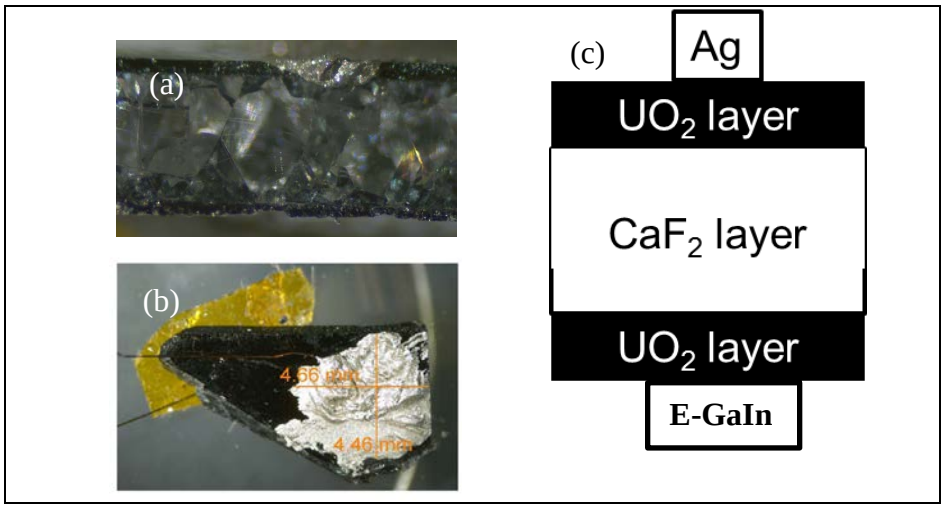


**Figure 13. $UO_2$ with $CaF_2$ seed crystal. Figure 13 (a) is a side-view of the $UO_2$ on the crystalline $CaF_2$ seed. Figure 13(b) provides a top view with a 4.5 mm diameter E-GaIn contact. In Figure 13(c) a diagram of the crude Ag/$UO_2$/$CaF_2$/$UO_2$/E-GaIn device.**

Variable angle spectroscopic ellipsometry (VASE) data was obtained using a dual-rotating compensator ellipsometer (RC2, J.A. Woollam Co., Inc.), using a wavelength-by-wavelength approach. The 0.1 mm $UO_2$ layer atop the 1-mm $CaF_2$ substrate was assumed to be bulk and therefore, the $CaF_2$ layer was neglected. This method allowed for the determination of the dielectric response of the bulk top layer $UO_2$. Measurements were taken at angles of incidence 45°, 55°, 65°, and 75° from 0.7 to 6.4 eV. The sample was modeled using a simple two-phase (ambient-substrate) approach where the substrate represents single-crystal $UO_2$, ignoring surface overlayer effects. Data was analyzed using WVASE32 (J.A. Woollam Co., Inc.).

### 4.3 Theory

All density functional theory calculations were performed within the framework of spin-polarized plane-wave density functional theory (PW-DFT), as implemented in the Vienna *ab initio* simulation package (VASP) [20]. The generalized gradient approximation (GGA) with the Perdew-Burke-Ernzerhof (PBE) functional and projector augmented wave (PAW) potentials

were used for geometry optimizations [21 -24] and specifically the exchange correlation was treated with the Perdew-Burke-Ernzerhof (PBE) functional [23]. In addition, to correcting the strong on-site electronic correlation, the DFT+U method was used for the U atoms with U - J = 4 eV. We used the simplified approach to the DFT+U introduced by Dudarev et al., where only the difference (U - J) is used to describe the electron correlation from different orbital momentum, U and J are the spherically averaged matrix elements of the screened Coulomb interaction[25].

We constructed the slab model for the $UO_2$ (111) surface with seven U atomic layers and eight O atomic layers, as shown in Figure 14. A vacuum layer, thicker than 15 Å between two adjacent slabs, was inserted in order to make the interactions between the slabs negligible. Geometrical structures were relaxed until the force on each atom was less than 0.01 eV/Å and the energy convergence criteria of $< 10^{-7}$ eV was met. The 2D Brillouin zone integration using the Monkhorst-PackΓ-center scheme was sampled with a 9 × 9 × 1 grid [28]. The Bader's atom in molecule (AIM) method based on the calculated charge density used for charge population analysis [26].

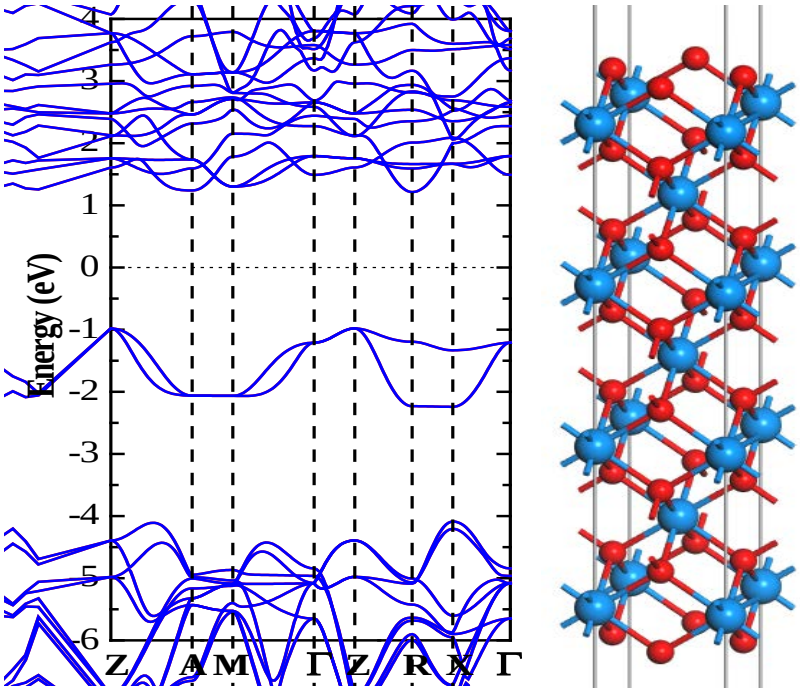


**Figure 14. The band structure of bulk $UO_2$ (schematically shown with O: red; U: blue) using Heyd-Scuseria-Ernzerhof (HSE) hybrid functional. The band gap is 2.19 eV and the ground state is anti-ferromagnetic.**

The Heyd-Scuseria-Ernzerhof (HSE) hybrid functional was also used to confirm the PBE+*U* results and we noticed that the new approach was more efficient in reaching convergence [27]. To complement density functional theory computation, the Cambridge Serial Total Energy Package (CASTEP) code was also adopted [28].

### 4.4 Results & Discussion

The I(V) measurement was used to evaluate the electrical contacts of the metal-semiconductor interfaces [27]. Knowing the work function of the metals ($\varphi_M$) and the electron affinity ($\chi$) allows for the prediction of the barrier height ($\varphi_B$) if a Schottky (metal-semiconductor) diode has been formed from Equation (4.1) and Equation (4.2), where $E_g$ is the semiconductor band gap [29].

$$\varphi_B = \varphi_M - \chi \text{ if the semiconductor is n-type} \quad (4.1)$$

$$\varphi_B = E_g + \chi - \varphi_M \text{ if the semiconductor is p-type} \quad (4.2)$$

The fluid metal eutectic, Ga-In or "EGaIn" forms an ohmic contact with thin-films devices due to its tendency to make low contact-resistance structures and has been chosen as the anode contact material [28]. The polycrystalline colloidal silver paste contact was deposited by vacuum evaporation.

The band gap, $E_g$, for $UO_2$ has been established as 2.1±0.1 eV [30]. In the flat band approximation, $\chi$ is the determined by subtracting band gap $E_g$ from the photoemission work function. The photoelectric work function of the (111) hydrothermally grown $UO_2$ was measured at 6.28 ± 0.36 eV providing an electron affinity of 4.2 eV [11]. Making use of Equations (4.1) and (4.2) for the (111) $UO_2$, if the semiconductor is n-type, $q\phi_{Bn0} = 0.56$ eV. If the semiconductor is p-type, the barrier, $q\phi_{Bp0}$, is 1.5 eV.

The band gap is vastly underestimated in density functional theory, under the Perdew-Burke-Ernzerhof (PBE) functional, even with a correlation energy 'turned on', i.e. $E_g$=0.28 eV. For CASTEP with PBE+U with a correlation energy of U=4 eV applied to the f-states and the ultrasoft pseudopotential, the band gap is only slightly better ~ 0.56 eV, based on different convergence schemes. However, with the Heyd-Scuseria-Ernzerhof (HSE) hybrid functional, the band gap comes out more correctly; but it is nonetheless clear that the 5f levels are very much a part of the band structure.

For VASP with PBE+U and plane augmented wave (PAW) pseudopotential: the $UO_2$ ground state is anti-ferromagnetic as is also indicated by VASP calculations undertaken with the HSE hybrid functional. For CASTEP with PBE+U and the ultrasoft pseudopotential, $UO_2$ is

ferromagnetic while it is ferrimagnetic in the slab calculation using the HSE hybrid functional. The convergence process of VASP was quite smooth.

The near linear I(V) response of Figure 15 clearly shows behavior near ohmic (i.e., a very small barrier to charge carriers). The energy of the Schottky diode is reduced by holes flowing from the metal to the semiconductor hence causing accumulation near the junction. Such a device is dominated by the electron flow from the semiconductor to the metal with essentially no recombination in the depletion region. Since the behavior is ohmic, there are two options for majority carriers at the junction. A p-type semiconductor metal interface can respond ohmically, since the work function of $UO_2$ is close to or larger than the sum of the electron affinity and the band gap energy. However, if the semiconductor is strongly n-type, then current flow could appear ohmic due to tunneling. Therefore, the I(V) plot is inconclusive as to majority carrier.

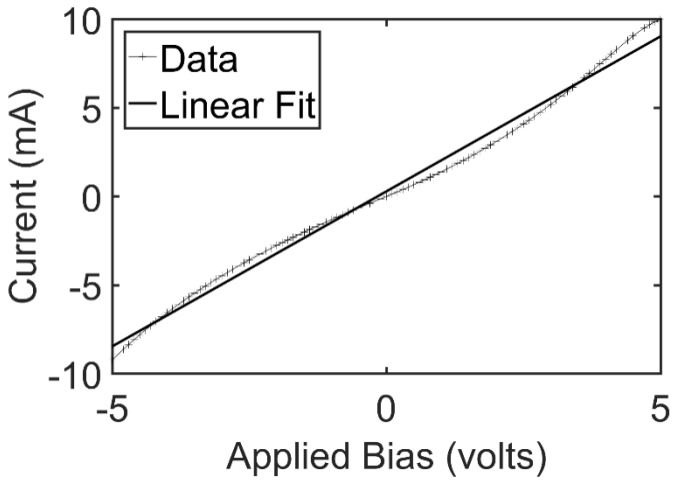


**Figure 15. The current versus voltage measurements of Ag/$UO_2$/E-GaIn metal-semiconductor Schottky device. The nearly linear data indicates a minimal barrier to charge carriers but is inconclusive as to the semiconductor majority carrier.**

Although the reverse bias behavior of a Schottky diode mimics that of a p-n junction (allowing for the $1/C^2$ determination of $V_{bi}$ by linear extrapolation), the forward bias a.c. response is fundamentally different, since it is a majority carrier device. There is negligible

diffusion current, and therefore negligible minority carrier charge injection and storage within the semiconductor. Instead stored carriers result in diffusion admittance. In the absence of stored carriers, there is no diffusion capacitance or diffusion conductance. As a result, at frequencies routinely approaching the GHz range, the device capacitance and conductance remain frequency independent. However, this is not what is observed in the data of Figure 16. The measurement of capacitance versus frequency (C(ω)), and conductance versus frequency (G(ω)) clearly show a frequency dependent response, with charge carriers that no longer respond at 10 kHz. This departure from the ideal is an indication of defects within the semiconductor.

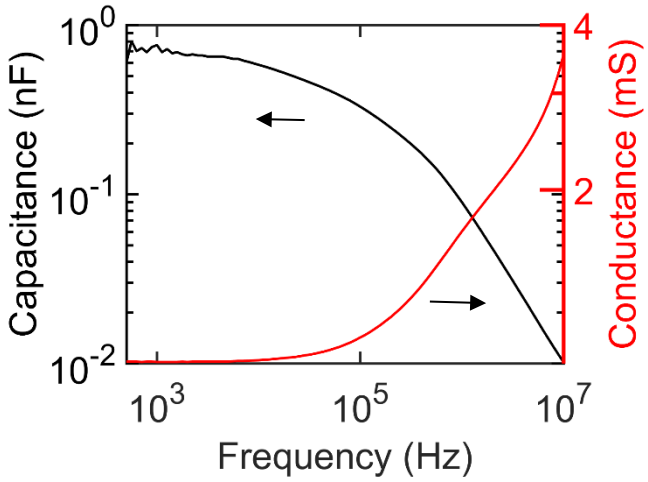


**Figure 16. The capacitance versus frequency and conductance versus frequency (semi-Log scale) measurements of Ag/$UO_2$/E-GaIn MS Schottky device. The frequency dependence of the data beginning at 10 kHz shows the presence of defects within the device.**

Figure 17 shows the capacitance versus voltage curves for different perturbation frequencies. Again, the frequency dependence in reverse bias is evident as the capacitance is reduced with increasing perturbation frequency. A $1/C^2$ extrapolation has been performed to determine $\varphi_B$, and is shown as an inset in Figure 17. The effective barrier height was found to be $\varphi_B$=1.28 eV. Although not completely equivalent, this barrier height coincides closer with the I(V) barrier height for p-type $UO_2$ from our previous calculations.

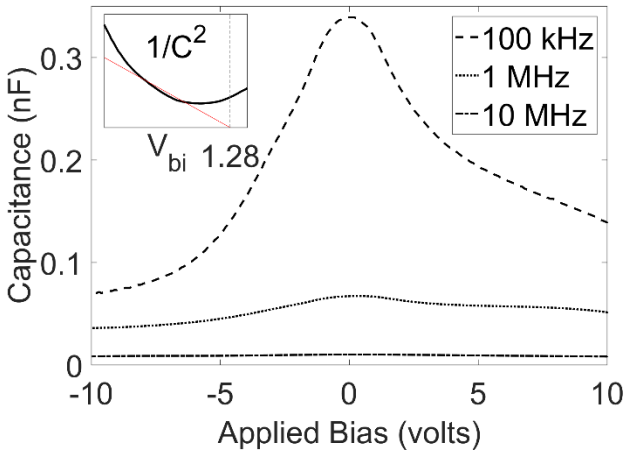


**Figure 17. The capacitance versus voltage measurement for the perturbation frequencies 100 kHz, 1 MHz, and 10 MHz. The inset is a $1/C^2$ extrapolation for the determination of the effective barrier height $\varphi_B$=1.28eV.**

While Figure 15 indicates the presence of defects, it is unclear as to their location (bulk or interface). However, the frequency at which the capacitance begins to increase provides evidence of defect type. For example, it has been shown in Si p-n homojunctions that defects due to vacancies and interstitial oxygen complexes cannot respond to oscillations near the $10^4$ Hz range [30], whereas other defects do. The C(V) curves, at 100 kHz and 1 MHz frequencies of the $UO_2$ Schottky diode are plotted in Figure 18. Ignoring defects and various contributions to capacitance, the drift carrier lifetime can be modeled by comparing the measured C(V) curve and the modeled diffusion capacitance in the region of small forward bias. The frequency dependent diffusion capacitance, $C_D$, is given by

$$C_D = \frac{G_0}{\omega\sqrt{2}}(\sqrt{1+\omega^2\tau^2}-1)^{1/2}, \tag{4.3}$$

where $\omega$ is the angular frequency ($2\pi f$), and $\tau$ is the drift carrier or effective carrier lifetime. The low frequency conductance, $G_0$, is calculated from the dc I(V) values by numerical differentiation. Utilizing $G_0$ and f from the experiment, $\tau$ can be iteratively adjusted to ensure the $C_D$ curve fits the C(V) data. The lifetime, $\tau$, controls the height and the slope of the modeled $C_D$

to the measured C(V) data and yields a drift carrier lifetime. Using this method, the Ag/$UO_2$ Schottky diode at 100 kHz is found to have a drift carrier lifetime ranging from 50 to 250 $\mu$s suggesting while defects are present, they are either not trap or scattering defects, or relatively few in number.

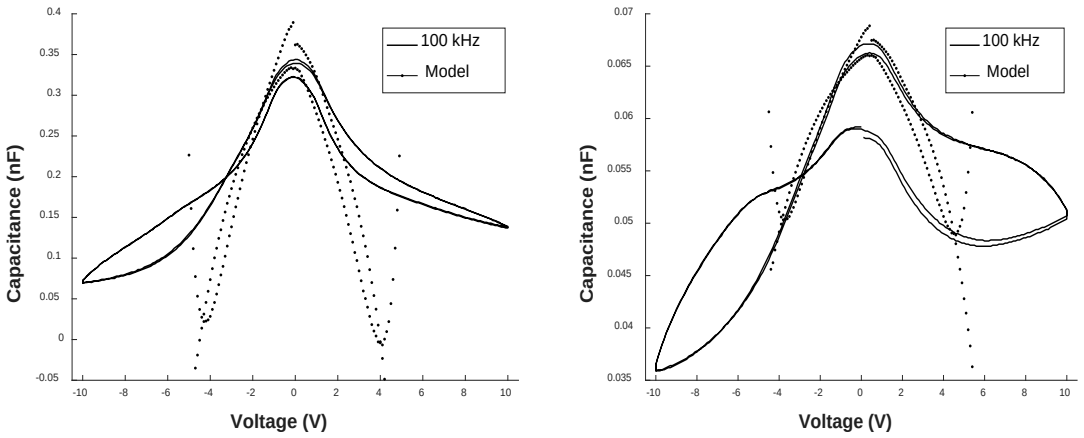


**Figure 18. Modeled diffusion capacitance $C_D$ (·) overlaid on C(V) data measured (solid lines) at 100 kHz and 1 MHz for the Ag/$UO_2$Schottky diode. The calculated diffusion capacitance, $C_D$, indicates a drift carrier lifetime in (a) of approximately 50 $\mu$s and in (b) of approximately 250 $\mu$s.**

To ascertain whether the surface defects differ from the bulk, depth resolved XPS measurements of the U 4*f* region of the (111) $UO_2$ sample surface were taken using Al Kα radiation prior to contact placement. The XPS showed indications of higher surface oxidation states of uranium. The binding energy of both doublet peaks increase from the expected energies of $U^{4+}$ at 0°, the condition in which the electron analyzer is normal to the sample surface, to higher binding energies at steep angles, indicating a chemical shift at the surface. The maximum sampled depth is estimated to be 50 Å at 0° based on the attenuation of an 1100 eV photoelectron [26]. Surface sensitivity is enhanced by altering the orientation angle of the electron analyzer away from 0°, normal to the surface, with an information depth of approximately 40 Å.

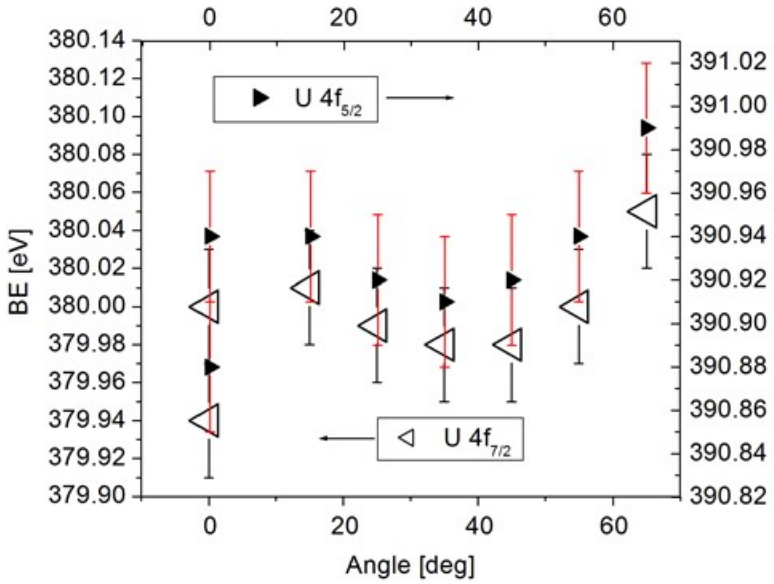


**Figure 19. The depth resolved XPS on the $UO_2$ (111). Both U 4*f* peaks shift to higher binding energies at the surface of the crystal, with increasing take off angle, indicating a chemical shift of the U to an oxidation state greater than $U^{4+}$.**

We estimate the depth of the p-type surface layer to be less than 40 Å based on the depth-resolved XPS measurement. Willis [31] showed that a hyper-stoichiometric (effectively p-type) $UO_{2+x}$ in the cubic fluorite structure is possible by the incorporation of interstitial oxygen. Willis concluded that the defect complex is comprised of 2 anion vacancies, 2 <111> interstitial oxygen atoms, and 2 <110> interstitial oxygen atoms. The C(ω), G(ω), and x-ray photoemission data all support the presence of a hyper-stoichiometric layer at the surface of the $UO_2$ crystal. Analysis shows that this layer is approximately 40 Å deep. Due to the presence of defects at the surface, and the low number of charge carriers of the bulk semiconductor material, near the surface, the material is effectively p-type creating a metal-semiconductor Schottky barrier with the Ag metal contact. The extremely narrow range of this region explains the discrepancy between the predicted barrier height of this contact of 1.5 eV and the effective barrier of 1.28 eV from the C(V) data. Fowler-Nordheim tunneling is known to dominate in devices as wide as 1200 Å [32],

although our data presently cannot support this. Overall, it seems that the material, unusual for an oxide, is p-type [33].

Variable angle spectroscopic ellipsometry (VASE) measurements, made at several azimuthal orientations, tends to verify that the sample is isotropic. This is important as some have concluded there is uniaxial anisotropy [34]. There was no significant evidence of anisotropy in the variable angle spectroscopic ellipsometry (VASE) data. Spectroscopic ellipsometry is an indirect measurement technique, which utilizes changes in polarization of light reflected off or transmitted through a sample [37-38]. An appropriate physical model is necessary to accurately describe the optical properties of the material. Values of the complex dielectric function of an unknown material can be found by a wavelength-by-wavelength regression analysis. Electronic band-to-band transitions cause critical point (CP) features in the dielectric function spectra. The imaginary part, $\varepsilon_2$, can be modeled conveniently using Gaussian functions as:

$$\varepsilon_2(E) = A\left(\exp\left(-\left(\frac{E-E_n}{\sigma}\right)^2\right) - \exp\left(-\left(\frac{E+E_n}{\sigma}\right)^2\right)\right), \tag{4.4}$$

$$\sigma = \frac{B_r}{2\sqrt{\ln(2)}}, \tag{4.5}$$

with best-match parameters of amplitude, A, center energy, $E_n$, and broadening, $B_r$ [35]. The real part, $\varepsilon_1$, is obtained from Kramers-Kronig transformation such that

$$\varepsilon_1(E) = \frac{2}{\pi} P \int_0^\infty \frac{\xi\varepsilon_2(\xi)}{\xi^2 - E^2} d\xi, \tag{4.6}$$

where P is the principal value of the integral and ω is the angular frequency. The dielectric constants determined in this study agree very well with those presented by Siekhaus and Crowhurst [38]. However, as Siekhaus and Crowhurst discuss, there is a significant shift when compared to reflectivity measurements as determined by Schoenes [39].

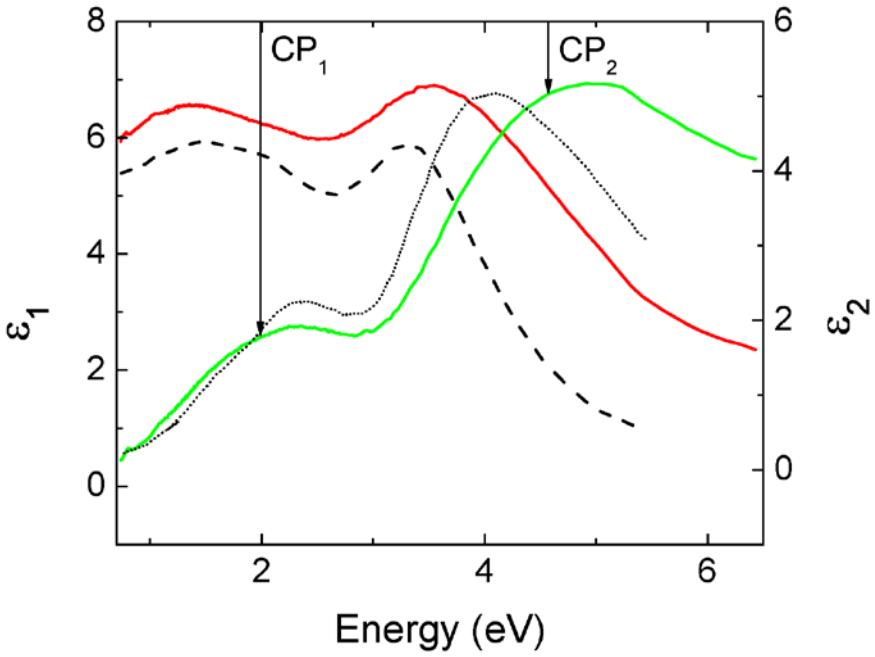


**Figure 20. Dielectric function of single-crystal $UO_2$ obtained in this analysis (red and green solid lines, respectively) compared to those by Siekhaus et al. [36](black dash and dot, respectively). Both the results of Siekhaus et al. [38] and this work come from ellipsometric techniques (see text). Arrows indicating the critical points identified by our work are labeled and correspond to Gaussian oscillator parameters.**

While we observe a similar shape to the real and imaginary parts of the dielectric response, we find a significant shift in the critical points (CPs). Electron band-to-band transitions create CP features in a dielectric response spectra [35]. These critical points are described using Gaussian oscillators and are summarized in Table 3. A single Gaussian oscillator centered beyond the investigated spectral region at 8.02 eV was also used to account for high-energy contributions. A constant offset and infrared contribution were accounted for in the analysis, which are not further detailed in the table.

**Table 3. Critical point transition parameters of single-crystal $UO_2$, obtained from spectroscopic ellipsometry data analysis of single-crystal $UO_2$. Parentheses denote 90% confidence of the last digit.**

| | Critical Point Transitions | | |
|---|---|---|---|
| Feature | A (eV) | E (eV) | $B_r$ (eV) |
| $CP_1$ | 1.5(1) | 1.99(1) | 1.5(1) |
| $CP_2$ | 3.7(5) | 4.57(1) | 2.4(1) |
| $CP_3$ | 4.6(1) | 8.02(9)[1] | 5.3(9) |
| [2]$CP_1$ | 1.8(6) | 2.1(1) | 1.5(2) |
| [2]$CP_2$ | 3(2) | 3.9(1) | 1.4(2) |
| [2]$CP_3$ | 3.3(4) | 5.1(5) | 3(1) |

**[1]Transition outside of presented range with limited sensitivity to critical point parameters.**

**[2]Features approximated by applying oscillators as used in this work to data gathered by Siekhaus et al. [36].**

The energetically lowest critical point was determined to have an energy of 1.99 eV, based on the spectral center of the absorption feature, compared to 2.4467 eV, as determined by Siekhaus et al. [36], also using a Gaussian oscillator absorption model. However, we cannot directly compare higher energy absorption feature values found here to those reported by Siekhaus et al., as the latter used a Tauc-Lorentz type oscillator to describe the second, higher energy, critical point with a center energy at 3.5646 eV and an optical gap energy of 2.7289 eV. The Tauc-Lorentz oscillator was developed to describe only amorphous materials, and while data taken from a single-crystal material may be well matched using a Tauc-Lorentz oscillator, the physical meaning behind parameters is not known. Therefore, we have estimated Gaussian parameters, as used in this work, to approximate data gathered by Siekhaus et al. in order to better quantize the shift seen Figure 20. Estimated parameters are displayed in Table 3. The energetically lowest transition is determined to be shifted by only approximately 0.1 eV, while shifts of higher transitions are more significant perhaps due to a further oxidation layer on the 25.5 year aged single-crystal $UO_2$ used by Siekhaus et al., although this layer was not verified and it is unclear if such a layer was taken into account.

These optical transitions are feasible when considering calculated band structure, shown in Figure 14. The optical transition at roughly 2 eV is clearly connected to the band gap. The optical transitions at roughly 4.6 eV and 8 eV, corresponds to transitions from the high density of states at -2 eV and -4 eV ($E-E_F$), within the valence band, to unoccupied states at the bottom of the conduction band.

### 4.5 Conclusion

In conclusion, a metal-semiconductor Schottky barrier may be formed between the hyper-stoichiometric $UO_{2+x}$ and Ag, but the barrier height does not match the predicted barrier height. The C(V) measurement has a frequency dependent capacitance not normally observed in an metal-semiconductor Schottky device in reverse bias, indicating that a large defect concentration exists that may affect the ellipsometry data. A hyper-stoichiometric layer is the most likely source of this frequency dependent capacitance, which is supported by the XPS data. The I(V) and C(V) measurements show the bulk of the $UO_2$ semiconducting crystal appears p-type, and makes Ohmic contacts with both E-GaIn and Ag. The C(V) measurements provide a drift carrier lifetime between 50-250 $\mu$s. This is likely due to the narrowness of the $UO_{2+x}$ layer (< 40 Å), which allows Fowler-Nordheim tunneling, and reduces the effective barrier height from 1.5 eV to 1.28 eV. Ellipsometry confirms isotropic $UO_2$ with an approximate 2.0 eV band gap.

In the future, any devices fabricated from $UO_2$ single crystals will have to account for the oxygen diffusion to interstitial sites, and take steps to suppress this, or perhaps more interestingly, make use of this layer in depositing p-type materials to form p-n heterostructures.

### 4.6 References


[1] Stone, R. "Researchers Rise to Challenge of Replacing Helium-3," *Science,* vol. 353, no. 6294, pp. 15-16, 2016.

[2] Caruso, A., Billa, R., Balaz, S., Brand, J., and Dowben, P., "The Heteroisomeric Diode," *Journal of Physics Condensed Matter,* vol. 16, pp. L139-L146, 2004.

[3] Caruso, A., Dowben, P., Balkir, S., Schemm, N., Osberg, K., Fairchild, R., Flores, O., Balaz, S., Harken, A., Robertson, R., and Brand, J., "The All Boron Carbide Neutron Detector: Comparison with Theory," *Material Science Engineering B,* vol. 135, pp. 129-133, 2006.

[4] Hong, N., Mullins, J., Foreman K., and, Adenwalla, S. "Boron Carbide Based Solid State Neutron Detectors: the Effects of Bias and Time Constant on Detection Efficiency," *Journal of Physics D: Applied Physics,* vol. 43, no. 27, 2010.

[5] Peterson, G., Su, Q., Wang, Y., Dowben, P., and Nastasi, M. "Improved P-N Heterojunction Device Performance Induced by Irradiation in Amorphous Boron Carbide Films," *Material Science Engineering B,* vol. 202, pp. 25-30, 2015.

[6] Echeverría, E., Dong, B., Peterson, G., Silva, J., Wilson, E., Driver, M., Jun, Y., Stucky, G., Knight, S., Hoffman, T., Han, Z., Shao, N., Gao, Y., Mei, W., Nastasi, M., Dowben, P., and Kelber, J. "Semiconducting Boron Carbides with Better Charge Extraction through the Addition of Pyridine Moieties," *Journal of Physics D: Applied Physics,* vol. 49, pp. 355302, 2016.

[7] Anderson, H., Fermi, E., and Szilard, L., "Neutron Production and Absorption in Uranium," *Physical Review,* vol. 56, pp. 284-286, 1939.

[8] Meek, T. and von Roedern, B., "Semiconductor Devices Fabricated from Actinide Oxides," *Vacuum,* vol. 83, pp. 226-228, 2008.

[9] von Roedern, B., Meek, T., and Haire, M. "Some Electrical Properties of Ion-Implanted Urania - Part II," *Symposium of the Society for the Advancement of Material and Process Engineering (SAMPE),* Long Beach, 2003.

[10] Kruschwitz, C., Mukhopadhyay, S., Schwellenbach, Meek, T. and Shaver, B., "Semiconductor Neutron Detectors using Depleted Uranium Oxide," *Proceedings SPIE 9213; Hard X-Ray, Gamma-Ray, and Neutron Detector Physics XVI*, San Diego, 2014.

[11] Young, C., Petrosky, J., Mann, J.M., Hunt, E., Turner, D., and Dowben, P. "The Lattice Stiffening Transition in $UO_2$ Single Crystals," *Journal of Physics: Condensed Matter*, vol. 29-3, 2016.

[12] J. Katz and E. Rabinowitch, *Physical Properties of Uranium Metal*, *The Chemistry of Uranium*, New York: McGraw-Hill Book Company, 1951.

[13] Lynds, L., Young, W., Mohl, J., and Libowitz, G. "X-ray and Density Study of Nonstoichiometry in Uranium Oxides," *Nonstoichiometric Compounds*, *American Chemical Society*, pp. 58-65, 1963.

[14] D. J. Kim, J. H. Kim, K. S. Kim, J. H. Yang, S. K. Kim and Y. H. Koo, "Thermodynamic Assessment of $UO_2$ Pellet Oxidation in Mixture Atmospheres under Spend Fuel Pool Accident," *World Journal of Nuclear Science and Technology*, vol. 5, pp. 102-106, 2015.

[15] Dorado, B., Jomard, G., Freyss, M., and Bertolus, M.,"Stability of Oxygen Point Defects in $UO_2$ by First-Principles DFT+U Calcuations: Occupation Matrix Control and Jahn-Teller Distortion," *Physical Review B*, vol. 82, 2010.

[16] Kelly, T., Petrosky, J., Turner, D., McClory, J., Mann, J.M., Kolis, J., Zhang, X., and Dowben, P. "The Unoccupied Electronic Structure Characterization of Hydrothermally Grown $ThO_2$ Single Crystals," *Physica Status Solidi RRL*, vol. 8-3, pp. 283-286, 2014.

[17] Leinders, G., Cardinels, T., Binnemans, K., and Verwerft, M. "Accurate Lattice Parameter Measurements of Stoichioimetric Uranium Dioxide," *Journal of Nuclear Materials*, vol. 459, pp. 135-142, 2015.

[18] J. Holz, F. K. Schulte and H. Wagner, *Solid Surface Physics*, Berlin: Springer Berlin Heidelberg, 1979.

[19] Chiechi, R., Weiss, E., Dickey, M., and Whitesides, G. "Eutectic Gallium-Indium (EGaIn): A Moldable Liquid Metal for Electrical Characterization of Self-Assembled Monolayers," *Angewandte Chemie*, vol. 120, pp. 148-150, 2007.

[20] Kresse G., and Furthmuller, J. "Efficient Iterative Schemes for ab initio Total-Energy Calculations Using a Plane-Wave Basis Set," *Physical Review B*, vol. 54-16, pp. 169-186, 1996.

[21] Kresse, G. and Hafner, J. "Ab initio Molecular Dynamics for Liquid Metals," *Physical Review B*, vol. 47-1, pp. 558-561, 1993.

[22] Kresse, G. and Joubert, D. "From Ultrasoft Pseudopotentials to the Projector Augmented-Wave Method," *Physical Review B*, vol. 59-3, pp. 1758-1775, 1999.

[23] Perdew, J., Burke, K., and Ernzerhof, M. "Generalized Gradient Approximation Made Simple," *Physical Review Letters*, vol. 77-18, pp. 3865-3868, 1996.

[24] Paier, J., Marsman, M., Hummer, K., Kresse, G., Gerber, I., and Angyan, J., "Screened Hybrid Density Functionals Applied to Solids," *The Journal of Chemical Physics*, vol. 124, 2006.

[25] Sanville, E., Kenny, E., Smith, R., and Henkelman, G., "Improved Grid-Based Algorithm for Bader Charge Allocation," *Journal of Computational Chemistry*, vol. 28, pp. 899-908, 2007.

[26] Heyd J., and Ernzerhob, G., "Hybrid Functionals Based on a Screened Coulomb Potential," *The Journal of Chemical Physics*, vol. 118, pp. 8207-8215, 2003.

[27] Monkhorst, H., and Pack, J. "Special Points for Brillouin-Zone Integrations," *Physical Review B*, vol. 13-12, pp. 5188-5192, 1976.

[28] Clark, S., Segall, M., Pickard, C. Hasnip, P., Probert, M., Refson, K., and Payne, M. "First Principles Methods Using CASTEP," *Zeitschrift für Kristallographie - Crystalline Materials*, vol. 220, pp. 567-570, 2005.

[29] S. M. Sze and K. K. NG, *Physics of Semiconductors Devices*, New Jersey: Wiley-Interscience, 2007.

[30] Schoenes, J. "Optical Properties and Electronic Structure of $UO_2$," *Journal of Applied Physics*, vol. 49-3, pp. 1463-1465, 2008.

[31] Borchi, E., Bruzzi, M., Pirollo, S., and Sciortino, S. "Temperature and Frequency Dependence of the Capacitance of Heavily Irradiated Silicon Diodes," *Solid-State Electronics*, vol. 42-11, pp. 2093-2096, 1998.

[32] Wilis, B. "The Defect Structure of Hyper-Stoichiometric Uranium Dioxide," *Acta Crystallographica Section A*: *Crystal Physics*, vol. 34, pp. 88-90, 1978.

[33] Parker, I., "Carrier Tunneling and Device Characteristics in Polymer Light-Emitting Diode," *Journal of Applied Physics*, vol. 75, pp. 1656-1666, 1994.

[34] J. S. Morrell and M. J. Jackson, *Uranium Processing and Properties*, New York: Springer, 2013.

[35] Gofryk, K., Du, S., Stanek, C., Lashley, J., Liu, X., Schulze, R., Smith, J., Safarik, D. Byler, D., McClellan, K., Uberuaga, B., Scott B., and Anderson, D. "Anisotropic Thermal Conductivity in Uranium Dioxide," *Nature Communications*, vol. 5-4551, 2014.

[36] H. Fujiwara, *Spectroscopic Ellipsometry: Principles and Applications*, Tokyo: John Wiley & Sons, 2003.

[37] R. Azzam and N. Bashara, *Ellipsometry a Polaized Light*, New York: North Holland, 1978.

[38] Mock, A., Korlacki, R., Briley, C., Sekora, D., Hofmann, T., Wilson, P., Sinitskii, A., Schubert, E., and, Schubert M., "Anisotropy, Band-to-Band Transitions, Phonon Models, and Oxidation Properties of Cobalt-Oxide Core-Shell Slanter Columnar Thin Films," *Applied Physics*, vol. 108-5, 2016.

[39] Siekhaus, W., and Crowhurst, J. "Optical Properties of a Mechanically Polished and Air-Equilibrated [111] $UO_2$ Surface by Raman and Ellipsometric Spectroscopy," *IOP Conference Series: Materials Science and Engineering*, vol. 9-1, 2010.

[40] Peterson, G., Echeverria, E., Dong, B., Silva, J., Wilson, E., Kelber, J., Nastasi, M., and Dowben, P. "Increased Drift Carrier Lifetime in Semiconducting Boron Carbides Deposited by Plasma Enhanced Chemical Vapor Deposition from Carboranes and Benzenes," *Journal of Vacuum Science & Technology A: Vacuum Surfaces, and Films*, vol. 35-3, 2016.

[41] Riul Jr. A., Mills, C., and Taylor, D., "The Electrical Characteristics of a Heterojunction Diode Formed from an Aniline Oligomer LB-deposited onto Poly(3-methylthiophene)," *Journal of Materials Chemistry*, vol. 10, pp. 91-97, 1999.

[42] Schoenes, J "Optical Properties and Electronic Structure of $UO_2$," *Journal of Applied Physics*, vol. 49-3, pp. 1463-1465, 1978.

## V. The Debye Temperature of a Single Crystal Thorium Uranium Dioxide Alloy

This chapter is directly derived from a paper submission to *Physica Status Solidi Rapid Review Letters*. It is presently in press. It was modified to be consistent with the dissertation format. The collaborating authors are C. Dugan, C. Young, R. Carmona, M. Schneider, J. Petrosky, J. M. Mann, E. Hunt, and J. W. McClory. The journal article is titled, "The Debye Temperature of a Single Crystal Thorium Uranium Dioxide Alloy."

The unknown carrier type along an ill-defined junction from the Hall and I(V) measurements directed the research away from device fabrication and back to gaining a fundamental understanding of the electronic structure at the surface of $UO_2$. For many years, the potential challenge of understanding $UO_2$ crystals was its reactive surface. Using a hydrothermally grown s.c. $U_xTh_{1-x}O_2$ alloy in the device was considered a novel way to reduce progressive surface oxidation. In order to understand the alloy structure stability as compared to s.c. $UO_2$ and $ThO_2$, the Debye temperature was measured and compared to previous research.

### Abstract

The effective Debye temperature ($\Theta_{DE}$) of the surface of a single crystal of $U_{0.71}Th_{0.29}O_2$ alloy prepared by hydrothermal synthesis was obtained from temperature-dependent XRF in the temperature range of 300 to 623 K. The effective Debye temperature was determined to be 217 ± 24 K. X-ray fluorescence spectroscopy confirms the crystal's composition as $U_{0.71}Th_{0.29}O_2$. XPS reveals both thorium and uranium 4f states, which includes uranium and thorium in 4+ oxidation states. The effective Debye temperature of the single crystal $U_{0.71}Th_{0.29}O_2$ alloy, as measured via photoemission, is lower than $UO_2$ and $ThO_2$ literature values, indicating either higher defect scattering or the presence of added vibrational modes within the alloyed sample.

## 5.1 Introduction

The World Nuclear Association 2013 Global Nuclear Fuel Market Report indicates a 31% increase in uranium demand over 2013-2023. In addition, the worldwide electricity demand is expected to double from 2004 to 2030 and novel nuclear fuels could provide one solution [1]. Recent research is focused on alternative radioactive isotope fuels, such as thorium, to allow for new breeding or conversion fuels. Thorium is three to four more times more abundant in nature than uranium, and the desired isotope $^{232}$Th is nearly 100% of natural thorium such that enrichment is not required. Therefore, for all Th derived fuel, no enrichment is needed. In comparison, natural uranium is 0.71% $^{235}$U and 99.28% $^{238}$U. For light water reactors, the uranium must be enriched to 2-4 weight percent $^{235}$U for a light water reactor, which represents ~50% of the fuel cost.

When a nuclear reactor is operating at or near its maximum allowable power, the thermal conductivity of the fuel becomes an important parameter related to the fuel safety margin. This is complicated by the fact that thermal conductivity is a function of the temperature, fuel composition, porosity, deviation from stoichiometry, and burnup. Aside from the advantage of breeding new fissile fuel, $ThO_2$ has a thermal conductivity about 30% greater than of $UO_2$ at 373 K and about 8% greater at 923 K [1]. Since $UO_2$ has a lower thermal conductivity it has a higher power peaking factor for the fuel, reducing the allowable reactor power in order to meet safety margins for fuel damage. Furthermore, the melting temperature for $ThO_2$ is 3650 K, as compared to $UO_2$ at 3120 K, allowing for an additional safety margin if operated at the same temperature [2 - 4]. At high pressures, short-range forces increase significantly, changing uranium's coordination number and transforming uranium's phase whereas thorium's volume

change is significantly smaller [5-6]. It may be possible to take advantage of mixed alloy fuel to produce higher efficiency and safer reactors.

Photoemission spectroscopy is the measurement of the kinetic energy of electrons after exciting them with x-rays. The excited electron energy (as measured in an electron spectrometer) reflects the effect of binding energy and lattice vibrations. The number of atoms contributing to the photoemission signal, or signal intensity, provides a measure of the relative density of atoms contributing to energy transitions. Equation 5.1 provides a model of the entire transition current, where σ is the photoabsorption cross-section, E is the electron energy, $\hbar\omega$, is the photon energy, $\Delta k$, is the electron wave transfer vector, $G$ is the reciprocal lattice vector, and $U_0$ is the scattered nuclei mean displacement [7].

$$N(E,\hbar\omega) \propto |\sigma^2| \left( \overbrace{e^{-\Delta k^2 {U_0}^2}}^{\text{Direct electron current}} \sum_{G}^{n} \delta(\Delta k - G) + \overbrace{N\left(1 - e^{\Delta k^2 {U_0}^2}\right)}^{\text{Indirect current (phonon coupled transitions)}} \right) \quad (5.1)$$

The heat capacity of solids is largely dependent upon simple lattice vibrations. However, at temperatures important in nuclear reactors (~873-1273 K) assumptions regarding the vibrations in the lattice are no longer valid and the total vibrational energy, including harmonic frequencies, must be taken into account. A transition to a lower energy occurs at the Debye cutoff frequencies, which scales the heat capacity, so a relationship with normal modes can be made and the heat capacity as a function of temperature can be predicted. In general, a low Debye temperature means that the harmonic modes are more accessible.

## 5.2 Experiment

A sample of single crystal $U_{0.71}Th_{0.29}O_2$ grown by the hydrothermal process was measured via x-ray fluorescence spectroscopy using a Horiba micro-XRF analyzer. A 30 keV accelerating voltage was applied, providing a spot size of 100 μm. Four grid locations were selected and analyzed for 60 minutes each. X-ray spectral deconvolution was used for elemental identification using a Gaussian fit, providing mass percent, and atomic percent for all x-ray lines observed. For each grid location, the point data were removed, leaving only thorium and uranium consistently identified on the samples (oxygen is not measured). The atomic percent was then averaged over the four grids.

Photoemission spectroscopy required attaching the sample to a tantalum plate by spot welding a tantalum wire. Following mounting, the sample was sputtered at 1000 keV for 30 minutes in an attached external chamber held at $10^{-4}$ torr and a residual gas analyzer was used to assess the sputtered materials. Due to high concentrations of cesium on the surface from the growth process, the crystal was sputtered for an additional 90 minutes to remove all possible surface contamination. The sample was then transferred to the main photoemission spectroscopy chamber while still under vacuum and the system pumped to a stable $10^{-8}$ torr. The photoemission experiments utilized a VG Scienta R3000 electron analyzer and a Specs XR5 x-ray source of Al Kα radiation with a 50 meV step size. The spectral intensity was measured with a 100 eV pass energy using a constant 3000 watt x-ray power output from 800 to 650 eV binding energies to analyze the Th $4f_{5/2}$, Th $4f_{7/2}$, U $4f_{5/2}$, and U $4f_{7/2}$ peaks. The photoelectrons were collected normal to the sample surface while the x-ray source was offset from normal at a fixed 45° angle. Measurements were taken at 301, 323, 373, 423, 473, 523, 573, and 623 K, with a 30 minute delay in measurement after a stable temperature was reached in order to ensure sample

equilibrium. The spectra were computed in transmission mode from the average of five measurements.

### 5.3 Results

X-ray fluorescence (XRF) compositional analysis provided a uranium-thorium alloy of $U_{0.71}Th_{0.29}O_2$ with an atomic percent standard error of 0.36%. The temperature-dependent photoemission spectra for the Th *4f* and U *4f* spectra are shown in Figure 21(a) and Figure 22(a). In Figure 21 (a) the thorium binding energies (denoted as $E_F - E$), appear at 334.4 and 343.7 eV for Th $4f_{7/2}$ and Th $4f_{5/2}$ respectively and are consistent with the reported binding energies of [8] and [9]. The room temperature uranium binding energies (also denoted as $E_F - E$) occur at 391.3 and 380.3 eV for U $4f_{7/2}$ and U $4f_{5/2}$ respectively and are consistent with the reported binding energies of 390.8 [8] and 380.8 eV [10] and 390.9[11] and 380.1 eV [11].

The presence of and energy location of shake-up satellite peaks provides insight into the atomic composition of and oxidation states of thorium-uranium alloys as reported in [12], where thorium-uranium alloys have shake-up satellites in the 6.5 – 7.4 eV range for both oxides. Of particular note, if thorium is in the 4+ oxidation state the satellites are located at 7.0 – 7.4 eV [12]. Figure 21 (a) presents a thorium satellite peak energy of 7.4 eV, which matches the thorium 4+ oxidation state of composition $U_{0.75}Th_{0.25}O_2$ as reported in Anthonysamy et al. giving confidence to our XRF analysis. Additionally, Anthonysamy et al. reports that a 6.7 eV uranium satellite peak is present, indicating both $U^{4+}$ and $U^{6+}$ oxidation states are present in an alloy composition of $U_{0.75}Th_{0.25}O_2$. These are also observed in our data in Figure 22(a). The presence of these 6.7 eV peaks can be explained by assignment of the $U(4f^{13}\text{-}\ 5f^{2}{}_{5/2}5f^{1}{}_{7/2})O(2p^5)$ in the final state.[11] In Figure 22(a), the U 4*f* peaks have a higher intensity on the tail of the high-energy side than the Th 4*f* peaks, revealing the photoelectrons from the U 4*f* distributions are

scattered into the lower part of the spectrum due to electron inelastic scattering [11]. When the temperature increases, as shown in Figure 21(a) and Figure 22(a), lattice vibrations increase further lowering the photoelectron's energy and shifting the peak.

The corresponding 4*f* satellite peaks shown in Figure 21(b) and Figure 22(b) are associated with the Th-O and U-O bonding to the empty states above the fermi level. The energy from the 4*f* peaks to the satellite peaks, $\Delta E_{sat}$, characterize the chemical bond and oxidation state for both $UO_2$ and $ThO_2$. According to Anthonysamy et al., $ThO_2$ and $UO_2$'s shake-up satellite transition peak energies for the $Th^{4+}$, $U^{4+}$, and $U^{6+}$ oxidation states are at 7.3, 6.8, and 4.4 eV respectively higher in binding energy [12]. Our data does not reveal a strong Th-O satellite signal. Furthermore, the temperature dependence of the satellite peaks for U $4f_{5/2}$ in Figure 22 (a) are shifted above the primary peak at 6.7 eV until 623 K at which the satellite peaks are at 4 and 10 eV. This is above the previously published $UO_2$'s lattice stiffening transition at 475 K [11]. Although there are no other literature values in alloys, $\gamma - UO_3$ has two satellite peaks approximately 3.9 and 9.5 eV from the fundamental U 4*f* peaks [13]. It is clear from our data that the structure of the hydrothermally grown $U_{0.71}Th_{0.29}O_2$ alloy has the conformity of both $UO_2$ and $ThO_2$ and the 29% atomic fraction of Th in the alloy does not appreciably alter the electronic states of the $UO_2$; this also evidenced by the preservation of $\Delta E_{sat}$ for U $4f_{5/2}$ peak in the alloy.

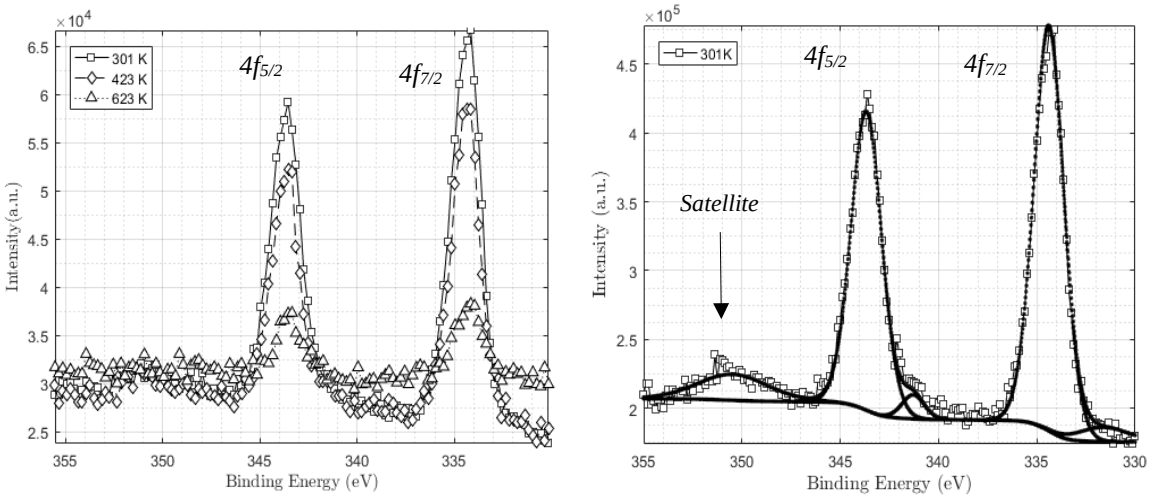


(a) (b)

**Figure 21. (a) XPS core level spectra for 301, 423, and 623 K in the region of the Th 4*f* shells. As the temperature is elevated the core level photoemission intensity declines sharply. (b) The thorium binding energy fits for 301 K reveal the 334.4 and 343.6 eV peaks for Th $4f_{7/2}$ and Th $4f_{5/2}$ respectively and the associated satellite peak. The fit also reveals an unknown peak at 341.5 eV. Data are shown plotting every 8th data point for clarity.**

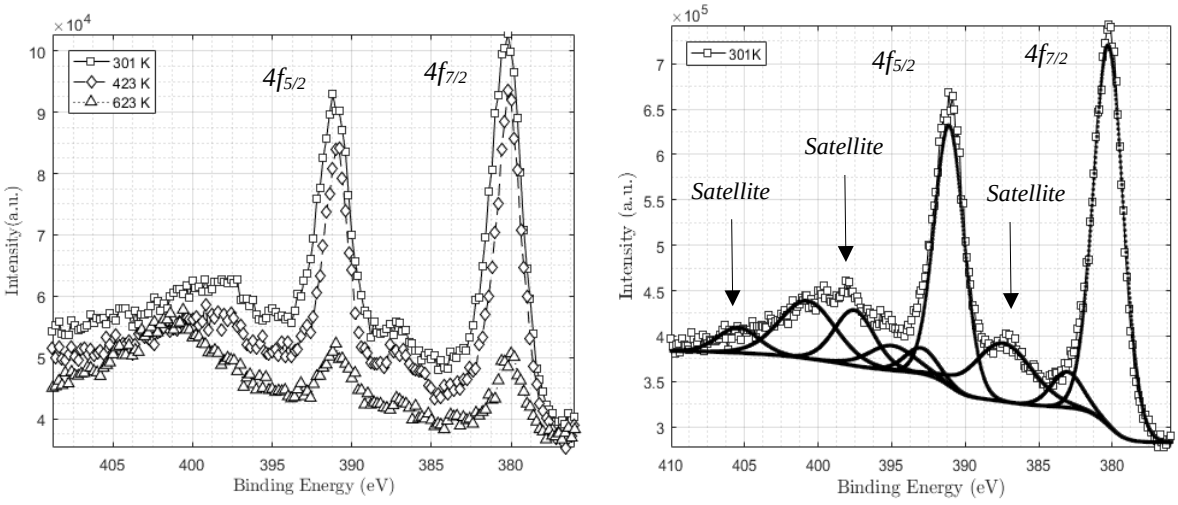


(a) (b)

**Figure 22. (a) XPS core level spectra for 301, 423, and 623 K in the region of the U 4*f* shells. As the temperature is elevated the core level photoemission intensity declines sharply. (b) The uranium binding energy fits for 380.3 K reveal the 391.3 eV peaks for U $4f_{7/2}$ and U $4f_{5/2}$ respectively and the associated satellite peak fits are shown at 301 K. Data are shown plotting every 8th data point for clarity.**

In tight binding systems, nuclear lattice vibrations are affected by atomic orbital electrons since they are connected to the vibrating uranium and thoria cores [7]. As temperature increases, the intensity of coherently scattered electrons decreases, which is the same intensity as measured by the photoemission spectroscopy. Mathematically, the temperature dependent peak intensity, *I*, is calculated by multiplying the initial transition intensity by $e^{-2W}$ as shown in Equation (5.2) where *W* is the Debye Waller factor, *T* is the sample absolute temperature, $\hbar\Delta k$ is the electron's momentrum transfer, *m* is the mass of the scattering center (either $^{232}$Th or $^{238}$U atom in this work), $k_B$ is Boltzman's constant, and $\theta_{DE}$ is the effective surface Debye temperature [7].

$$\boldsymbol{I = I_0 e^{-2W}} \text{ where } \boldsymbol{2W = \frac{3\hbar^2 \Delta k^2 T}{2 m k_B (\theta_{DE})^2}} \tag{5.2}$$

The term, $\Delta k$, is the change in wavenumber (shown in Equation 5.3) and is calculated from the kinetic energy, $E_{kin}$, of either the $^{232}$Th or the $^{238}$U atom's $4f_{5/2}$ or $4f_{7/2}$ shell, and the electron's mass, $m_e$.

$$\boldsymbol{\Delta k = \frac{\sqrt{2 E_{kin} m_e}}{\hbar c}} \tag{5.3}$$

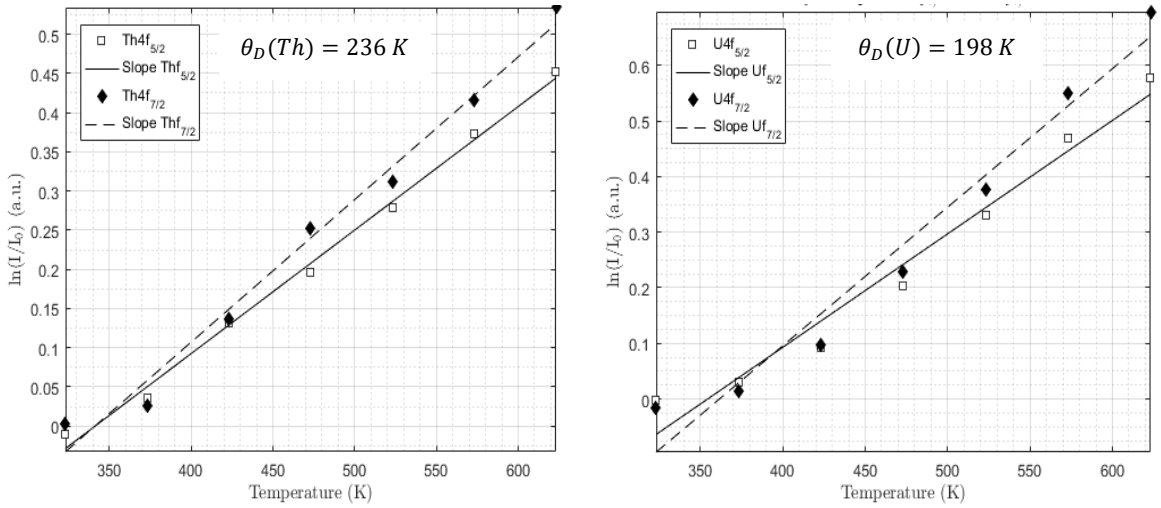


(a) (b)

**Figure 23. The natural logarithmic ratio of intensities as a function of temperature ranging from 301 to 623 K. The reference intensity, $I_o$, is the intensity for the room temperature measurement at 301 K. (a) The natural logarithmic slope for the Th 4$f_{5/2}$ and Th 4$f_{7/2}$ photoelectron is plotted along with the corresponding temperature measurements. (b) The natural logarithmic slope for the U 4$f_{5/2}$ and U 4$f_{7/2}$ photoelectron is plotted along with the corresponding temperature measurements.**

For a ternary alloy, such as $U_xTh_{1-x}O_2$, where the masses of the thorium and uranium atoms are much greater than the mass of the oxygen atom, the frequency distribution must be separated into at least two degenerate branches, with the heavier atoms each represented by the Debye acoustical branch and averaged for the entire system. Therefore, the Debye temperature was calculated from the slopes of the experimental data shown in Figure 23(a) and Figure 23 (b) as 236.3 ± 11 K for the thorium 4*f* peaks and 198 ± 13 K for the uranium 4*f* peaks. The averaged Debye temperature of 217 ± 24 K is found for the $U_{0.71}Th_{0.29}O_2$ alloy. The thorium and uranium weighted effective Debye temperature does not include a strong weight from the oxygen ligand or anharmonic contributions. Using the same methods as the present research, the Debye temperature of single crystal $ThO_2$ has previously been reported from experiment as 268 K [13] and 468 ± 32 K [5]. For comparison, the Debye temperature of single crystal $UO_2$ has been reported as 500 ± 59 K at temperatures below 475 K and 165 ± 21 K at temperatures greater than

475 K [11]. For comparison, the $ThO_2$ Debye temperature using experimentally determined elastic constants, was calculated at 297 and 370 K; note these are not single crystal samples [14]. Computational methods have provided a Debye temperature of 289.1 and 304.7 K [14]. Additionally, [15] presents a study of a full range of atomic fractions of $U_xTh_{1-x}O_2$ sintered pellets. Their work determined the Debye temperature directly, using low temperature heat capacity measurements, providing a bulk Debye temperature of 425 K for $ThO_2$, and nearly monotonically reducing to ~375 K at $UO_2$; again not single-crystal samples.

The reason for multiple Debye temperature constants is due to the difference in response of the 4 $f_{5/2}$ and 4$f_{7/2}$ photoelectron peaks, which overlap between the fitted Gaussian-Lorentzian peaks. In the present research, the $U_{0.71}Th_{0.29}O_2$ as a lower Debye temperature than calculated from photoemission experiments on similar growth $UO_2$ and $ThO_2$. This can be explained either by assuming that the Th/U alloy allows added vibrational modes to the crystal that are accessible at lower temperatures, or that there are additional defect scattering sites in the $U_{0.71}Th_{0.29}O_2$ samples that were not present in those being referenced in the literature samples [16].

**5.4 Conclusions**

An investigation of the Debye temperature for hydrothermally grown single crystal alloys of $U_{0.71}Th_{0.29}O_2$ has been conducted using photoemission spectroscopy and compared with similarly grown $ThO_2$ and $UO_2$. The alloy has a reduced Debye temperature while maintaining 4 f peak conformity. This result indicates that heat capacity is favorably raised for the ternary alloy, presenting a potentially added benefit in the use of the alloy as a mixed reactor fuel for either breeding or conversion fuel. The XPS result provides a path for further research as either added vibrational modes are accessed during heating or added defect scattering may occur due to

Th/U substitution. With the quality of the peak structure in these samples, temperature dependent cathodoluminescence would likely reveal defect states that become activated at elevated temperature. In either case, this may be a positive new growth method that can lead to uranium/thorium mixed fuels that maintain structural integrity under typical reactor conditions.

### 5.5 References


[1] W. N. Association, "Uranium Markets," February July 2017. [Online]. Available: http://www.world-nuclear.org/information-library/nuclear-fuel-cycle/uranium-resources/uranium-markets.aspx. [Accessed 23 05 2018].

[2] Peterson, S., Adams, R. and Douglas Jr., A., "Properties of Thorium, Its Alloys, and its Compounds," Oak Ridge National Laboratory, Oak Ridge, 1965.

[3] Bain, A., "The Heat Rating Required to Produce Central Melting in Various $UO_2$ Fuels," *Symposium on Radiation Effects in Refractory Fuel Compounds*, vol. 306, p. 30, 1962.

[4] International Atomic Energy Agency, "Thorium Fuel Utilization: Options and Trends," in *IAEA-TEDOC-1319*, Vienna, 2002.

[5] Anthonysamy S., Panneerselvam G., Santanu Bera S., Narasimhan S., P.R. Vasudeva Rao, 'Studies on Thermal Expansion and XPS of Urania-Thoria Solutions," *Journal of Nuclear Materials*, vol. 281, pp. 15-21, 2000.

[6] Aynas, M., Sanyal, A., and Jha, P. "Structural Phase Transition and Elastic Properties of Thorium Pnictides at High Pressure,"*Physica Status Solidi B*, vol. 229-3, pp. 1459-1465, 2002.

[7] S. Hufner, Stefan. *Photoelectron Spectroscopy Principles and Applications* (New York: Springer), 2003.

[8] Thorn, R. "Intensities and Satellites of 4*f*-Photoelectrons in Thorium and Uranium Dioxides," *The Journal of Physics and Chemistry Solids*, vol. 43-6, pp. 571-575, 1982.

[9] Kelly, T., Petrosky, J. McClory, J., Zens, T., Turner, D., "The Debye Temperature for Hydrothermally Grown $ThO_2$ Single Crystals," *Material Research Society Symposium*, Proceedings, vol.1576, 2013.

[10] Van den Berghe S., Miserque F., Gouder, T., Gaudreau B., Verwerft M. "X-ray Photoelectron Spectroscopy on Uranium Oxides: a Comparison between Bulk and Thin Layers," *Journal Nuclear Materials*, vol. 294, pp. 168-174, 201.

[11] Young, C., Petrosky, J., Mann, J., Hunt, E. Turner, D., Dowben, P. “The Lattice Stiffening Transition in $UO_2$ Single Crystals”, *Journal of Physics: Condensed Matter*, vol. 29-3, p. 035005, 2016.

[12] Teterin, Y., Kulakov, V., Baev A., Nevzoroz, Melnikov, I. Streltsov, Mashirov, L., Suglogov, Zelenkov, “A Study of Synthetic and Natural Uranium Oxides by X-ray Photoelectron Spectroscopy”, *Physics and Chemistry of Materials*, vol. 7, pp. 151-158, 1981.

[13] Ali, M., and Nagels, P. “Evaluation of the Debye Temperature of Thorium Dioxide,” *Physica Status Solidi*, vol.21-113, pp. 113-116, 1967.

[14] Kanchana, K., Vaitheeswaran G., Svane A., and Delin A. “First-principles Study of Elastic Properties of $CeO_2$, $ThO_2$ and $PoO_2$,” *Journal of Physics: Condensed Matter*, vol. 18, pp. 9615–9624, 2006.

[15] Muta, H., Murakami, Y., Uno, M., Kurosaki, K. and Yamanaka, S. “Thermophysical Properties of Th1-xUxO2 Pellets Prepared by Spark Plasma Sintering Technique,” *Journal of Nuclear Science and Technology*, vol. 50, pp. 181-187, 2013.

[16] Shind´e, L., Goela, J. *High Lattice Thermal Conductivity Solids*, New York: Springer, 2006.

## VI. A Comparison of Modulated Differential Scanning Calorimetry and Debye Temperature Determined Specific Heat Capacities of $UO_2$, $ThO_2$, and $U_{0.71}Th_{0.29}O_2$

This chapter is directly derived from a paper prepared for submission to *Physical Review B: Condensed Matter and Material Physics*. It was modified to be consistent with the dissertation format. The collaborating authors are C. Dugan, D. Felker, J. M. Mann, E. Hunt, J. W. McClory, and J. Petrosky. The journal article is titled, "A Comparison of Modulated Differential Scanning Calorimetry and Debye Temperature Determined Specific Heat Capacities of $UO_2$, $ThO_2$, and $U_{0.71}Th_{0.29}O_2$."

Typically, the Debye temperature is calculated from heat capacity results. We attempt to validate our novel photoemission-derived Debye temperature methods by computationally deriving the XPS heat capacity. We then compare to a standard heat capacity measurement using modulated differential scanning calorimetry, MDSC.


### Abstract

Temperature-dependent specific heat capacities for uranium dioxide, $UO_2$, thorium dioxide, $ThO_2$, and, $U_{0.71}Th_{0.29}O_2$ have been determined using a XPS-derived Debye temperature and compared to heat capacities obtained by the modulated-temperature differential scanning calorimetry (MDSC). The measurements cover the temperature ranges from 193 to 673 K. MDSC demonstrates single-crystal, s.c., actinides initially experience a higher heat capacity than amorphous $UO_2$ fuel pellets. Finally, the XPS derived heat capacities are lower than the MDSC determined heat capacities possibly due to cleaner, less oxidized crystal surface.


### 6.1 Introduction

Specific heat capacity measurements can provide intuition into the $UO_2$ crystal surface's stoichiometry. Specific heat capacity measurements of $UO_2$, $ThO_2$, and $U_xTh_{1-x}O_2$ have

previously been researched by drop calorimetric experiments and adiabatic shield calorimetry. Drop calorimetry is not well suited for resolving heat capacity behavior [1]. High-temperature heat capacity measurements of $UO_2$ and $ThO_2$ have been studied significantly for nuclear fuel applications. Likewise, low temperature (less than 40 K) heat capacity measurements have reported a sharp λ-type anomaly at 30.8 K indicating a first-order transition from the low-temperature antiferromagnetic state of type I that is associated with an internal distortion of the oxygen sub-lattice to a paramagnetic state [2]. There is a void in published literature for specific heat capacity measurements from 200 to 673 K, especially for hydrothermally grown s.c. actinide oxides.

One future application utilizing $UO_2$ is the fabrication of a $UO_2$ solid-state neutron detector [3]. Such device fabrication would require an extensive knowledge of $UO_2$ surface properties. The variation in $UO_2$'s carrier mobilities are influenced by surface oxidation and roughness. Schottky barrier formation may be possible, but it very much depends on the choice of contact and surface stoichiometry. Ohmic contacts have been favored [4].

Uranium dioxide's surface structure, reduction or oxidation potential, and chemical reactivity play a significant role in solid-state device fabrication. Material doping and hence device conductivity is dependent on oxygen atom mobility through $UO_2$'s fluorite lattice. An n-type $UO_{2-x}$ and $UO_2$ surface is created as oxygen migrates through lattice vacancies. On a $UO_{2+x}$ surface, interstitial oxygen migration dominates, creating a p-type semiconductor. [5] Argon sputtering of (111) $UO_2$ crystal surface results in reducing $U^{4+}$ cations into U metal atoms or other lower oxidation states potentially creating a hypostoichiometric surface [5]. First principle calculation of $UO_2$ surface chemistry provides a theoretical approach to understanding $UO_2$

surface energy. Experiments have uncovered that water reacts with $UO_2$ surfaces and the amount of reaction is geometrically dependent [6].

### 6.2. Experiment

Modulated differential scanning calorimetry (MDSC) is a thermal analysis technique measuring the temperature and heat flow associated with thermal transitions in a material. The MDSC experiments were carried out on a TA instruments Model DSC 2500 differential scanning calorimeter at a ramp rate of 1 °C/min. The temperature was modulated at 273.65 K (0.05 °C) for 75 seconds. Temperature calibrations were conducted with indium, tin, lead, and zinc. T-zero calibrations for heat capacity were performed with sapphire standards. Using a liquid nitrogen cooled system, the temperature range was calculated from 193 to 673 K. The sample was enclosed in a recyclable aluminum pan and compared to an empty aluminum reference pan. The sample and reference pans masses were calibrated to within ±0.01 mg. Sample/pan and reference pans were mechanically placed on separate raised platforms and then surrounded by the furnace. As the frequency dependent furnace temperature increased, both sample/pan and reference were heated. Thermocouples recorded the differential temperature recorded between the sample/pan and the reference pan, which provided the differential heat flow. Due to observed data variations, three iterations were measured for each sample. The first measurement for all s.c. samples presented a lower specific heat capacity than the second and third measurement. The second and third measurements were consistent for all actinide oxide samples.

In previous work, XPS spectra were taken with a constant 300-watt x-ray power output from 800 to 650 eV binding energies to analyze the Th $4f_{5/2}$, Th4 $f_{7/2}$,U $4f_{5/2}$, and U $4f_{7/2}$ peaks at increasing temperatures. The photoelectrons were collected normal to the sample surface while

the x-ray source was offset from normal at a fixed 45° angle. Temperatures were raised from room temperature allowing the surface to stabilize at the measurement temperature for 30 minutes to minimize mechanical fluctuations and to ensure surface stabilization [7-9].

### 6.3 Theory

Specific heat is a measure of how thermally insensitive a substance is to the addition of energy. The heat capacity at a constant volume is defined as the change in internal energy as $C_v = {\delta U}/{\delta T}$ where *U* is the energy and *T* is the temperature. Expanding on Einstein's theory on particle motion in a solid, Debye recognized there is a maximum number of vibrational modes, $\upsilon_D$ available in any system. Assuming three phonon modes associated with N primitive cells, the total phonon energy would be defined as

$$U = 9Nk_B T\left(\frac{T}{\theta}\right)^4 \int_0^{x_D} \frac{x^3}{e^x - 1} dx, \tag{6.1}$$

where $x_D$ is

$$x_D \equiv \frac{\hbar\omega_D}{k_B T} \equiv \frac{\theta}{T} \text{ [10].} \tag{6.2}$$

Therefore, heat capacity with constant volume and constant pressure, $C_V$ and $C_P$ is defined respectively as

$$C_V(T) = 3n_A R B_3(2, x_D), \text{and} \tag{6.3}$$

$$C_P(T) = C_v(T) + A_0[C_v(T)]^2 \frac{T}{T_m}. \tag{6.4}$$

In Equation (6.3) and (6.4), R is the gas constant, $n_A$ is the number of atoms in a mole, $A_0 = 5.1x10^{-3} J^{-1} K * mol$, and $T_m$ is the melting temperature. $B_n(\beta, x_D)$ is the n-dimensional second kind Debye integral defined by Equations (6.5) and (6.6) with $x_D = {\theta_D}/{T}$. Debye temperature-dependent specific heat capacity results assume a 1-dimensional second kind Debye integral.

$$B_n(2, x_D) = \frac{n}{n+1} x_D[D_{n+1}(\beta - 1), x_D) + D_{n+1}(\beta, x_D)] \tag{6.5}$$

$$D_n(2, x_D) = \frac{n}{x_D^n} \int_0^{x_D} \frac{x^n}{(e^x - 1)^\beta} dx \tag{6.6}$$

$$C_P(T) = 3n_A R B_n(2, x_D)\{1 + 3n_A A_0 R \left(\frac{T}{T_m}\right) B_n(2, x_D)\} \tag{6.7}$$

Expanding the square root in Equation (6.4) and substituting Equations (6.5) and (6.6), the simple structure for heat capacity and thermal expansion can be found with Equation (6.7) [11]. Therefore, the specific heat capacity can be calculated once the Debye temperature is known. A more common method to determine specific heat capacity is MDSC. MDSC depends on the traditional DSC thermally equivalent ohm's law, $dQ = dT/R$ where dQ is the difference in heat flow between the sample and the reference, $dT$ is the temperature difference measured, and $R$ is the thermal resistance of the cell [12]. With modulation, a variable heating rate is applied to the sample/pan and the reference pans via the furnace. A periodic-sinusoidal ripple is overlaid on the standard linear temperature ramp. The heating rate, amplitude of modulation, and frequency of modulation heat flow rate are applied in Equation 6.8.

$$\Phi(T, t) = C_p \beta_o + \Phi^{ex.}(T, t) + C_p T_A \omega \cos(\omega t) + \frac{\delta \Phi^{ex.}(T_u, t)}{\delta T} T_A \sin(\omega t) \tag{6.8}$$

In Equation (6.8) $C_p$ is the heat capacity, $\beta_o$ is the underlying heating rate, $\Phi^{ex.}(T, t)$ represents the endothermic or exothermic latent heat exchange, $T_A$ is the amplitude, $\omega$ is the modulation frequency, and $T_u$ represents the mean temperature around fluctuations, $T_u = T_0 + \beta_o t$ [13].

**6.4 Results**

As observed, specific heat capacity increases with temperature. In Figure 24 the specific heat capacities of $UO_2$, $ThO_2$, and $U_{0.71}Th_{0.29}O_2$ increase from 300 to 650 K. The measurements in Figure 24 employ previously published XPS-calculated Debye temperatures to provide insight into the surface specific heat capacity of $UO_2$, $ThO_2$, and $U_{0.71}Th_{0.29}O_2$ [7-9]. The calculated heat capacity of $ThO_2$ is mathematically extrapolated from 375 to 650 K for data comparison. The shaded regions represent the error in the plotted heat capacity data due to experimental error from the XPS measurements. For reference, Figure 24 provides empirically calculated values from the Willis' neutron diffraction study, with calculated Debye temperatures of 377 and 393 K for $UO_2$ and $ThO_2$ respectively [14].

Our data provides the Debye temperature-calculated specific heat capacities of $UO_2$ and $ThO_2$ at room temperature as 71.85 and 71.85 [J/K mol]. These values are lower than previously published values from Willis, 75.45 and 75.20 [J/K mol], but higher than other published room temperature specific heat capacities of 63.60 and 61.91[J/K moll] for $UO_2$ and $ThO_2$ respectively [15-17]. An abrupt shift is observed in the calculated heat capacity for $UO_2$, which occurs at 475 K and is a result of a lattice stiffening transition characterized by dissimilar regions of different Debye temperatures [7]. The $U_{0.71}Th_{0.29}O_2$ crystal also presents the highest temperature dependent heat capacity. This is most likely due to more entropy or lattice strain in the mixed actinide lattice structure. This behavior is governed by progressive excitation of the harmonic lattice vibrations with a smaller contribution from thermal excitations of localized electrons of the $U^{4+}$ and $Th^{4+}$ in the crystal field [13].

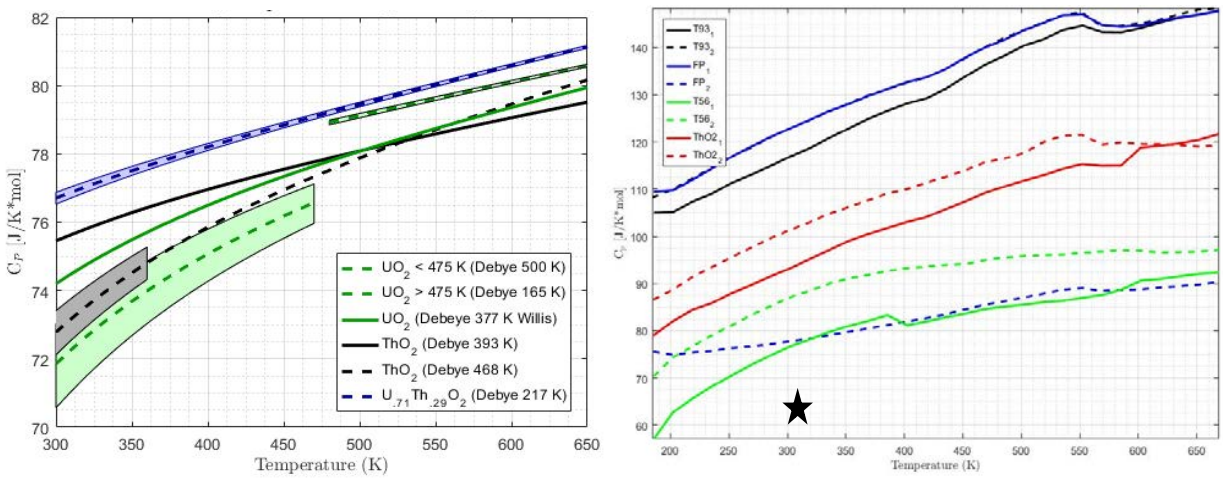


**Figure 24. Specific heat capacities for $ThO_2$, $UO_2$, and $U_{0.71}Th_{0.29}O_2$ for temperatures ranging from 300 to 673 K. As observed in the left figure, the dashed lines represent specific heat calculated utilizing XPS determined Debye temperatures. The shaded regions represent experimental uncertainties with previously calculated Debye temperatures. The solid lines reference previously published Debye temperatures. As shown in the right figure, the MDSC calculated heat capacity of an amorphous fuel pellet is compared to the specific heat capacity s.c. $UO_2$ and $ThO_2$. Note a later hydrothermal growth, solid line, increases the heat capacity of the s.c. $UO_2$. The solid lines are the first MDSC measurement results. Dashed lines represent measurements 2 and 3 for each sample. The star denotes calculated specific heat capacity values at 300 K derived the from $UO_2$ temperature dependent heat content equation at 63.6 [J/K mol] utilizing a drop calorimetry measurements [18].**

Our data provides the specific heat capacity of $UO_2$ and $ThO_2$ from MDSC as shown in Figure 24. The $UO_2$ fuel pellet heat capacity is the lowest calculated from MDSC measurements but still higher than any $UO_2$ surface heat capacity found in Figure 24. Notice the significantly decreased specific heat capacity for the $UO_2$ fuel pellet for subsequent measurements. The room temperature specific heat capacity decreases from 114.4 to 75.7 [J/K mol]. The sintered fuel pellet may initially present as a fully oxidized fuel pellet of many stoichiometric uranium oxides with a higher entropy due to the abundance of oxygen on the fuel pellet's surface [17]. The $UO_2$ represented by the solid line is an earlier hydrothermal growth than the higher heat capacity solid black line measurement. Likewise, the specific heat capacities of the $ThO_2$ samples increase with subsequent measurements. At 300 K the $ThO_2$ specific heat capacity increases from 85.8 to 94.0 [J/K mol]. Also, the $UO_2$ specific heat capacity increases from 68.2 to 78.9 [J/K mol] and

108.0 to 114.0 [J/K mol]. The specific heat capacity rise of approximately 8 [J/K mol] could be due to introduction of more oxygen into the $UO_2$ and $ThO_2$ due to the oxidation brought forth from heating the samples. Grenthe et al. provides validation to this theory as an increase in the hyperstoichiometry of $UO_2$ increases its specific heat capacity [17]. Finally, the largest specific heat capacities are produced by uranium hydrates with room temperature heat capacities of approximately 141 [J/K mol], closely resembling the initial specific heat capacity of the fuel pellet $UO_2$ [17]. The solid blue and black $UO_2$ specific heat capacity shown in Figure 24 presents a peak at approximately 540 K. Previous research has identified a change in Debye temperature around 475 K suggesting a $UO_{2+x}$ to a $UO_{2+x}$ and $U_4O_{9-y}$ transition between 473 and 670 K [8]. The black star denotes a specific heat capacity obtained from a polynomial fit of $UO_2$'s heat content [18].

The MDSC experimentally determined specific heat capacities are significantly higher than the XPS derived heat capacities. One potential reason for the wide range of discrepancy presented in the specific heat capacity measurements could be the stability of the $UO_2$ and $ThO_2$ surfaces. The XPS measurements were taken under ultra-high vacuum after the surface was cleaned by argon sputtering. At atmospheric pressure, the $UO_{2+x}$ phase diagram provides evidence of temperature-dependent multiple phase and stoichiometric changes of uranium oxide. The XPS specific heat capacity data was performed on s.c. actinide oxides routinely appears slightly higher than previously measured data. It is feasible this elevated specific heat capacity could more accurately represent pure $UO_2$ and $ThO_2$ crystals than formerly researched.

### 6.5 Conclusion

Variation in previously published results may be attributed to dissimilarities in material structure, bulk versus surface measurements, disparity in crystal quality, and the measurement

environment. It appears the most accurate way to quantify the specific heat capacity of s.c. $UO_2$ and $ThO_2$ crystals is in an ultra-high vacuum where there is the capability to remove surface oxidation. Common specific heat capacity measurement techniques such as MDSC alter the specific heat capacity of easily oxidized crystals, such as actinide oxides, during measurement.

### 6.6 References


[1] Gronwold, F. Kveseth, N., Sveen, A., and Tichy, J. "Thermodynamics of the $UO_{2+x}$ phase I. Heat Capacities of $UO_{2.017}$ and $UO_{2.254}$ from 300 to 1000K and Electronic Contributions," *Journal of Chemical Thermodynamics*, vol. 2-5, pp. 665 – 679, 1970.

[2] L. Morss, N., Edelstein, and J. Fuger. "The Chemistry of the Actinide and Transactinide Elements, 3rd edition, Netherlands: Springer, 2006.

[3] Kruschwitz, C., Mukhopadhyay, S., Schwellenbach, D., Meek, T., and Shaver, B., "Semiconductor Neutron Detectors using Depleted Uranium Oxide," *SPIE Proceedings*, vol. 9213 (2014).

[4] Dugan, C., Peterson, G., Mock, A., Young, C. Mann, J., Natashi, M., Schubert, M., Wang, L., Mei, W., Tanabe, I., Dowben, P., and J. Petrosky, "Electrical and Material Properties of Hydrothermally Grown Single Crystal (111) $UO_2$," *European Journal of Physics B*, vol. 91-67, 2018.

[5] Idriss, H., "Surface Reactions of Uranium Dioxide Powdered, Thin Films and Single Crystals," *Surface Science Reports*, vol. 65, pp. 67-109, 2010.

[6] Maldonado, P., Evins, L, and Oppeneer, P., "Ab Initio Atomistic Thermodynamics of Water Reacting with Uranium Dioxide surfaces," *The Journal of Physical Chemistry C*, vol. 118, pp. 8491 – 8500, 2014.

[7] Kelly, T., Petrosky, J. McClory, J., Zens, T., and Turner, D., "The Debye Temperature for Hydrothermally Grown $ThO_2$ Single Crystals," *Material Research Society Symposium, Proceedings*, vol 1576, 2013.

[8] Young, C., Petrosky, J., Mann, J., Hunt, E., Turner, D., and Dowben, P., "The Lattice Stiffening Transition in $UO_2$ Single Crystals," *Journal of Physics: Condensed Matter*, vol. 29-3, p. 035005, 2017.

[9] Dugan, C., Young, C., Carmona R., Schneider, M., McClory, J., and Petrosky, J., "The Effective Surface Debye Temperature of Single Crystal Uranium Thorium Dioxide," *Physica Status Solidi, Rapid Review Letters*, In Press.

[10] Kittel, Charles. *Introduction to Solid State Physics*, New Jersey: John Wiley & Sons, Inc, 2005.

[11] Eser, E., Koc, H., Gokbulut, M., and Gursoy, G., "Estimations of Heat Capacities for Actinide Dioxide: $UO_2$, $NpO_2$, $ThO_2$, and $PuO_2$," *Nuclear Engineering and Technology*, vol. 46, pp. 863 – 868, 2014.

[12] Gill, P. S., Sauerbrunn, S.R., and Reading, M. "Modulated Differential Scanning Calorimetry," *Journal of Thermal Analysis*, vol. 40, pp. 931-939, 1993.

[13] G. Hohne, W. F., Hemminger, and H.-J. Flammersheim, *Differential Scanning Calorimetry* Heidelberg: Springer, Berlin, 2003.

[14] Willis, B. "Neutron Diffraction Studies of the Actinide Oxides II. Thermal Motions of the Atoms in Uranium Dioxide and Thorium Dioxide Between Room Temperature and 1100 °C," *Proceedings of the Royal Society A*, vol. 274, p. 134, 1963.

[15] Fink, J.K. "Enthalpy and Heat Capacity of the Actinide Oxides," *International Journal of Thermophysics*, vol. 3, pp.165-200, 1982.

[16] Osborne, D., and Westrum, E. "The Heat Capacity of Thorium Dioxide from 10 to 305°K. The Heat Capacity Anomalies in Uranium Dioxide and Neptunium Dioxide," *The Journal of Chemical Physics*, vol. 21, 1884 – 1887, 1953.

[17] I. Grenthe, J. Fuger, R., Konings, R. Lemire, A. Muller, C. Nguyen-Trung, and H. Wanner, *Chemical Thermodynamics of Uranium*, Netherlands: North-Holland, 1992.

[18] J. Katz, and E. Rabinowitch, *The Chemistry of Uranium*, New York: McGraw-Hill Book Company, Inc., 1951.

## VII. Surface-Depth Profiling of an Oxidized Single-Crystal $UO_2$ Surface by Angle-Resolved X-ray Photoemission Spectroscopy

This chapter is derived from a paper prepared for submission to *Physica Status Solidi Rapid Review Letters*. It was modified to be consistent with the dissertation format. The collaborating authors are C. Dugan, R. Carmona, A. Pelton, A. Peterson, J. Petrosky, J. M. Mann, E. Hunt, and J. W. McClory. The journal article is titled, "Surface-Depth Profiling of an Oxidized Single-Crystal $UO_2$ Surface by Angle-Resolved X-ray Photoemission Spectroscopy."

The heat capacity and Debye measurements suggest an oxidized $UO_2$ surface for hydrothermally grown s.c. $UO_2$. The oxidation depth and surface stoichiometry are made relevant to device fabrication with the Hall and I(V) measurements. This study used angle resolved x-ray photoemission spectroscopy to examine the oxidation states of $UO_2$ as a function of depth in a roughly polished sample. The technique evolved from understanding the XPS determined Debye temperature spectra, as localized f-shell transitions and satellite peaks provide a better understanding of the surface characteristics. In this paper we relate the hydrothermally grown s.c. $UO_2$ sample oxidation to uranium metal and $UO_2$ crystals grown by various other methods.

### Abstract

Oxidation of the $UO_2$ surface has plagued the actinide community's understanding of uranium dioxide's surface properties. Here we measure the valence-band edge, O 1*s* peak, and U 4*f* orbitals using angular-resolved XPS spectra for a rough-polished, single crystal, hydrothermally grown, $UO_2$ sample. Satellite peaks have been deconvolved for all spectra, and where possible, compared to literature values. The $UO_2$ rough polished surface is representative of naturally occurring $UO_2$ and a comparison is provided with previously published clean

samples. An oxidized surface is confirmed with an increase in the binding energies of the U 4*f* peaks. Peak deconvolution of the U $4f_{7/2}$ peak provides evidence of $U^{4+}$ and $U^{6+}$ oxidation states confirming we have not probed to a stoichiometric $UO_2$ bulk region, likely revealing a selvedge region near the surface with increasing $UO_2$ at greater depths. Analysis of the U 4*f* shake-up satellite peaks indicates mixed oxidation states on the $UO_2$'s surface. The shifting of the U $4f_{7/2}$ peak energy and the peak convolution of the O 1*s* peak affirms the presence of surface water. The presence of U 5*f* peaks in the valence band spectra provides evidence of the $U^{4+}$ oxidation state, but does not refute the presence of the $U^{6+}$ oxidation state. The electronic band-gap energy of 2.2 eV confirms the presence of the $UO_2$ structure. Possible explanations for these results are well supported in the literature, as oxidation of the surface of the $UO_2$ crystal incorporates oxygen into the interstitial sites in the lattice to form a $UO_{2+x}$ surface [1-4].

### 7.1 Introduction

Current and future applications of $UO_2$ are hampered by its reactive surface. Dry-stored irradiated nuclear fuel, which began as sintered $UO_2$, will oxidize to $U_3O_8$ at temperatures ranging from 423 to 443 K [1]. Oxidation of $UO_2$ consists of two oxidation steps: $UO_2$ oxidizes to form $U_3O_7$ and $U_4O_9$, which then oxidizes to form $U_3O_8$. The $UO_2$ fluorite structure is ionic and provides an avenue for oxygen to fill lattice vacancies, displacing U and eventually producing $U_3O_7$ and $U_4O_9$. These oxides have a higher density that $UO_2$, and a reduced volume. The second reduction forms $U_3O_8$, which is 23% less dense than $UO_2$ and has a 36% volume increase, splitting fuel element sheaths [5]. Understanding how the surface oxidation may be affected by growth and processing is of key importance to development of safer, more stable fuels.

Uranium dioxide's oxygen potential is a function of stoichiometry and temperature. It has been reported that under ultra-high vacuum (UHV) the $UO_2$ surface becomes contaminated after a period of about 100 minutes [6]. $UO_2$ is known to oxidize at room temperature and a $U_3O_7$ phase is formed when $UO_2$ is oxidized below 400 K [7]. Previously, XPS studies of uranium oxide surfaces included angle-resolved studies of the $UO_2$ valence band [8], uranium metal oxidation [9], $UO_2$ shake-up peaks for the U 4*f* shell [3], oxidation of uranium oxides via comparison of O 1*s* and U 4*f* peaks [6], and the relation of 4*f* satellite peaks to ionization [11].The photoelectron escape depth in $UO_2$ is less than 50 Å [7], making angled-resolved x-ray photoemission spectroscopy (AR-XPS) the preferred technique to surface profile the $UO_2$ surface and selvedge region. Here we measure the valence-band edge, O 1*s* peak, and U 4*f* orbitals photoemission spectra at several angles using XPS for hydrothermally grown s.c. $UO_2$. Satellite peaks have been deconvolved for all spectra and where possible compared to literature values. The $UO_2$ surface is representative of naturally occurring $UO_2$ and a comparison is provided with previously published data.

**7.2 Experiment**

A hydrothermally-grown s.c. $UO_2$ was mounted on a nonmagnetic stainless steel plate via spot welding of a tantalum wire and degreased using HPLC grade methanol in preparation for AR-XPS. It was analyzed in an Omicron Multiprobe XPS with an Argus 124-mm hemispherical analyzer with a 128 channel detector. An Omicron XM 1000 Mk11 x-ray source produced mono-chromatic Al Kα x-rays at 225 W. The instrument was operated at $3\times10^{-9}$ mbar and kept at room temperature. The instrument was operated in constant analyzer energy (CAE) mode with a pass energy of 25 eV and a 0.2 eV step size. The spectra were measured at incident angles of 34, 44, 49, 54, and 64° between the sample plate and the x-ray source. The

spectrometer energy scale was calibrated using copper; the carbon 1*s* graphitic feature was fixed at 285 eV for calibration.

The spectra were curve fit using CasaXPS with a 70% Gaussian/30% Lorentzian distribution for core electrons and an asymmetric Lorentzian for valence-band edge electrons. Shirley backgrounds were applied to all binding energy spectra. The major regions studied were the valence-band region (15 to 0 eV), the O *1s* region (540 to 525 eV), and the U 4*f* region (410 to 375 eV).

## 7.3 Results

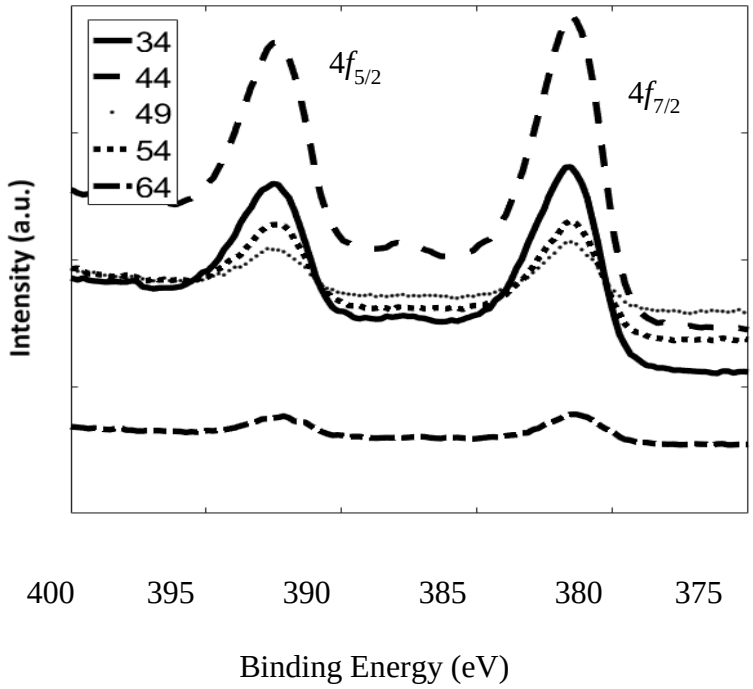


**Figure 25. AR-XPS spectra of the U 4*f* shell spectra collected from angles of 34, 44, 49, 54, and 64° between the surface and the x-ray source with 34° representing the most-surface sensitive measurement.**

### *7.3.1 Binding Energies of U 4f Core Level Peaks*

Figure 25 presents the AR-XPS core level spectra for s.c. $UO_2$ surface. The most-surface sensitive measurement is 34°, providing the greatest angle between the x-ray gun and the $UO_2$ surface. In Figure 26 the hyperfine splitting of the U 4*f* orbital is represented by two peaks representing the U $f_{7/2}$ and U $f_{5/2}$ energy levels. The U $f_{7/2}$ peaks are located at 381.7, 381.6, 381.7, 381.6, and 381.5 eV for angles 34, 44, 49. 54 and 64° respectively. These binding energies are higher than the reported literature values of [7] and [11] of 380.1, 380.2, and 380.3 eV for $UO_{2.11}$ pellets, $UO_2$, and $UO_2$ in equilibrium with U. Likewise the U $f_{5/2}$ peaks are located at 392.5, 392.5, 392.6, 392.5, and 392.2 eV for angles 34, 44, 49. 54 and 64° respectively. These binding energies are higher than [12] at 390.9 eV, but in agreement with [13], which was a measurement on an oxidized $UO_2$ surface.

These peaks represent the contribution from the binding energies of both $U^{4+}$ and $U^{6+}$ oxidation states, and the contributions can be determined by deconvolving the primary sum peaks. In Figure 26(a) and Figure 26(b) we show the peak deconvolution of the U $4f_{7/2}$ and U $4f_{5/2}$ peaks at two angles, 34 and 49° indicating two resolvable peaks. Since the $U^{6+}$ is

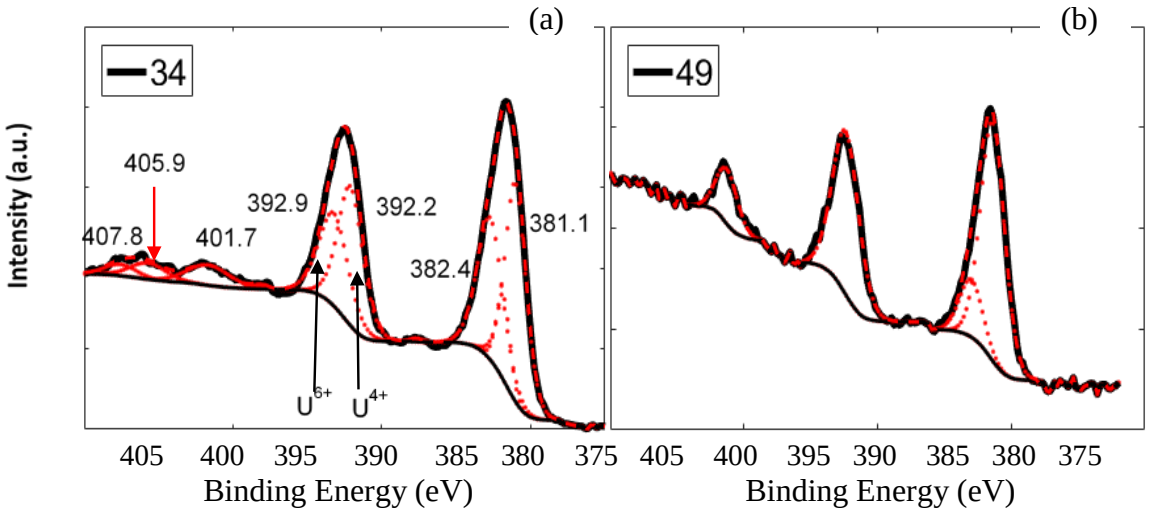


**Figure 26. The U 4*f* shell binding energies are peak deconvolved for 34 and 49° respectively. The dotted red lines represent the individual deconvoluted peaks, while the red dashed line is the summation of the peak deconvolution. Also provided are the various shakeup satellite peaks and their energy representation.**

expected to have a higher binding energy, the higher energy peak is assumed to be associated with the $U^{6+}$ oxidation state. This assumption is supported by the location of the satellite peaks, presented in the following paragraphs. The specific binding energies found by deconvolution are provided in Table 4.

**Table 4. The angle-dependent U $4f_{7/2}$ and U $4f_{5/2}$ peak deconvoluted binding energies (eV) for the U $4f_{7/2}$ and U $4f_{5/2}$ sum of hydrothermally-grown s.c. $UO_2$.**

| | 34° | 44° | 49° | 54° | 64° | |
|---|---|---|---|---|---|---|
| | | | U $4f_{7/2}$ | | | |
| $U^{4+}$ | 381.1 | 381.0 | 381.4 | $4f_{5/2}$ | $4f_{7/2}$ | |
| $U^{6+}$ | 382.4 | 382.0 | 383.1 | | 381.3 | |
| | | | U $4f_{5/2}$ | | | |
| $U^{4+}$ | 392.2 | 392.0 | ** | 392.2 | 392.2 | $U^4$ |
| $U^{6+}$ | 392.9 | 392.8 | ** | 393.7 | 394.0 | |

**Peak not resolved. Sum peak located at 392.4 eV.

Shown in Figure 26(a) and Figure 26(b) are the presence of shakeup satellite peaks for 34 and 49°, which result from electron absorptions near the valence band. These absorptions reduce the kinetic energy of the emitted photoelectron; this presents as a higher binding energy. These peaks can help identify oxidation states of the uranium atoms.

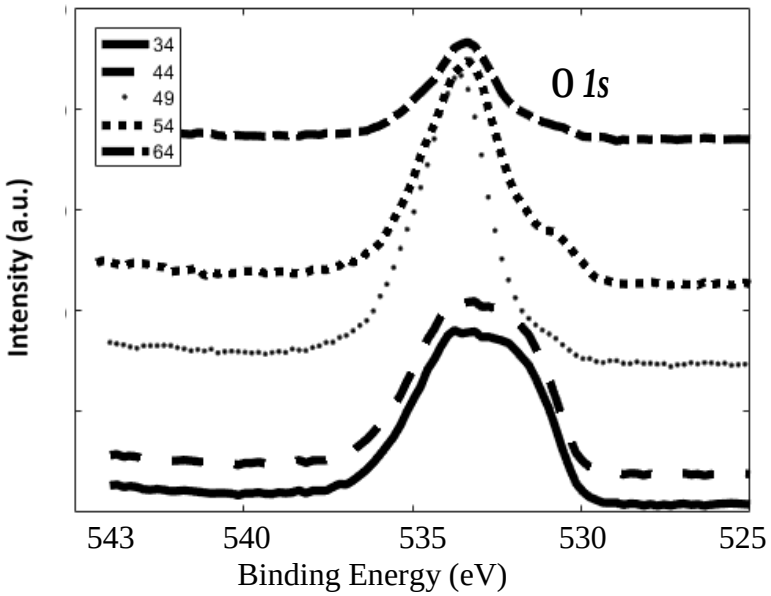


**Figure 27. Angle-resolved XPS core level spectra in the regions of the O 1*s* shell. The angle dependent spectra collected from angles of 34, 44, 49, 54, and 64°between the surface and the x-ray source with 34° representing the most-surface sensitive measurement.**

*7.3.2 Binding Energy of O1s.*

Figure 27 presents the AR-XPS O 1*s* spectra for s.c. $UO_2$ surface, with the most surface sensitive measurement being at 34°. In Figure 28, the O 1*s* sum peaks are located at 533.3, 533.1, 533.6, 533.4, and 533.4 eV for angles 34, 44, 49. 54 and 64° respectively. Allen et al., published the binding energy of the O 1*s* peaks for heated and cooled $UO_2$, powdered $UO_2$, $UO_{2.1}$, $UO_{2.2}$, $U_4O_9$, $U_3O_7$, and $U_3O_8$ at 530.4, 530.4, 530.3, 530.6, 530.2, 530.1, and 530.1 ± 0.2 eV respectively [7].

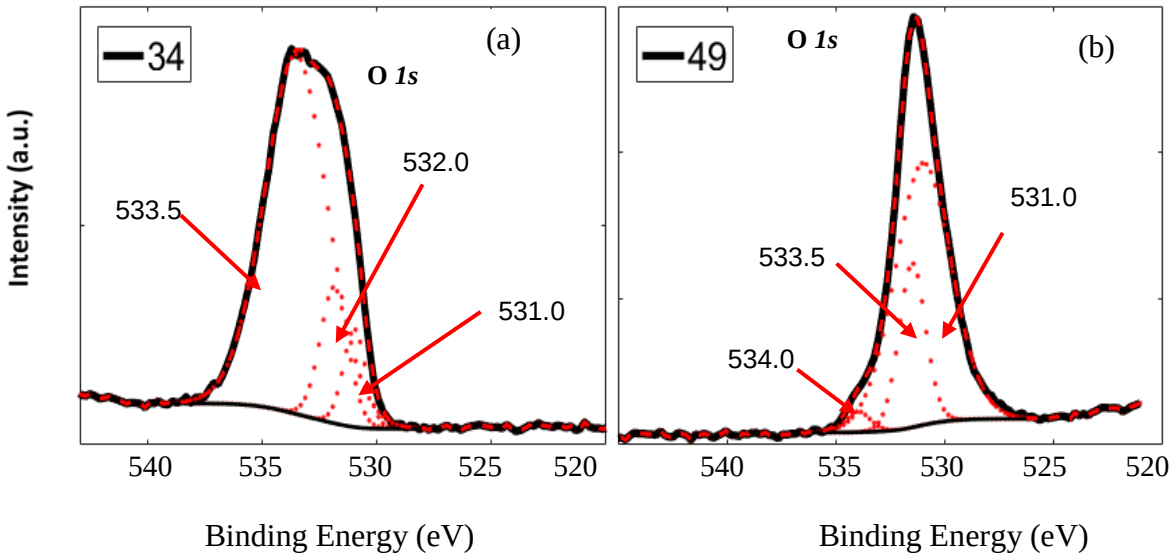


**Figure 28. The O 1*s* binding energies are peak deconvolved for 34 and 49° respectively. The dotted red lines represent the individual deconvoluted peaks, while the red dashed line is the summation of the peak deconvolution. The three O 1*s* peaks are observed at 531.0, 531.9, and 533.5 eV for the 34° spectrum and are observed at 531.0, 533.5, and 534.0 eV for the 49° spectrum.**

The O 1*s* binding energy peaks represent the contributions from water and oxygen adsorption on the $UO_2$ surface [9], which can be determined through peak deconvolution. Figure 28(a) and Figure 28(b) show the peak deconvolution of the O 1*s* at two angles indicating three resolvable peaks at 531.0, 531.9, and 533.5 eV for 34° and at 531.0, 533.5, and 534.0 eV for 49°. In Figure 28(a) and Figure 28(b) the measurements provide an O 1*s* binding energy peak at 533.5, and 532.0 eV, and 534.0 and 533.5 eV respectively, more towards water contamination. Oxygen adsorption on $UO_2$ presents the O1*s* 531.0 eV binding energy peak.

*7.3.3 Binding Energies of O 2p - Valence-Band Region Transitions*

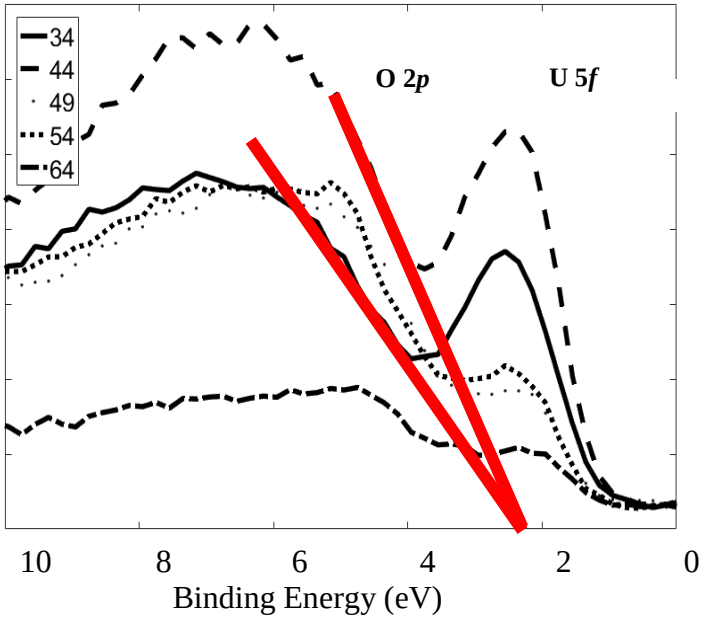


**Figure 29. The AR-XPS spectra for the $UO_2$ valence band edge collected for angles of 34, 44, 49, 54, and 64° between the surface and the x-ray source. An electronic band gap of ~2.2 eV is denoted by red lines.**

Figure 29 presents the O 2*p* and U 5*f* interband binding energies for angles of 34, 44, 49, 54, and 64°. Using the same description as [18] and [7], we refer to the O 2*p* band as the valence band, since is represents the lower energy level for optical transitions. From Figure 29 we find the valence band edge provides an energy band-gap of 2.2 eV, in agreement with the literature value of 2.0 ± 0.1 eV for $UO_2$ [19]. This band gap is attributed to a $5f^2 \rightarrow {}^5f^1 6d$ transition [19].

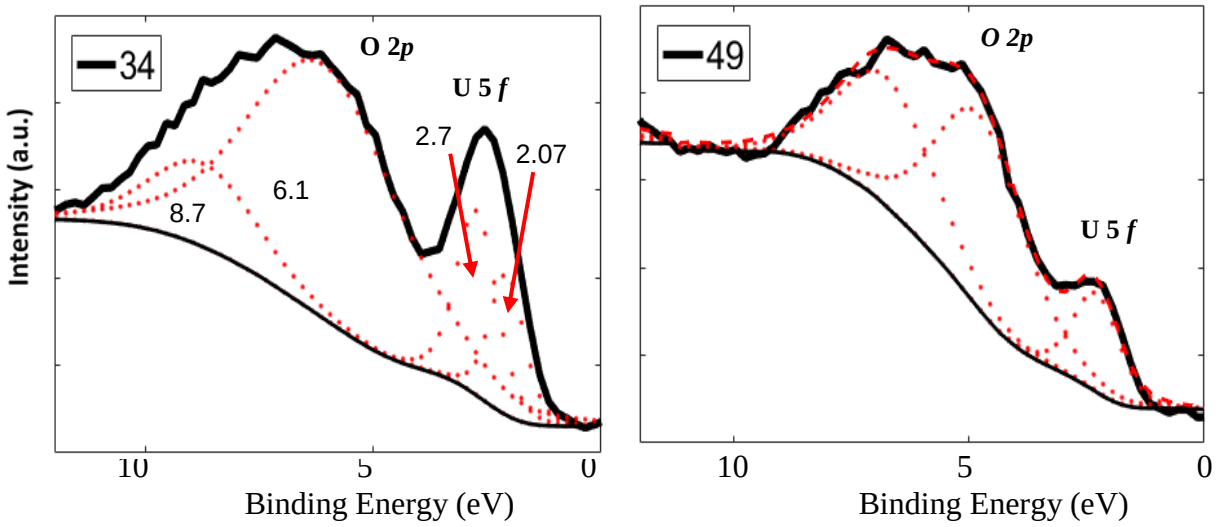


**Figure 30. The O 2*p* and U 5*f* binding energies are peak deconvolved for 34 and 49° respectively. The dotted red lines represent the individual deconvoluted peaks, while the red dashed line is the summation of the peak deconvolution. The 34° spectrum provides evidence of the spin orbit coupled U $5f_{7/2}$ and U $5f_{5/2}$ orbitals while in the 49° spectrum the U *5f* orbitals are indistinguishable.**

Figure 33 presents the O 2*p* and U 5*f* binding energies for angles of 34, 44, 49, 54, and 64°. The O 2*p* sum peaks are wide and range from 4.77 to 8.7 eV. They, however, are broad and cannot be attributed to any known transitions. We show the peak deconvolution of the O 2*p* peak at two angles, 34 and 49° indicating two resolvable peaks. The specific binding energies found by deconvolution are provided in Table 5. The U 5*f* binding energy sum peak at 34° is shown to be a result of two peaks at 2.07 and 2.7eV. These are can be attributed to the spin-orbit coupled U *5f* orbitals as described in [18] and are also provided in Table 5. These U *5f* orbitals are indistinguishable in the 49° spectrum, with a sum peak at 2.49 eV.

**Table 5. The valence band region angle-dependent O 2*p* and U 5*f* peak deconvoluted binding energies [eV] for hydrothermally-grown s.c. $UO_2$.**

| | 34° | 44° | 49° | 54° | 64° |
|---|---|---|---|---|---|
| | | | O 2*p* | | |
| Peak 1 | 8.7 | 7.6 | 6.75 | 7.2 | 6.75 |
| Peak 2 | 6.07 | 5.4 | 4.76 | 4.78 | 4.77 |
| | | | U 5*f* | | |
| Peak 1 | 2.07 | 2.38. | 2.49 | 2.29 | 2.2 |
| Peak $2^+$ | 2.74 | | | | |

## 7.4 Discussion

### *7.4.1 U 4f Binding Energies and Oxidation States*

Table 5 presents the binding energies for the U 4 $f_{7/2}$ and U 4 $f_{5/2}$ at various angles, representing depths of measurements. At all observed angles (except at 49° where the U 4 $f_{5/2}$ could not be deconvolved), both $U^{4+}$ and $U^{6+}$ oxidation states are present. Therefore we conclude a mixture of $UO_2$ and $UO_3$ present for all depths measured. Nornes et al. reported an oxidized uranium metal surface with a U 4$f_{7/2}$ peak at 380.6 eV, while water condensation has a U 4$f_{7/2}$ peak at 381.8 eV [9]. Additionally, Allen et al. reported binding energies of 380.6 and 391.6 eV for the U 4$f_{7/2}$ and U 4$f_{5/2}$ respectively for heated stoichiometric $UO_2$ being exposed to partial pressures of oxygen [10]. Our binding energy measurements are consistent with oxidized $UO_2$, which have higher binding energies than stoichiometric $UO_2$ [10].

The binding energies of the U 4*f* peaks are altered by the addition of oxygen disrupting the crystalline structure. The addition of oxygen to $UO_2$ disturbs the uranium fluorite sub-lattice producing $UO_{2.1}$ and $UO_{2.2}$ [11]. According to [11], the addition of more oxygen creates a mixture of $UO_{(2+x)}$ and $U_4O_{(9-y)}$ increasing the crystal's oxidation state, decreasing ionic size, and decreasing the lattice constants, thus shifting the U 4*f* peaks to a higher binding energy as the oxidation state increases [11]. At $UO_{2.25}$, the oxygen atoms become ordered over a long range to

form $U_4O_9$. With more oxidation, $U_3O_7$ and $U_3O_8$ are formed as more oxygen is added and the binding energies increase [10].

The contributions of the oxidation states provides an indication of the stoichiometry of the surface as a function of depth, via the relative counts under each energy peak. A comparison of the peak areas as a percentage of the total sum peaks is provided in Table 6.

**Table 6. Theoretically computed atomic percent ratios for the surface depth profiling of hydrothermally-grown s.c. $UO_2$ by a comparison of the U $4f_{7/2}$ and U $4f_{5/2}$ binding energies.**

$UO_2$ oxidation states surface-depth profiling

| | 34° | 44° | 49° | 54° | 64° |
|---|---|---|---|---|---|
| | | | U $4f_{7/2}$ | | |
| $U^{4+}$ | 53 ± 6% | 31 ± 3% | 44± 6% | 77± 10% | 91± 23% |
| $U^{6+}$ | 47 ± 5% | 69 ± 6% | 56 ± 7% | 23 ± 4% | 9± 5% |
| | | | U $4f_{5/2}$ | | |
| $U^{4+}$ | 53 ± 7% | 31 ± 4% | ** | 77 ± 12% | 91 ± 26% |
| $U^{6+}$ | 47 ± 6% | 69 ± 6% | ** | 33 ± 5% | 9 ± 5% |

**Could not be resolved due to low counting statistics.

In uranyl compounds, the chemical shifts of the ionization energies are due to Madelung potentials, varying fractional atomic charges, and mostly a large contribution from the relaxation of the electronic densities of the other orbitals [14]. Consequently, the chemical shifts in the U $4f_{7/2}$ and U $4f_{5/2}$ peaks are directly related to the oxidation state of uranium. The $UO_2$ binding energy decreases as the oxidation state is decreased from $6^+$ to $4^+$ [15]. The theoretically computed atomic ratios provide a mixture of both $U^{6+}$ and $U^{4+}$ oxide states inferring the photoelectrons, with an escape depth in $UO_2$ of less 50Å, have not penetrated to the $UO_2$ bulk. However, agreeing with theory, there is an increase in the +4 oxidation state of uranium as the photoelectrons penetrate deeper into the selvedge region as shown from 44 to 64°.

The higher $U^{4+}$ concentration at the surface is likely an artifact of our experimental technique that uses an ultra-high vacuum system and thereby removes oxygen from the $UO_2$ surface. Therefore the surface sensitive measurements are oxygen reduced.

Another method of determining a $UO_2$ crystal's oxidation state, is to compare the binding energy of the U 4f shake-up satellite peak to its sum peak. $UO_2$ shake-up satellite peaks arise from the excitation of an electron from the O 2*p*-U bonding level to the partially occupied or unoccupied localized 5*f* levels during the U 4*f* core ionization. Reorganization of the metal U 5*f* electron level, such as with mixed valence or interstitial oxides, changes the number, shape, intensity and position of the U 4*f* satellites [12]. Figure 26 presents the U $f_{7/2}$ shakeup satellite peaks at 387.8 and 382.5 eV for 34 and 49° respectively. In Figure 26(a) the 34° U $4f_{5/2}$ shake-up satellite peaks are present at 401.7, 405.9, and 407.8 eV, higher in binding energy than the sum U $4f_{5/2}$ peak. In Figure 26(b), the 49° U $4f_{5/2}$ satellite peak is are shown at 401.36 eV higher in binding energy than the sum U $4f_{5/2}$ peak and are unobservable at higher emission angles with less intense spectra.

According to [16] the satellite peak shift location is based upon the uranium oxidation state, which we do not know *a priori*. According to Nornes et al., the U $4f_{7/2}$ has binding energies of 380.8 and 382.4 eV for the $U^{4+}$ and $U^{6+}$ respectively. Again in [11] the U $4f_{5/2}$ binding energies of approximately 390.0 and 392.6 eV for the $U^{4+}$ and $U^{6+}$. Figure 26(a) and Figure 26(b) present the U $4f_{7/2}$ binding energies of at 380.2 and 382.4 eV for the $U^{4+}$ and $U^{6+}$ respectively. Figure 26(a) and Figure 26(b) present the U $4f_{5/2}$ binding energies at 380.2 and 382.4 eV for the $U^{4+}$ and $U^{6+}$ respectively. We compare the binding energy of our shake- up satellite peaks to binding energies for the $U^{4+}$ and $U^{6+}$ oxidation states in [16] for both U $4f_{7/2}$ and U $4f_{5/2}$ energy peaks. At 34°, the U $4f_{7/2}$ satellite peak at 387.82 eV is consistent with [16] for $UO_2$. At 34°, the U $4f_{5/2}$ satellite peak at 387.82 eV is consistent with [16] for $UO_{2+x}$, and resembles measurements between $UO_{2.68}$ and $UO_{3.0}$. At 49°, the U $4f_{72}$ satellite peak at 382.84 eV is 2.01 eV from the 4+ oxidation state peak and 0.44 eV from the $6^+$ oxidation state

peak and inconclusive due to few peak deconvolutions of the same satellite peak in [16]. Again, at 49°, the U $4f_{5/2}$ satellite peak at 399.62 eV is 8.72 eV from the 4+ oxidation state peak and 7.02 eV from the 6+ oxidation state peak, and consistent with [16] for $UO_{2.68}$. At 34 and 49°, the satellite peaks confirm the mixed oxidation states presented in Table 4. Still, the largest challenge in utilizing the shake-up satellite peaks to confirm the $UO_2$ oxidation state is utilizing the correct U 4*f* binding energies for stoichiometric $UO_2$. Allen et al. presents U $4f_{7/2}$ binding energies for $UO_{2.0}$ ranging from 380.0 to 380.3 eV, while the U $4f_{7/2}$ binding energies for $UO_{2.1}$ presents a binding energy of 381.6 eV [10].

*7.4.2 Binding Energy of O 1s.*

Without fine splitting or multiple oxidation states, the O 1*s* spectra should present a single-binding energy peak. Multiple oxygen peaks reveal water or oxygen on the surface. In comparison, Nornes et al. studied water adsorption on elemental uranium, and identify three O 1*s* photoelectron peaks for water adsorbed on uranium in addition to the peak energy for the adsorption of oxygen. The presence of O 1*s* peaks at 535.8, 533.5, and 532.0 eV are associated with $H_2O$ adsorption on uranium with the 535.8 peak not appearing above 200 K. [9] A binding energy peak of 531.4 eV is associated with oxygen adsorption.

Figure 32(a) and Figure 32(b) provide a 3-peak deconvolution of the O 1*s* peak for both 34 and 49°. At 34 and 49°, the normalized oxygen fraction (%) on the surface is 8% and 3% respectively, indication a low and decreasing surface oxygen concentration. In [9], a peak of 533.5 eV is representative of oxygen in an OH complex, or surface water. Again, at 34 and 49°, the normalized percent water fraction on the surface is 79% and 22% respectively indicating a decreasing surface water concentration. Therefore, there could be the presence of a uranium

hydrate on the surface, but more likely it would be a $UO_2$ hydrate since the published O 1*s* sum peak binding energies for $UO_2$ to $UO_3$ range from 530.4 to 528.9 eV [7], and our sum peak values are shown in Figure 27 at 533.3, 533.1, 533.6, 533.4, and 533.4 eV for angles 34, 44, 49. 54 and 64° respectively.

### *7.4.3 Valence Band Region*

The slope of the O 2*p* band provides the $UO_2$ band gap and an insight into the $UO_2$ crystal oxidation state. According to Figure 29, the band gap of the $UO_2$ crystal at multiple angles is 2.2 eV, whereas the stoichiometric $UO_2$ band gap is 2.0 eV. As the measurement probes further into the selvedge region a small shift in band gap is another verification of the mixed oxide crystal structure and proof we have not penetrated the selvedge region to $UO_2$.

In addition to providing the electronic band gap of $UO_2$, the valence band region also informs the $UO_2$ oxidation state. $UO_2$ is a known Mott insulator with a U 5*f* interband. All spectra in Figure 29 and Figure 33 verify the presence of U 5*f* electrons at 2.5 eV. At 34° the higher concentration of $UO_2$, as shown in Table 4, and the high intensity peak resolution are present with both the U $5f_{7/2}$ and U $5f_{5/2}$ peaks. At 49° only one U 5*f* peak is present as the concentration of the $U^{6+}$ oxidation state is greater than the concentration of the $U^{4+}$ oxidation state, as shown in Table 4.

Oxidation states can be determined by the intensity of the U 5*f* interband with stoichiometric ratios dependent on the oxygen-to-uranium ratio. With stoichiometric $UO_2$, the two 5*f* electrons are localized on the U center with a high photoexcitation cross-section for Al Kα radiation. The localized 5*f* electrons are lost from the center U into bonding or antibonding orbitals for interstitial oxides from $UO_{2+x}$ to $UO_3$ [12]. Since the O 2*p*-U bonding does not

change for the different U/O ratios, the 5*f* electrons have a minimal contribution to covalent bonding and the 5*f* character is lost when these electrons are transferred into covalent bonding states [12]. Hence, the presence of U 5 *f* peaks in the valence band spectra provides evidence of the $U^{4+}$ oxidation state but does not refute the presence of the $U^{6+}$ oxidation state.

Published values for the binding energy of the $UO_2$ 5*f* electrons are 1.5 eV [20]. The U 5*f* emission cross-section is strongly energy-dependent. Arko et al. present angle-resolved XPS of the $UO_2$ valence band edge and illustrate the energy dependence of the U 5*f* binding energy. The U 5*f* binding energy increases as the incident photon energy increases from 14 to 30 eV [20]. The U 5*f* electrons presented in Figure 33 are shifted higher in binding energy since the incident energy was two-fold greater at 1486.6 eV.

**7.5 Conclusion**

An investigation of a rough polished hydrothermally grown s.c.$UO_2$ surface has been conducted using AR-XPS and compared with oxidized uranium metal, $UO_2$, and other oxides. An oxidized $UO_2$ surface is confirmed with an increase in the binding energies of the U 4*f* peaks. Peak deconvolution of the U $4f_{7/2}$ peak provides evidence of $U^{4+}$ and $U^{6+}$ oxidation states. An increase in the concentration of the $U^{4+}$ oxidation state confirmed we have not probed through the $UO_2$ surface and selvedge regions to stoichiometric $UO_2$. Analysis of the U 4*f* shake-up satellite peaks indicates a smaller oxygen concentration on the $UO_2$ surface likely due to surface oxygen reduction during latent time at ultra-high vacuum. The shifting of the U $4f_{7/2}$ peak energy and the peak convolution of the O 1*s* peak reaffirms the presence of surface water, which decreases with depth, as expected. The presence of U 5*f* peaks in the valence band spectra provides evidence of the $U^{4+}$ oxidation state but does not refute the presence of the $U^{6+}$ oxidation state. The electronic band-gap energy of 2.2 eV confirms the presence of $UO_2$. Possible

explanations to our AR-PES data are a new oxide growth on the surface of the $UO_2$ crystal or excess oxygen incorporated into the interstitial sites in the lattice to form a $UO_{2+x}$ surface. Even with the presence of surface $H_2O$ and $O_2$, the $UO_2$ surface and selvedge region of the $UO_2$ still retains the primary band gap for stoichiometric $UO_2$.

### 7.6 References


[1] Taylor, P., McEachern, R., Sunder, S., Wasywich, W., Miller, N., and Wood, D. "Recent Findings on the Oxidation of $UO_2$ Fuel under Nominally Dry Storage Conditions," *AECL-11447*, vol. 33-27, pp.1-13, 1995.

[2] McEachern, R., and Talyor, P. "A Review of the Oxidation of Uranium Dioxide at Temperatures below 400°C," *AECL-11335*, pp. 1-75, 1997.

[3] Blackburn, P., Weissbart, J., Gulbransen, E. "Oxidation of Uranium Dioxide," *Journal of Physical Chemistry*, vol. 62, pp. 902 – 908, 1958.

[4] Fuggle, C., Burr, A., Watson, L., Fabiran, D., and Lang, W. "X-ray Photoelectron Studies of Thorium and Uranium,"*Journal of Physics F: Metal Physics*, vol. 4, pp. 335-342, 1974.

[5] Allen, G., Crofts, C., Curtis, M., Tucker, P., Chadwich, D., and Hampson, P. "X-ray Photoelectron Spectroscopy of Some Uranium Oxide Phases," *Journal Chemical Society Dalton Trans*actions, vol., pp. 1296-1301, 1974.

[6] Arko, A., and Koelling. "The Band Structure of $UO_2$: An Angle Resolved and Resonant Photoemission Study," *Journal of Less-Common Metals*, vol. 122 pp. 95-99, 1965.

[7] Nornes, S., Mesisenheimer, R., "X-ray Photoelectron Spectroscopy Study of the Chemisorption of Water on Uranium and Thorium and Oxygen and Uranium," *Surface Science*, vol. 88, pp. 191-203, 1979.

[8] Allen, G., Tucker, P., Tyler, J. "Oxidation of Uranium at 298 K Studied by Using X-ray Photoelectron Spectroscopy," *Journal of Physical Chemistry*, 86 (1982) 224-228.

[9] Allen, G., Trickle, I., and Tucker, P. "Surface Characterization of Uranium Metal and Uranium Dioxide using X- ray Photoelectron Spectroscopy," *Philosophical Magazine B*, vol. 43-4, pp. 689-703, 1981.

[10] Young, C., Petrosky, J., Mann, J., Hunt, E. Turner, D., Dowben, P. "The Lattice Stiffening Transition in $UO_2$ Single Crystals," *Journal of Physics: Condensed Matter* 29-3 (2016), 035005.

[11] Ilton, E., Boily, J. Bagus, P. “Beam Induced Reduction of U(VI) during X-ray Photoelectron Spectroscopy. The Utility of the U4f Satellite Structure for Identifying Uranium Oxidation States in Mixed Valence Uranium Oxides,” *Surface Science* vol. 601, pp. 908-916, 2007.

[12] Keller, C., and Jorgensen, C. “Photoelectron Spectra of Uranium (V) in Mixed Oxides Showing Characteristic Satellite Signals,” *Chemical Physics Letters* vol. 32-3, pp. 397-400, 1975.

[13] Bera, S., Sali, S., Sampath, S., Narasimhan, S., and Venugopal, V. “Oxidation State of Uranium: an XPS Study of Alkali and Alkaline Earth Uranates,” *Journal of Nuclear Materials*, vol. 255 pp. 26-33, 1998.

[14] Anthonysamy S., Panneerselvam G., Santanu Bera S., Narasimhan S., P.R. Vasudeva Rao. “Studies on Thermal Expansion and XPS of Urania ± Thoria Solid Solutions,” *Journal of Nuclear Materials* vol. 281, pp. 15-21., 2000.

[15] Teterin, Yu A, et al. “A Study of Synthetic and Natural Uranium Oxides by X-ray Photoelectron Spectroscopy,” *Physics and Chemistry of Minerals* vol. 7-4, pp. 151 – 158, 1981.

[16] Pireaux, J., Thibaut, J., Tenret-Noel, C., Caudano, R., and Verbist, J. “Shake-up Satellites in the X-ray Photoelectron Spectra of Uranium Oxides and Fluorides. A Band Structure Scheme for Uranium Dioxide, $UO_2$,” *Chemical Physics* vol. 22, pp.113-120, 1977.

[17] Schoenes, J. “Optical Properties and Electronic Structure of $UO_2$,” *Journal of Applied Physics*, vol. 49, pp.1463-1465 (1978).

[18] Arko, A., and Doelling, D. “The Band Structure of $UO_2$: An Angle Resolved and Resonant Photoemission Study,” *Journal of the Less-Common Metals*, vol. 122, pp. 95-99, 1986.

[19] Veal, B., and Lam D. “X-ray Photoelectron Studies of Thorium, Uranium, and their Dioxides,” *Physical Review B*, vol. 10-12, pp. 4903-4908, 1974.

## VIII. Near-Infrared to Vacuum Ultraviolet Dielectric Functions and Critical Points of Single Crystal Thoria Compared to Urania

This section is directly derived from a paper being prepared for submission to Physica Solidi Rapid Review Letters. It was modified to be consistent with the dissertation format. The collaborating authors are C. Dugan, A. Mock, S. Knight, R. Korlacki, L. Wang, K. Zhang., J. M. Mann, E. Hunt, W. Mei, M. Schubert, P. Dowben, and J. Petrosky. The journal article is titled, "Near-Infrared to Vacuum Ultraviolet Dielectric Functions and Critical Points of Single Crystal Thoria Compared to Urania."

The AR-XPS confirmed the presence of both $UO_2$ and $UO_3$ on the crystal's surface with a higher concentration of $UO_2$ deeper into the crystal. Ellipsometry measurements were taken to confirm the $UO_2$ crystal quality. A comparison can be made with DFT calculations, which was accomplished by my collaborators.

Cathodoluminescence spectroscopy verified the energy for both the DFT and ellipsometric calculations merging experimental technique and theoretical calculations, producing a verified dielectric function.

### 8.1 Introduction

The electronic properties of actinide dioxides, from $UO_2$ to $AmO_2$, must include the localized 5*f* electronic states whose strong on-site Coulombic repulsion interaction is often severely underestimated in density functional theory (DFT) calculations [1-6]. An accurate quantitative description of the optical spectra requires theory beyond the independent particle picture, yet qualitative agreement between theory and experiment can often be obtained at the level of DFT [7]. While the optical adsorption and reflectance spectra of semiconductors have

been studied for several decades, similar work on actinide oxides has been hampered by the absence of high quality single crystals [8, 9].

Experimentally, Schoenes studied the incident light reflectivity from $UO_2$ single crystals in the photon energy range of 0.03–13 eV from which the complex dielectric function $\varepsilon(\omega) = \varepsilon_1(\omega) + i\varepsilon_2(\omega)$ has been derived [10]. This effort to extract the complex dielectric function has been repeated more recently by Siekhausand J. Crowhurst [11] as well as Dugan and coworkers [12], which resulted in significant shifts when compared to reflectivity measurements as determined by Schoenes [10]. Reflection from $UO_2$ thin films by optical transmission has also been measured [13], while the optical properties for both $ThO_2$ and $UO_2$ have been previously calculated [14] using the Heyd-Scuseria-Ernzerhof (HSE) functional. The challenges of growing single-crystal $UO_2$ have been addressed with the fabrication of high-quality, single crystal actinide oxide samples using a hydrothermal synthesis growth technique [12, 14, 15]. This growth process has produced bulk single crystals of near-stoichiometric $UO_2$ [12, 16-18] and $ThO_2$ [15, 16, 19]. These improved single crystals open the door to a much better assessment of the optical and semiconductor properties, not previously possible.

**8.2 Experiment**

Single crystals of $ThO_2$ and $UO_2$ were grown by hydrothermal synthesis [12, 15, 18-19]. The $ThO_2$ single crystals were prepared by the hydrothermal technique in a supercritical cesium fluoride mineralizer solution. Due to the corrosive nature of the mineralizer solution, the reaction was performed in a sealed silver ampoule (Stern Leach, 99.99%) with an inner diameter of 3/8 in and an overall length of 8 in. Thorium oxide (Strem, 99.99%) powder weighing 1.3 g and 4 mL of 6 M CsF (Alfa Aesar, 99.99%) were added to the silver ampoule, which was then welded shut. The ampoule was placed in a 27 mL inconel autoclave with excess water added to the remaining

volume of the vessel. This excess water acts as counter pressure to prevent the ampoule from rupturing during the growth cycle. Once the autoclave was sealed, two band heaters were applied with a top and bottom temperature of 963 and 1023 K respectively. The result is 20 kpsi of pressure on the ampoule. The applied conditions were sufficient to spontaneously nucleate single crystals of $ThO_2$ from a supersaturated mineralizer solution. Crystal formation occurred over an 11 day growth period, at which time the autoclave was allowed to cool to room temperature. Further growth information is detailed in [20].

The $UO_2$ crystals were grown using a nutrient/feedstock of high-purity, depleted uranium dioxide powder (99.998% $UO_2$, International Bioanalytical Laboratories, Lot# B206093). A 6M cesium fluoride mineralizer solution (99.9% CsF, Alfa Aesar, Lot# S25A038) was utilized to aid dissolution of the nutrient and transport it to the colder crystallization zone of the reaction vessel. The temperatures of the feedstock and crystallization zones were held at 923 and 873 K, respectively for 45 days at a pressure of 25 kpsi. The feedstock, mineralizer and seed crystals were loaded into an inert sealed silver ampule (99.95% Ag, Refining Systems, Inc.) and then welded shut. $CaF_2$ seeds with (111) orientation provided a template for oriented growth of 0.10 mm $UO_2$ on the substrate. Orientation and crystalline structure was confirmed by single-crystal X-ray diffraction. The $UO_2$ crystals grown under these conditions have measured lattice parameters of 5.4703 ± 0.0006 Å indicating a stoichiometry near $UO_{2.003}$ [21, 22].

The ellipsometric data was collected in the spectral range 0.75-6.4 eV with a dual rotating compensator ellipsometer (RC2, J.A. Woollam Co., Inc.) and from 5-9.4 eV with a nitrogen purged rotating analyzer ellipsometer (VUV, J.A. Woollam Co., Inc.). Measurements were taken at 5, 55, 65, and 75° angles of incidence. Data was analyzed using WVASE32 (J.A. Woollam Co., Inc.).

The cathodoluminescence system uses a Kimball Physics EMG-12 electron gun powered by an EGPS-12 power supply, a vacuum system, a sample chamber with suitable optical ports, an optical system, a spectrometer, and a photomultiplier detector. The liquid nitrogen-cooled $UO_2$ was placed at the focal point of the electron gun and the resulting cathodoluminescence signal from the sample was transmitted through the quartz window of the vacuum chamber, focused onto the entrance slit of the monochromator and then to the photomultiplier. The electron beam was incident at an angle of approximately 45° with 10 keV energy.

**8.3 Theory**

For this spectroscopic ellipsometric investigation, an isotropic analysis is performed with a substrate-ambient boundary condition approximation where the single crystalline actinides correspond to half-infinite substrates. Nanometer scale finite roughness effects must be accounted for when investigating polished single crystals. Here we utilize an effective medium approximation (EMA) to render the effects of a layer with thickness much smaller than the wavelengths used in the analysis procedure [23]. In this work we calculated this effective medium approximation layer by averaging the optical properties of the actinide layer with void assuming a 50:50 ratio. A wavelength-by-wavelength regression analysis is utilized where the only unknown parameters are the real and imaginary parts of the substrate dielectric function.

Critical point (CP) features, observed in the dielectric function spectra caused by transitions in the electronic band-to-band structure, can be conveniently modeled using Gaussian line shapes with a Kramers-Kronig transformation [24]. Electronic band-to-band transitions cause critical point (CP) features in the dielectric function spectra. The imaginary part, $\varepsilon_2$, can be modeled conveniently using Gaussian functions as:

$$\varepsilon_2(E) = A\left(e^{-\left(\frac{E-E_n}{\sigma}\right)^2} - e^{-\left(\frac{E+E_n}{\sigma}\right)^2}\right) \tag{8.1}$$

$$\sigma = \frac{B_r}{2\sqrt{\ln(2)}}, \tag{8.2}$$

with best-match parameters of amplitude $A$, center energy $E_n$, and broadening $B_r$ [24]. The real part, $\varepsilon_1$, is obtained from Kramers-Kronig transformation such that

$$\varepsilon_1(E) = \frac{2}{\pi} P \int_0^\infty \frac{\xi \varepsilon_2(\xi)}{\xi^2 - E^2} d\xi, \tag{8.3}$$

where $P$ is the principal value of the integral and $\omega$ is the angular frequency.

All the electronic band structure calculations were performed within the framework of spin-polarized plane-wave density functional theory (PW-DFT), implemented in the Vienna ab initio simulation package (VASP). [25, 26] The Perdew–Burke–Ernzerhof (PBE) functional and projector augmented wave (PAW) potentials were used [27-29]. An energy cutoff of 600 eV was adopted for the plane-wave expansion of the electronic wave function. Geometry structures are relaxed until the force on each atom is less than 0.01 eV/Å and the energy convergence criteria of $10^{-7}$ eV are met. Once the optimized structures were achieved, the hybrid functional, in the Heyd-Scuseria-Ernzerhof (HSE06) [30] form, was used to determine more accurate band gaps. The imaginary part of the frequency-dependent dielectric matrix was calculated based on the HSE06 ground states of $ThO_2$ by using the random phase approximation (RPA) [30, 31].

## 8.4 Results

### *8.4.1 The complex dielectric function of $ThO_2$ and $UO_2$:*

Figure 34 has the real ($\varepsilon_1(\omega)$) and imaginary ($\varepsilon_2(\omega)$) parts of the dielectric function for single crystalline $ThO_2$, extracted from the VASE by the wavelength-by-wavelength analysis approach, with critical point analysis. Again, the individual component oscillators are provided

in the imaginary part by the vertical lines correspond to the center energies of each. Oscillator parameters, determined during the critical point analysis are given in Table 7. The VASE measurements made at several azimuthal orientations tends to verify that the sample is isotropic. There was no significant evidence of anisotropy in the VASE data. The extinction of the imaginary dielectric constant, $\varepsilon_2(\omega)$, part of the dielectric function is gradual, thereby suggesting the $ThO_2$ crystal contains some heterogeneous defects. But as with VASE obtained for $UO_2$, shown in Figure 35, the extinction goes to zero at the lowest photon energies and is indicative of a superior crystal with few defects.

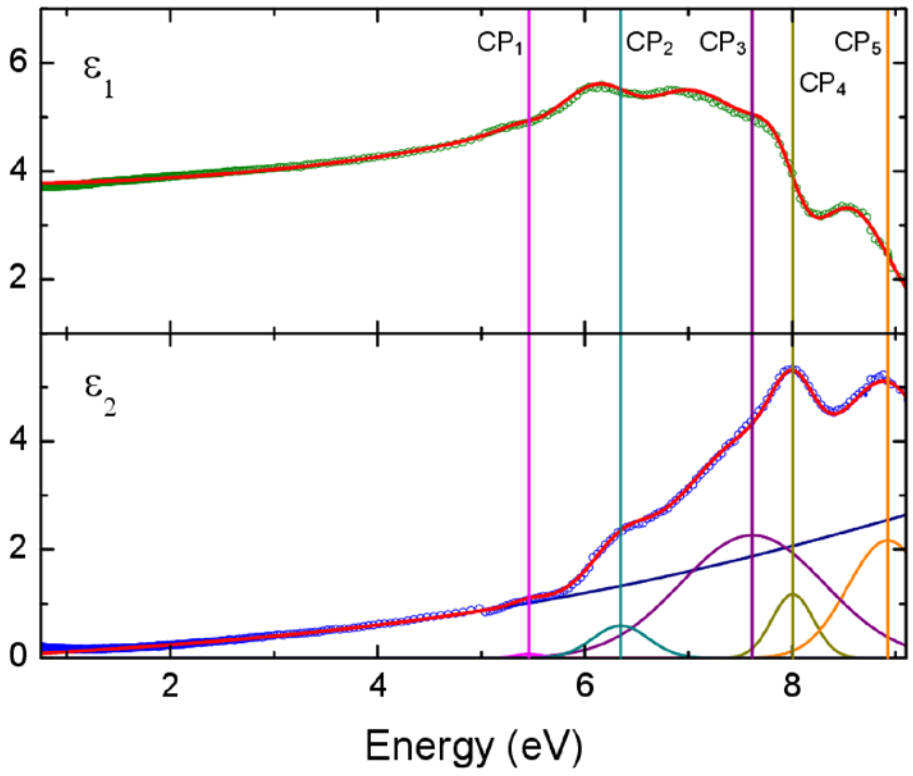


**Figure 31. The real and imaginary parts of the $ThO_2$ dielectric function, extracted from the variable angle spectroscopic ellipsometry by wavelength-by-wavelength analysis (green and blue circles, respectively), shown in comparison with the critical point model dielectric function (red solid). Individual contributions to the imaginary part of the dielectric function obtained with Gaussian oscillators are shown with vertical lines corresponding to their center energies ($CP_1$-magenta, $CP_2$-dark cyan, $CP_3$-violet, $CP_4$-dark yellow, $CP_5$-orange, as well as another contribution outside the investigated spectral range to account for higher energy transitions shown as navy).**

**Table 7. Critical point parameters determined from the VASE model dielectric function analysis, amplitude (A), energy (E) and broadening (Br) for $ThO_2$ in comparison with band-to-band transition energies determined from DFT calculation. Digits in parenthesis indicate 90% confidence from model analysis. A higher energy transition outside the investigated range is also used to account for higher energy transitions.**

| Feature | VASE Critical point transitions | | | | Assignment |
|---|---|---|---|---|---|
| | A (eV) | [1]E (eV) | Br (eV) | [2]E (eV) | |
| $CP_1$ | 0.07(2) | 5.4(6) | 0.3(3) | 6.12 | Th $6d \rightarrow$ O $2p$ |
| $CP_2$ | 0.6(0) | 6.3(5) | 0.6(3) | 7.2 | Th $6d \rightarrow$ O $2p$ |
| $CP_3$ | 2.2(6) | 7.6(2) | 1.6(3) | 7.7 | Th $6d/5f \rightarrow$ O $2p$ |
| $CP_4$ | 1.1(8) | 8.0(1) | 0.47(3) | 9.0 | Th $5f \rightarrow$ O $2p$ |
| $CP_5$ | 2.1(7) | 8.9(2) | 0.9(1) | | |

1. Experimentally determined energy values

2. HSE theoretically determined energy values.

Figure 35 displays the real ($\varepsilon_1(\omega)$) and imaginary ($\varepsilon_2(\omega)$) parts of the dielectric function of the single crystal $UO_2$, also extracted from VASE by the wavelength-by-wavelength analysis approach, with critical points analysis. Individual contributions, corresponding to electronic interband transitions are shown in the imaginary part ($\varepsilon_2(\omega)$) of the dielectric function, with vertical lines corresponding to the spectra weight center of the transition. The critical point values for the single crystalline $UO_2$ are given in Table 7. The experimentally determined band gap of 2.1 eV found here, from VASE, is consistent with the theoretically predicted band gap of 2.19 [12], 2 [32], and 2.03 eV [3] as well as prior experimental measurements [10]. Density function theory on the other hand is notorious for under estimating the band gap, and in the case of $UO_2$, the estimated band gaps typically range from 1.3 [34] to 1.9 eV [35, 36], although unlike [12], many HSE calculations come out with a much larger band gap than expected ranging from 2.39 [37] to 2.76 eV [38]. For $ThO_2$, DFT has produced band gaps as low as 3.3 [39] and 4.7 eV [40].

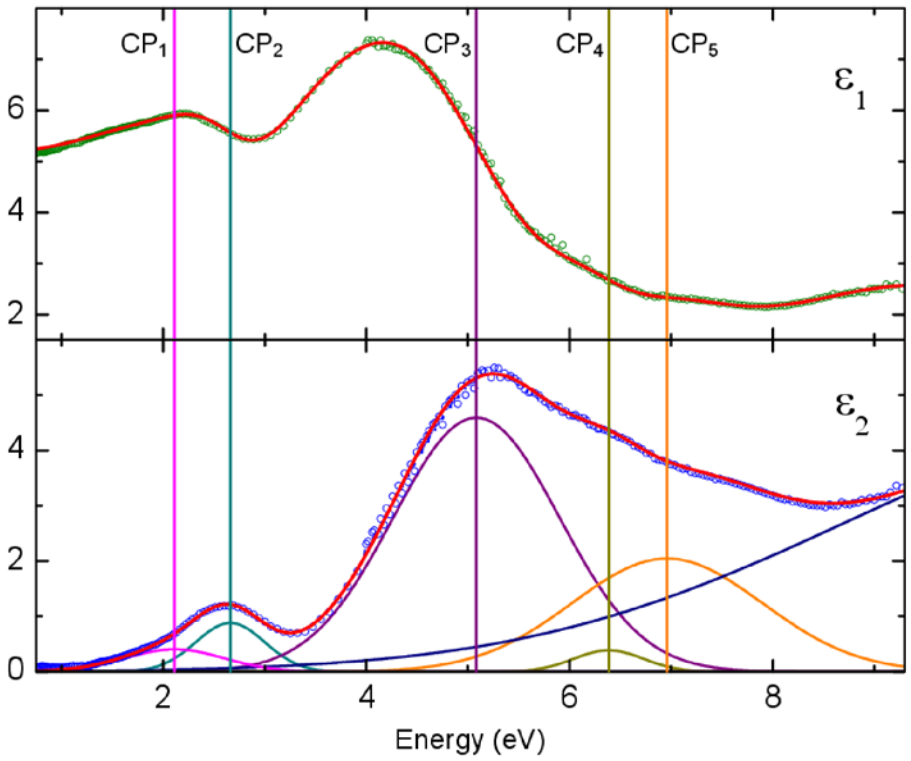


**Figure 32. The real and imaginary parts of the $UO_2$ dielectric function extracted from the variable angle spectroscopic ellipsometry by wavelength-by-wavelength analysis (green and blue circles, respectively) shown in comparison with the critical point model dielectric function (red solid). Individual contributions to the imaginary part of the dielectric function obtained with Gaussian oscillators are shown with vertical lines corresponding to their center energies ($CP_1$-magenta, $CP_2$-dark cyan, $CP_3$-violet, $CP_4$-dark yellow, $CP_5$-orange, as well as another contribution outside the investigated spectral range to account for higher energy transitions shown as navy).**

Figure 33 displays the cathodoluminescence, collected at 10 keV, for the single crystal $UO_2$. The values given in Table 8 generally agree with the optical transition values extracted from VASE. The experimentally determined band gap of 2.37 eV, from cathodoluminescence, is also consistent with the theoretically predicted band gap of 2.19 eV [12]. This value of 2.37 eV is larger than found by VASE (Table 7). Since there is no initial state photo-hole, the luminescence corresponding to transition from the lowest unoccupied state to highest occupied state is expected to result in a larger measured band gap using CL versus VASE. The very low luminescence for

the transitions corresponding to the band gap is the result of it being a selection rule forbidden transition, as will be discussed later.

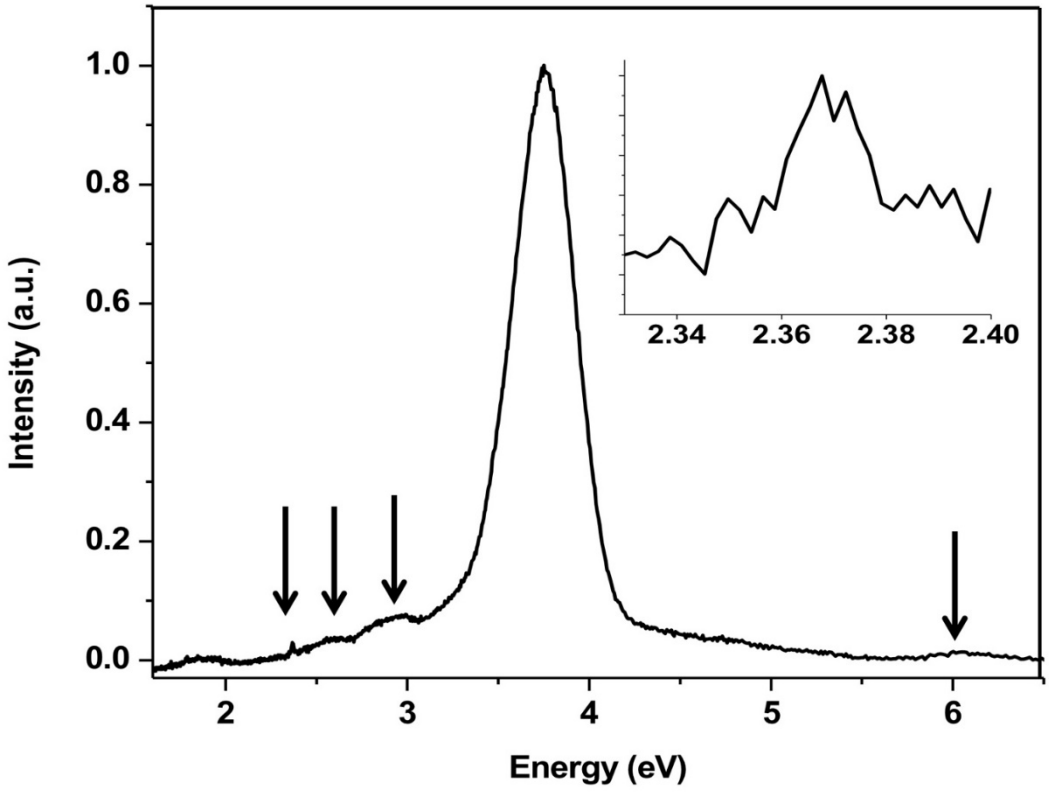


**Figure 33. The optical transitions for single crystal $UO_2$, measured from CL. The incident electron energy is 10 keV to avoid surface effects. The weaker transitions are indicated by arrows, and the transition corresponding the lowest unoccupied state to highest occupied state transition is shown in the inset.**

**Table 8. Critical point analysis parameters of amplitude (A), energy (E) and broadening (Br) for $UO_2$, obtained from VASE. Digits in parenthesis indicate 90% confidence from model analysis. A higher energy transition outside the investigated range is also used to account for higher energy transitions.**

| Feature | VASE Critical point transitions | | | Theory | [3]CL | Assignment |
|---|---|---|---|---|---|---|
| | A (eV) | [1]E (eV) | Br (eV) | [2]HSE | [3]E(eV) | |
| $CP_1$ | 0.4(0) | 2.1(1) | 1.(1) | 2.19 | 2.36 | $U5f \rightarrow U5f$ |
| $CP_2$ | 0.(8) | 2.6(6) | 0.8(0) | - | 2.6, 2.9 | $U5f \rightarrow U5f$ |
| | | 4.2(1) | | 3.6 | 3.76 | $U5f \rightarrow U6d$ |
| $CP_3$ | 4.5(9) | 5.0(8) | 1.9(3) | 4.5 | - | $U5f \rightarrow U6d$ |
| $CP_4$ | 0.3(9) | 6.3(9) | 0.8(1) | 6.0 | 6.1 | $O\ 2p \rightarrow U6d/5f$ |
| $CP_5$ | 2.0(4) | 6.9(6) | 2.2(1) | 7.0 | 6.8 | $O\ 2p \rightarrow U6d/5f$ |

[1]Experimentally determined energy values from VASE
[2]HSE theoretically determined energy values.
[3]Experimentally determined energy values from CL

### *8.4.2 Interband transitions of $ThO_2$ and $UO_2$*

When the DFT+*U* method was used, with a choice of $U$ = 2 eV for *f*-states of Th atoms to provide the necessary correction for the on-site Coulomb interactions, the calculated band gap is 5.04 eV. Using the Heyd-Scuseria-Ernzerhof functional, to estimate a more accurate band gap, our calculation revealed that the ground states of bulk $ThO_2$ are nonmagnetic, with a band gap of 6.12 eV, as shown in Figure 34. This is close to the 6.21 eV previously calculated [30]. However, it has been shown that the Heyd-Scuseria-Ernzerhof band structure calculation, with spin-orbit coupling turned on, provides a band gap of 5.8 eV [30], which is closer to the experimental value of 5.75 eV [31] and our value of 5.4 eV measured from variable angle ellipsometry. The Heyd-Scuseria-Ernzerhof functional does, however, differ significantly from the calculated band structure obtained using Perdew, Burke, Ernzerhof (PBE) and the band structures previously reported [30, 32, 39].

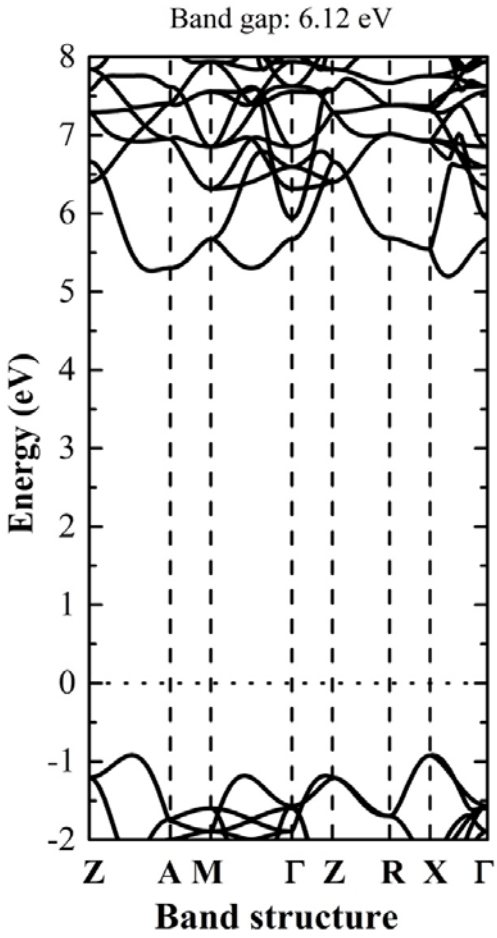


**Figure 34. The band structure of bulk $ThO_2$ using Heyd-Scuseria-Ernzerhof (HSE) hybrid functional. The band gap is 6.12 eV and the ground state is anti-ferromagnetic.**

These band gap calculations do not represent the signature of surface effects. Density functional theory slab calculations indicates that $ThO_2$ (001), with a Th atom termination, is not a spin polarized semiconductor, and in this approach, we are left with the suggestion that the band gap is small, of order 0.28 eV. $ThO_2$ (100), with an O atom, termination ferromagnetic metal with the magnetic moments of the supercell 4.0 $\mu_B$. Basically, by including the surface, the $ThO_2$ (001) band structure is characteristic of a semimetal. The semimetal band gap is an indirect gap

of about 2.7 eV, and in any case, the predicted semimetal behavior of the surface is not what has been measured here.

The Perdew, Burke, Ernzerhof (PBE) calculated $ThO_2$ band structure, with a correlation U, as in Figure 35, is qualitatively similar to that calculated through B3LYP functional [32] and the relativistic linear augmented-plane-wave (RLAPW) calculation of [39], for the valence band but differs significantly from this previously calculated band structure on the conduction band side. One difference with the calculated band structure of [32, 39] in that the calculation of Figure 35 has the conduction band minimum at the L point of the Brillouin zone, as is shown in [32]. For the pure $ThO_2$ bulk, the band gap is 5.04 eV in the PBE+U functional, consistent with other theories published to date [41, 42, 45, 46, and 47]. A similar band gap was obtained with PBE+U in the density mixing scheme and the EDFT scheme. These are the band structures within the same PBE functional plus a correlation energy U from different convergence schemes and should converge to the same ground states. While the band structure is very similar, one makes $ThO_2$ more p-type, the other more n-type. A key point that comes from comparing the band structure from different functionals is that the resulting calculated band structures do differ.

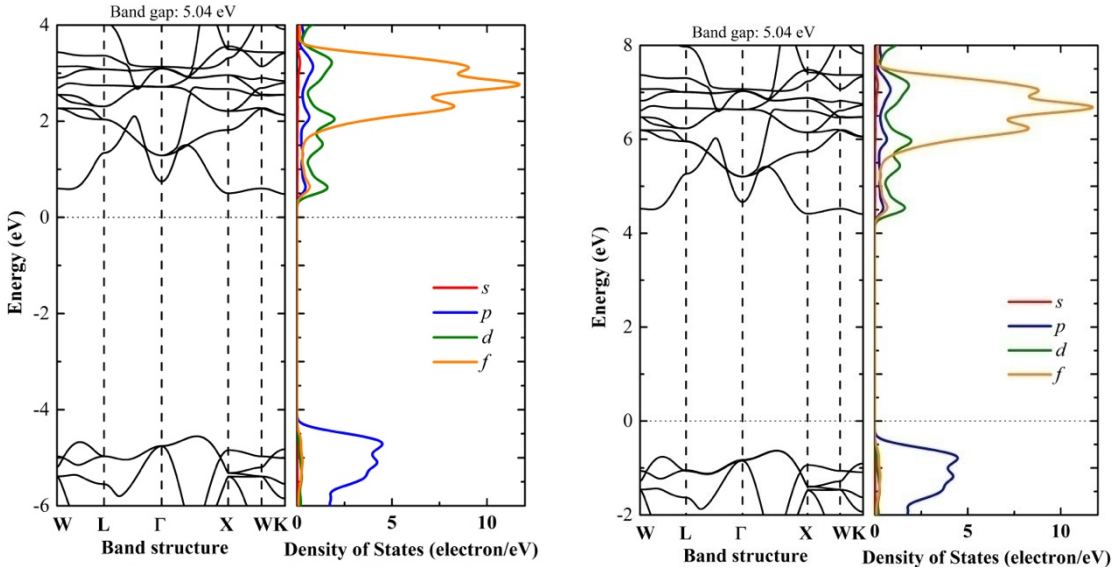


**Figure 35. Band structure and density of states of $ThO_2$ by the (a) PBE+U functional in the density mixing scheme and by (b) PBE+U function in the EDFT scheme.**

The calculated bulk dielectric function is shown in Figure 36. Absorption and the optical response will occur for any symmetry and selection rule allowed transition at any place in the Brillouin zone, not just Γ, so long as the transition itself has little or no momentum exchange, i.e. is a Δq=0 transition. Basically, the low lying critical points found in experiment (Figure 32) are qualitatively reproduced in theory, though shifted to higher energies in the HSE theory, as summarized in Table 7. For PBE, the agreement is more in line with experiment, but also qualitatively similar to HSE. This means that the strongest contributions to the optical properties for $ThO_2$ are the p-d transitions in the region of 5-8 eV. This places the low lying critical points for $ThO_2$ at 5.5 eV (the Δq=0 [p-d; e symmetry] transition in the region of W-L, and the Δq=0 [p-d; $a_1$ symmetry] transition in the region of gamma) and at 6.8 eV (the combined q=0 transitions [p-d; e symmetry] in the region of W and K.

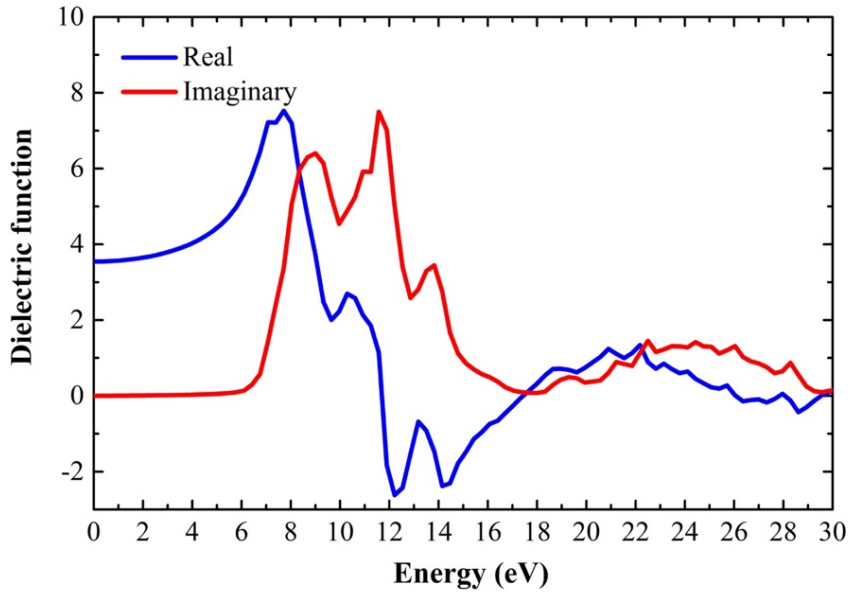


**Figure 36. The calculated real (blue) and imaginary (red) parts of the $ThO_2$ dielectric function.**

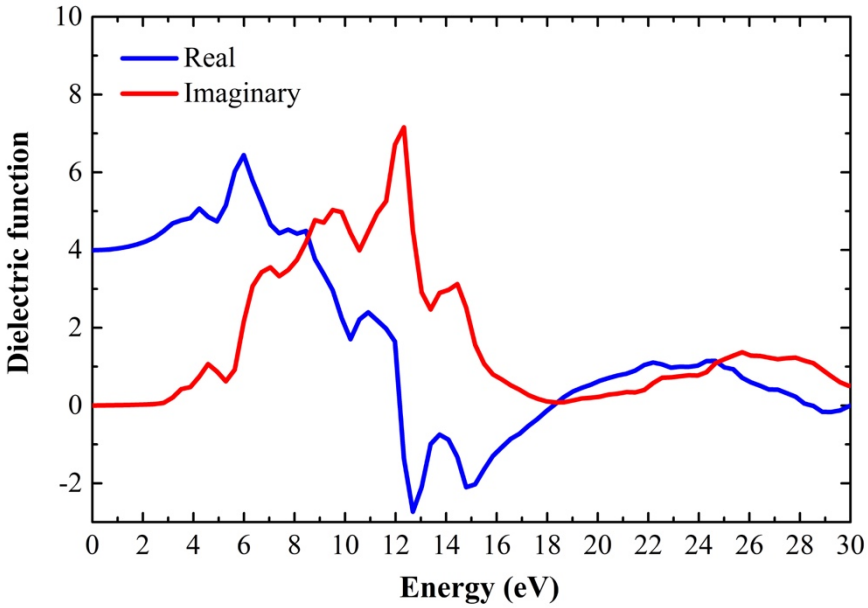


**Figure 37. The calculated real (blue) and imaginary (red) parts of the $UO_2$ dielectric function.**

Five critical points are observed in the investigated spectra for both of the actinides oxides, $UO_2$ (Table 8) and $ThO_2$ (Table 7). The two actinides have a very similar oscillator

pattern that appears to be compressed and shifted to higher energy for the $ThO_2$ for the features below 10 eV. For example, a fairly small amplitude oscillator is used to describe the lowest energy critical point and a relatively large amplitude oscillator is needed to render the optical response of the energetic third critical point in both cases. Also, the critical points observed in $UO_2$ are broader than their counterparts in $ThO_2$. These trends are also seen in the calculated real and imaginary parts of the dielectric function for $ThO_2$ (Figure 34) and $UO_2$ (Figure 32). For the features at roughly 10, 12, 14 and 15 eV, thoria ($ThO_2$) and urania ($UO_2$) resemble each other as noted in [42]. The calculated optical properties of Figure 34 and Figure 32 differ, but it should be noted that there is now a wealth of information on $UO_2$, as summarized in Table 8, and the transition energies in variable angle ellipsometry measured here, agree with the cathodoluminescence and theory. This means that the transitions can be assigned, based on the theory.

The fact that the cathodoluminescence features are generally very weak, especially for the luminescence corresponding to the lowest unoccupied state to highest occupied state transition, for single crystal $UO_2$, is because this transition is a selection rule forbidden transition. A $U5f \rightarrow U5f$ transition does not obey the required $\Delta l = \pm 1$ for an optical transition. $U6d/5f \rightarrow O\ 2p$ luminescence transitions are also expected to be weak as they are extra-atomic transitions, as is observed here. The strongest luminescence feature is the on-site, selection rule allowed $U\ 6d \rightarrow U\ 5f$ transition, as seen in Figure 33. These transition assignments are consistent not only with theory [10], but also combined XPS and inverse XPS studies of $UO_2$ [43]. This, in turn, implies that $UO_2$ and $ThO_2$ are indeed strongly correlated systems with correlation energies in the region of 6 eV for $ThO_2$ [44] and 4-5 eV for $UO_2$ [32, 33].

## 8.5 Conclusions

There is a consistent picture of the electronic structure, from experiment, that is not shared among the many theoretical band structure calculations. As noted elsewhere [45], when it comes to theory, the final arbiter of successful theoretical band structure calculations appears to be agreement with the experimental results for the actinide oxides. As sample quality improves, the variation between experiments is increasingly diminished, although the role of screening appears to have a profound effect on experiment. Surface effects, not discussed here, are expected to be a persistent problem and caution is needed in interpreting experimental results with a strong surface contribution.

## 8.6 References


[1] Boettger, J. and Ray, A. "All-Electron LCGTO Calculations for Uranium Dioxide," *International Journal of Quantum Chemistry*, vol. 80, p.824, 2000.

[2]Boettger, J. and Ray. A. "Fully Relativistic Density Functional Calculations on Hydroxylated Actinide Oxide Surfaces," *International Journal of Quantum Chemistry*, vol. 90, p.1470, 2002.

[3]Jomard, G. Amadon, B. Bottin, F. and Torrent, M. "Structural, Thermodynamic, and Electronic Properties of Plutonium Oxides from First Principles," *Physics Review B*, vol. 78, p. 07512, 2005.

[4]Zhang, P., Wang, B., Zhao, X. "Ground-State Properties and High-Pressure Behavior of Plutonium Dioxide: Density Functional Theory Calculations," *Physics Review B* vol. 82, p. 144110, 2010.

[5]Wang, B., Shi, H., Li, W., Zhang, P. "First-Principles LDA+U and GCA+U Study of Neptunium Dioxide," *Physics Review B* vol. 81, p. 45119, 2010.

[6]Lu, Y., Yang, W., Zheng, F., Wang, B. and Zhang, P. "Electronic, Mechanical, and Thermodynamic Properties of Americium Dioxide," *Journal of Nuclear Materials*, vol. 441, pp. 411-420, 2013.

[7] Gajdoš, M., Hummer, K., Kresse, G., Furthmüller, J. and Bechstedt, F. "Linear Optical Properties in the Projector-Augmented Wave Methodology," *Physics Review B*, vol. 73, p. 045112, 2006.

[8] Meek and von Roedern, B. “Semiconductor Devices Fabricated from Actinide Oxides,” *Vacuum*, vol. 83, pp. 226-228, 2008.

[9] Kruschwitz, C., Mukhopadhyay, S., Schwellenbach, D., Meek, T. and Shaver, B., "Semiconductor Neutron Detectors Using Depleted Uranium Oxide," *Proceedings SPIE 9213; Hard X-Ray, Gamma-Ray, and Neutron Detector Physics XVI*, San Diego, 2014.

[10]Schoenes, J. “Optical Properties and Electronic Structure of $UO_2$,”*Journal of Applied Physics*, vol. 49 p. 1463, 1978.

[11] Siekhaus, W. and Crowhurst, J. “Optical Properties of a Mechanically Polished and Air-Equilibrated [111] $UO_2$ Surface by Raman and Ellipsometric Spectroscopy,” *IOP Conference Series: Materials Science and Engineering*, vol. 9, p. 012055, 2010.

[12] Dugan, C., Peterson, G., Mock, A., Young, C., Mann, J.M., Nastasi, M., Schubert, M., Wang, L., Mei, W., Tanabe, I., Dowben, P. and Petrosky, J. “Electrical and Material Properties of Hydrothermally Grown Single Crystal (111) $UO_2$,”*European Physical Journal B*, vol. 91, p. 67, 2018.

[13] Meek, T. von Roedern, B., Clem, P. and Hanrahan Jr, R. “Some Optical Properties of Intrinsic and Doped $UO_2$ Thin Films,” *Materials Letters*, vol. 59, pp. 1085– 1088, 2005.

[14] Ehrenreich, H., and Cohen, M. "Self-Consistent Field Approach to the Many-Electron Problem," *Physics Review*, vol. 115, pp. 786-790, 1959.

[15] Kelly, T., Petrosky, J., McClory, J., Zens, T., Turner, D., Mann, J.M., Kolis, J., Colón Santana, J. and Dowben, P. “The Debye Temperature for Hydrothermally Grown $ThO_2$ Single Crystals,” *MRS Symposium Proceedings*, vol. 1576, 2013.

[16] Turner, D., Kelly, T., Peterson, G., Reding, J., Hengehold, R., Mann, J., Kolis, J., Zhang, X., Dowben, P., and Petrosky, P., “Electronic Structure of Hydrothermally Synthesized Single Crystal $U_{0.22}Th_{0.78}O_2$,” *Physica Status Solidi B*, vol. 253, pp. 1970–1976, 2016.

[17]Young, C., Petrosky, J., Mann, J., Hunt, E., Turner, D., and Kelly, T., “The work function of hydrothermally synthesized UO2 and the implications for semiconductor device fabrication,” *Physica Status Solidi Rapid Review Letters*, vol. 10, pp. 687–690, 2016.

[18] Young, C. Petrosky, J., Mann, J.M., Hunt, E., Turner, D. and Dowben, P. “The Lattice Stiffening Transition in $UO_2$ Single Crystals,” *Journal of Physics: Condensed Matter*, vol. 29, p. 035005; 2017.

[19] Kelly, T., Petrosky, J., Turner, D., McClory, J., Mann, J. M., Kolis, J., Zhang, X. and Dowben, P. “The Unoccupied Electronic Structure Characterization of Hydrothermally Grown $ThO_2$ Single Crystals,” *Physica Status Solidi RRL*, vol. 8, pp. 283-286, 2014.

[20] Mann, J.M., Thompson, K. Serivalsatit, T. M. Tritt, J. Ballato and Kolis, J. “Hydrothermal Growth and Thermal Property Characterization of $ThO_2$ Single Crystals,” *Crystal Growth and Design*, vol. 10, pp. 2146-2151, 2010.

[21] Lynds, L, Young, W., Mohl, J., and Libowitz, G. "X-ray and Density Study of Nonstoichiometry in Uranium Oxides," *Nonstoichiometric Compounds, American Chemical Society*, pp. 58-65, 1963.

[22] Leinders, G., Cardinels, T., Binnemans K., and Verwerft, M. “Accurate Lattice Parameter Measurements of Stoichiometric Uranium Dioxide,” *Journal of Nuclear Materials*, vol. 459, pp. 135-142, 2015.

[23] Aspnes, D., Theeten, J. and Hottier, F. “Investigation of Effective-Medium Models of Microscopic Surface Roughness by Spectroscopic Ellipsometry,” *Physical Review B.* vol. 20, p. 3292, 1979.

[24] Mock, A., Korlacki, R., Briley, C., Sekora, D., Hofmann, T., Wilson, P., Sinitskii, A., Schubert, E. and Schubert, M. “Anisotropy, Band-to-Band Transitions, Phonon Modes, and Oxidation Properties of Cobalt-Oxide Core-Shell Slanted Columnar Thin Films,” *Applied Physics*, vol. 108, p. 051905, 2016.

[25] Kresse, G. and Furthmüller, J. "Efficient Iterative Schemes for Ab Initio Total-Energy Calculations Using a Plane-Wave Basis Set," *Physical Review B*, vol. 54, p. 11169, 1994.

[26] Kresse, G. and Furthmüller, J. "Efficiency of Ab-Initio Total Energy Calculations for Metals and Semiconductors Using a Plane-Wave Basis Set," *Computational Materials Science*, vol. *6* , pp. 15-50, 1996.

[27] Kresse, G. and Hafner, J. "Ab Initio Molecular Dynamics for Liquid Metals," *Physical Review B*, vol.47, p. 558. 1993.

[28] Kresse, G. and Joubert, D. "From Ultrasoft Pseudopotentials to the Projector Augmented-Wave Method," *Physical Review B*, vol. 59, p. 1758, 1999.

[29] Perdew, J.; Burke, K.; Ernzerhof, M. "Generalized Gradient Approximation Made Simple," *Physics Review Letters*, vol. 77, p. 3865, 1996.

[30] Heyd, J., Scuseria, G., Ernzerhof and Erratum, M.: “Hybrid Functionals Based on a Screened Coulomb Potential,” *Journal of Chemical Physics*, vol. 118, pp. 8207-8215, 2003.

[31] Gajdos, M.; Hummer, K.; Kresse, G.; Furthmuller, J.; Bechstedt, F. "Linear Optical Properties in the Projector-Augmented Wave Methodology," *Physical Review B*, vol. 73, p. 045112, 2006.

[32] R. Lasowski, Madsen, G., Blaha, P. and Schwarz, K. "Magnetic Structure and Electric-Field Gradients of Uranium Dioxide: An ab Initio Study, " *Physical Review B*, vol. 69, p. 140408 (R), 2004.

[33] Sui, P., Dai, Z., Zhang, X. and Zhao, Y. "Electronic Structure and Optical Properties in Uranium Dioxide: the First Principle Calculations," *Chinese Physics* Letters, vol. 32, p. 077101, 2015.

[34] Dudarev, S., Botton, G. Savrasov, S., Szotek, Z., Temmerman, W. and Sutton, A." Electronic Structure and Elastic Properties of Strongly Correlated Metal Oxides from First Principles: LSDA + U, SIC-LSDA and EELS Study of $UO_2$ and NiO," *Physica Status Solidi* A, vol. 166, p. 429, 1998.

[35] Chen, Q., Lai, X., Tang, T., Bai, B., Chu, M., Zhang, Y. and Tan, S. "First-Principles Study of the Electronic Structure and Optical Properties of $UO_2$," *Journal of Nuclear Materials*, vol. 401, pp.118–123, 2010.

[36] Nerikar, P., Watanabe, T., Tulenko, J., Phillpot, S., and Sinnott, S. "Energetic Intrinsic Point Defects in Uranium Dioxide from Electronic-Structure Calculations," *Journal of Nuclear Materials*, vol. 384, pp. 61–69, 2009.

[37] Prodan, I., Scuseria, G., and Martin, R. " Covalency in the Actinide Dioxides: Systematic Study of the Electronic Properties Using Screened Hybrid Density Functional Theory," *Physical Review B: Condensed Matter Physics*, vol. 73, pp. 045104 -045110, 2007.

[38] Roy, L., Durakiewicz, T., Martin, R., Peralta, J., Scuseria, G., Olson, C, Joyce, J. and Guziewicz, E., "Dispersion in the Mott Insulator $UO_2$: A Comparison of Photoemission Spectroscopy and Screened Hybrid Density Functional Theory," *Journal of Computational Chemistry*, vol. 29, pp. 2288–2294, 2008.

[39] Maehira, T. and Hotta, T. "Relativistic Band-Structure Calculations for Electronic Properties of Actinide Dioxides," *Journal of Magnetism and Magnetic Materials*, vol.310, pp. 754–756, 2007.

[40] Wen, X., Martin, R., Roy, L., Scuseria, G., Rudin, S., Batista, E., McCleskey, T., Scott, B., Bauer, E., Joyce, J. and Durakiewicz, T." Effect of Spin-Orbit Coupling on the Actinide Dioxides $AnO_2$ (An=Th, Pa, U, Np, Pu, and Am): A Screened Hybrid Density Functional Study," *Journal of Chemical Physics*, vol. 137, p. 154707, 2012.

[41] Chongjie Mo, Yu Yang, Wei Kang, and Ping Zhang, "Electronic and Optical Properties of (U, Th)$O_2$ Compound from Screened Hybrid Density Functional Studies," *Physics Letters A*, vol. 380, pp. 1481–1486, 2016.

[42] Jayakumara, O., Gopalakrishnana, I., Vinub, A., Asthanac, A., and Tyagia, A. " Room Temperature Ferromagnetism in $Th_{1-x}Fe_xO_{2-d}$ (X=0.0, 0.05, 0.10, 0.15, 0.20 and 0.25) Nanoparticles, " *Journal of Alloys and Compounds*, vol. 461, p.p. 608-611, 2008.

[43] Szpunar, B. and Szpunar, J. "Application of Density Functional Theory in Assessing Properties of Thoria and Recycled Fuels," *Journal of Nuclear Materials*, vol. 439, pp. 243–250, 2013.

[44] Baer, Y. and Schoenes, J. "Electronic Structure and Coulomb Correlation Energy in $UO_2$ Single Crystal," *Solid State Communications*, vol. 33, p. 885, 1980.

[45] Kelly, P. and Brooks, M. "Electronic Structure and Ground-State Properties of the Actinide Dioxides," *Journal of the Chemical Society, Faraday*, vol. 2-83, p.1189, 1987.

# IX. Conclusions

## 9.1 Summary of Findings

This study applied a broad set of techniques to examine the characteristics of a recent material growth development for $ThO_2$ and $UO_2$, hydrothermal synthesis. The techniques applied in this research have led to a better understanding of the surface characteristics of $ThO_2$ and $UO_2$ grown by this method, and provide some insight into the characteristics of this material compared to those previously reported in literature. Particularly in the case of $UO_2$, the evidence shows that although the growth technique is unique, it does not yet avoid some of the problems associated with $UO_2$ in the specific applications for a majority of this research; a novel $UO_2$ based detector. Specifically, the $UO_2$ surface and selvedge region suffer from progressive oxidation and result in an unstable character where material parameters, such as band gap, and mobility can be uncertain and possibly changing, primarily based upon the XPS studies. There is, however, evidence that this growth method produces high quality samples, as shown by the extinction coefficient of ellipsometry and the relatively high carrier mobility. Additionally, there is evidence that appropriate contacts provide access to the stable regions of the structure and possibly the bulk, which may allow for bulk characterization to begin despite surface changes. Lastly, this growth process has produced large bulk crystals, which provide large nearly-homogenous regions upon which to conduct experiments. It is this last fact that allowed for the progress of this work and assessment of the optical and semiconductor properties, that was not previously possible.

With the development of s.c. $UO_2$, the suitability of $UO_2$ as a neutron detection material was examined via semiconductor and material physics. Initial measurement of the mobility for hydrothermally grown s.c. $UO_2$ provided insight into the sample quality, as it was in the higher

range of reported values with little surface treatment. The consistency of the bulk d.c. I(V) measurements reported here provides evidence that measured Hall currents are reaching below the surface layer, which is known to oxidize and restructure. The measured mobility and conductivity are highly favorable for $UO_2$ being selected as the working semiconductor for a solid-state neutron detection device. As with many novel materials, we also have demonstrated some of the behaviors that must be considered when working with $UO_2$ that are not observed with more traditional materials.

Another study of a layered s.c. $UO_2$, $CaF_2$, $UO_2$ crystal with Ag paint and E-GaIn contacts provided insight into the semiconductor and optical properties of $UO_2$. Ellipsometry measurements indicates $UO_2$ is relatively isotropic with a band gap of approximately 2.0 eV, consistent with theoretical expectations. The very long drift carrier lifetimes, obtained from current-voltage I(V) and capacitance-voltage C(*V*) measurements, along with the well-defined optical properties provide little evidence of an abundance of material defects away from the surface region. Schottky barrier formation may be possible, but very much dependent on the choice of contact and surface stoichiometry and we find that ohmic contacts are in fact favored.

Surface passivation for device fabrication and reactor applications were explored more carefully by incorporating a small atomic percentage of $ThO_2$, with an approximately 6% lattice mismatch, into the $UO_2$ crystal during growth. The Debye temperature for hydrothermally grown s.c. alloys of $U_{0.71}Th_{0.29}O_2$ was investigated using XPS and compared with similarly grown $ThO_2$ and $UO_2$. The alloy has a reduced Debye temperature while maintaining 4 *f* peak conformity. This result indicates that heat capacity is favorably raised for the ternary alloy, presenting a potentially added benefit in the use of the alloy as a mixed reactor fuel for either breeding or conversion fuel. The XPS result, although not conclusive, indicates that Th/U

substitution in the fluorite structure does not present additional defect damage, but instead provides for multiple vibrational modes to be accessed during heating. If so, this may be a positive new growth method that can lead to uranium/thorium mixed fuels that maintain structural integrity under typical reactor conditions.

Next, temperature dependent specific heat capacities for uranium dioxide, $UO_2$, thorium dioxide, $ThO_2$, and, $U_{0.71}Th_{0.29}O_2$ have been calculated using an XPS determined Debye temperature and compared to heat capacities obtained by MDSC. Uranium dioxide's surface structure, reduction or oxidation potential, and chemical reactivity play a significant role in solid-state device fabrication. Material doping and hence device conductivity is dependent oxygen atom mobility through the $UO_2$ fluorite lattice. An n-type $UO_{2-x}$ and $UO_2$ surface is created as oxygen migrates through lattice vacancies. On a $UO_{2+x}$ surface, interstitial oxygen migration dominates creating a p-type semiconductor. The measurements cover the temperature ranges from 193 to 673 K. MDSC demonstrates single-crystal actinides initially experience a higher heat capacity than an amorphous $UO_2$ fuel pellet. Finally, the XPS derived Debye temperature heat capacities are lower than the MDSC calculated measurements and possibly more accurate due to a cleaner, less oxidized crystal surface.

Variation in previously published results may be attributed to dissimilarities in material structure, bulk versus surface measurements, disparity in crystal quality, and the measurement environment. It appears the most accurate way to quantify the specific heat capacity of s.c. $UO_2$ and $ThO_2$ crystals is in ultra-high vacuum where there is an ability to remove surface oxidation. Common specific heat capacity measurement techniques such as MDSC alter the specific heat capacity of easily oxidized crystals, such as actinide oxides, during measurement.

Finally, an examination of the $UO_2$ surface defected with $H_2O$ and $O_2$ was conducted using angle resolved photoemission to determine if the material characteristics of stoichiometric $UO_2$ were maintained and if the surface contact was suitable for device fabrication. Angle-resolved photoemission confirms the presence of $H_2O$ and $O_2$ on the surface and in the selvedge region with increased U4*f* binding energies and the observed chemical shift of the O 1*s* peak. Peak deconvolution of the U $4f_{7/2}$ peak provides evidence of $U^{4+}$ and $U^{6+}$ oxidation states confirming we have not probed the bulk through the $UO_2$ surface and selvedge region. The presence of U 5*f* peaks in the valence band spectra provides evidence of the $U^{4+}$ oxidation state but does not refute the presence of the $U^{6+}$. The electronic band-gap energy of 2.2 eV confirms the presence of $UO_2$. Possible explanations are a new oxide growth on the surface of the $UO_2$ crystal or excess oxygen incorporated into the interstitial sites in the lattice to form a $UO_{2+x}$ surface.

## 9.2. Future Work

### *9.2.1 Materials Characterization*

In order to understand intrinsic defects in $UO_2$, cathodoluminescence and photoluminescence spectroscopy can be conducted on s.c. $UO_2$ samples. The material growth studies have matured sufficiently and the analyses conducted in the present research indicate sufficient maturity to begin these measurements. Further research must include a comparison of the native defect structures to those induced by radiation, as this could present a substantial limitation to hydrothermal growth or even for $UO_2$ semiconductor applications for neutron detection because of long-term performance degradation.

A second and near immediate need is related to developing and analyzing passivation materials to incorporate in device design. In the present research we investigated the potential for use of uranium-thorium alloys as a potential stable material for inclusion in a neutron detection device. The initial results of this study are promising in that the Th incorporation in low atomic density does not alter the $UO_2$ character sufficiently to change the band structure. This is promising, but understanding the overall effect on electronic characteristics is certainly the next step. The present study may provide a template for the next study.

To progress the hydrothermal growth technology to device realization, diode formation methods must be realized. Literature provides some indication through DFT and band mapping that the U 5*f* electron shell present as the intraband results in a p-type majority carrier. This is known to improve carrier concentration with low oxidation ($UO_{2.13}$) until a phase change occurs.

### *9.2.2 Electrical Characterization*

In addition to further material characterization after thermal and fast neutron irradiation, further electric measurements can be pursued to build a solid-state neutron detector. A requirement is an in-depth contact study providing consistent Hall effect and I(V) measurements with evaporated contacts. Once a contact material is identified with optimal thickness and area, the $UO_2$ device can be packaged to produce an output signal identifying neutrons. Finally, the detector's response after neutron irradiation must be examined to determine the overall effect on detection efficiency.

# REPORT DOCUMENTATION PAGE

*Form Approved*
*OMB No. 0704-0188*



| **1. REPORT DATE** *(DD-MM-YYYY)* | **2. REPORT TYPE** | **3. DATES COVERED** *(From - To)* |
|---|---|---|
| 20-12-2018 | Ph.D. Dissertation | October 2015-December 2018 |

**4. TITLE AND SUBTITL**
Electrical Characterization of Crystalline $UO_2$, $ThO_2$, and $U_{0.71}Th_{0.29}O_2$

**5a. CONTRACT NUMBER**

**5b. GRANT NUMBER**

**5c. PROGRAM ELEMENT NUMBER**

**6. AUTHOR(S)**
Dugan, Christina L., Lieutenant Colonel, USA

**5d. PROJECT NUMBER**

**5e. TASK NUMBER**

**5f. WORK UNIT NUMBER**

**7. PERFORMING ORGANIZATION NAME(S) AND ADDRESS(ES)**
Air Force Institute of Technology

Graduate School of Engineering and Management (AFIT/EN)
2950 Hobson Way, Wright-Patterson AFB OH 45433-7765

**8. PERFORMING ORGANIZATION REPORT NUMBER**
AFIT-ENP-DS-18-D-007

**9. SPONSORING / MONITORING AGENCY NAME(S) AND ADDRESS(ES)**
ATTN: Amalie Zeitoun
Domestic Nuclear Detection Office
Mail Stop 0550 Department of Homeland Security
245 Murray Lane
Washington DC 20528

**10. SPONSOR/MONITOR'S ACRONYM(S)**
DHS/DNDO

**11. SPONSOR/MONITOR'S REPORT NUMBER(S)**

**12. DISTRIBUTION / AVAILABILITY STATEMENT**
Distribution Statement A. Approved for Public Release; Distribution Unlimited

**13. SUPPLEMENTARY NOTES**
This work is declared a work of the U.S. Government and is not subject to copyright protection in the United States.

## 14. ABSTRACT

Uranium dioxide ($UO_2$), thorium dioxide ($ThO_2$), and $U_xTh_{1-x}O_2$ alloys are characterized for suitability in uranium-based neutron detectors. $ThO_2$ was studied for an envisioned $UO_2/ThO_2$ heterojunction. A $U_{0.71}Th_{0.29}O_2$ alloy was studied because of its resistance to oxidation and potential use in surface passivation.

The $U_{0.71}Th_{0.29}O_2$ effective Debye temperature of 217± 24 K was measured using temperature-dependent x-ray photoemission spectroscopy (XPS). The specific heat capacity for the $U_{0.71}Th_{0.29}O_2$ alloy was calculated from the Debye temperature and compared to the heat capacity obtained from modulated-temperature differential scanning calorimetry (MDSC). The XPS derived Debye temperature specific heat capacity was lower than with MDSC due to effects of a vacuum reduced crystal surface.

Angle resolved XPS provides depth profiling of a $UO_2$ surface. The U $4f_{7/2}$ peaks are evident of $U^{4+}$ and $U^{6+}$ oxidation states with an increase in the $U^{4+}$ oxidation state further from the surface. The presence of U 5*f* peaks in the valence band spectra provided evidence of $U^{4+}$ but does not preclude the presence of $U^{6+}$, while the electronic band-gap energy remained at 2.2 eV, confirming the presence of $UO_2$. These surface characteristics indicated a vacuum reduced $UO_2$ surface and excess oxygen incorporated into the lattice forming a $UO_{2+x}$ selvedge region.

**15. SUBJECT TERMS**
Uranium Dioxide, Thorium Dioxide, Photoemission Spectroscopy, neutron detection

| **16. SECURITY CLASSIFICATION OF:** | | | **17. LIMITATION OF ABSTRACT** | **18. NUMBER OF PAGES** | **19a. NAME OF RESPONSIBLE PERSON** |
|---|---|---|---|---|---|
| **a. REPORT** | **b. ABSTRACT** | **c. THIS PAGE** | | | James C. Petrosky, AFIT/ENP |
| U | U | U | UU | 155 | **19b. TELEPHONE NUMBER** *(include area code)* (937) 255-3636 x4562 |

**Standard Form 298 (Rev. 8-98)**
**Prescribed by ANSI Std. Z39.18**